

UNIVERSITY OF BRISTOL



University of
BRISTOL

MASTER'S THESIS

Quantum Dynamics of Bath Influenced
Excitonic Energy Transfer in Photosynthetic
Pigment-Protein Complexes

Author:

Joseph W. ABBOTT

Supervisor:

Professor Fred MANBY

2nd Assessor:

Professor Adrian MULHOLLAND

*A thesis submitted in partial fulfillment of the requirements
for the Honours degree of MSci Chemistry at the University of Bristol*

in the

Manby Group

School of Chemistry

April 16, 2020

UNIVERSITY OF BRISTOL

Abstract

Faculty of Arts and Sciences

School of Chemistry

MSci Chemistry

Quantum Dynamics of Bath Influenced Excitonic Energy Transfer in Photosynthetic Pigment-Protein Complexes

by Joseph W. ABBOTT

All life on Earth relies on the ability of photosynthetic organisms to efficiently harvest and trap energy from sunlight. Acting as a molecular wire, a protein-pigment complex (PPC) known as the *Fenna-Matthews-Olson* (FMO) complex found in green sulfur bacteria mediates the transfer of photo-excitation energy between the photosynthetic antennae complex, where energy is harvested, and the reaction centre, where it is trapped. The fine balance between intra-system and system-bath couplings present in the FMO complex allows it to perform unidirectional excitonic energy transfer (EET) with an almost 100% quantum yield. Using coherent theories, quantum dynamical treatment of the bath-influenced EET process can simulate, *in silico*, coherence effects that have been observed experimentally. The celebrated hierarchical equations of motion (HEOM) approach accurately describes EET dynamics and successfully accounts for non-equilibrium and non-Markovian effects. Though exact, with very few assumptions made about the dynamics or state of the system, HEOM is computationally very expensive for large systems. This motivates the use of a quantum master equation, such as the Lindblad equation formed under the Born-Markov approximation, as an alternative and cheaper description of EET. One such Lindblad model, in agreement with the HEOM approach and experiment, is particularly effective in describing the EET dynamics in the FMO complex despite the minimal computational cost.

Acknowledgements

I would like to thank Professor Fred Manby for inspiring discussions on topics both related and unrelated to quantum chemistry; Dr Susannah Bourne-Worster for her endless answers and support; and Dr Alex Buccheri, Harry Stroud, Oliver Feighan, and the rest of the Manby Group for their useful insights, advice, and encouragement.

I would also like to thank my parents for everything they have done for me, as well as my friends, family, and peers in Bristol, Seattle, and elsewhere for a memorable 4 years.

Contents

Abstract	iii
Acknowledgements	v
1 Introduction	1
1.1 Light Harvesting	1
1.2 The FMO Complex	3
1.2.1 Excitons	3
1.2.2 The FMO Hamiltonian	4
1.3 The Protein Environment	6
1.3.1 The System-Bath Model	7
1.3.2 Quantum States for Open Systems	8
1.3.3 Dynamical Processes	9
1.3.4 Time Evolution	11
1.3.5 Coherent Theories	11
1.4 Influence of the Bath	12
1.4.1 Harmonic Potentials	12
1.4.2 Correlation Functions	13
1.4.3 The Spectral Density	14
1.4.4 Population Transfer Rates	16
1.4.5 Thermal Equilibrium	16
1.5 The Lindblad Quantum Master Equation	17
1.5.1 General Form	18
1.5.2 Properties	18
1.5.3 Approximations	19
1.5.4 Construction of the Lindblad Operator	20
Local Dephasing	21

Global Thermalising	21
Local Thermalising	21
1.6 Hierarchical Equations of Motion	22
1.6.1 Influence Functional	23
1.6.2 Auxiliary Density Matrices	24
1.6.3 Hierarchy Truncation	25
2 Results and Discussion	27
2.1 Model 2-Site System	28
2.1.1 The Spin-Boson Hamiltonian	28
2.1.2 Key Features of the Lindblad Models	31
2.1.3 Trace Distance	34
2.1.4 Non-Markovianity	36
2.1.5 Non-Canonical Steady States	39
2.1.6 Summary	42
2.2 The FMO Complex	42
2.2.1 Parameters	42
2.2.2 Qualitative Model Comparison	43
2.2.3 Equilibration Timescales	45
2.2.4 Quantum Beating and EET Pathways	48
2.2.5 Entering Non-Markovian Regimes	50
2.2.6 Computational Expense	52
3 Conclusion	55
3.1 Summary	55
3.2 Future Work	56
3.2.1 Trapping Efficiency	56
3.2.2 The Spectral Density	57
3.3 Closing Remarks	61
3.3.1 Are Coherence Effects Important?	61
3.3.2 Light-Matter Interactions	62
A Mathematical Concepts	65
A.1 Abbreviations and Notation	65

A.2 Operators	65
A.2.1 Linearity	65
A.2.2 Commutation	66
A.2.3 Trace	66
A.2.4 Kronecker Product	67
A.2.5 Superoperators	67
A.3 Hermitian Operators	67
A.4 Delta Functions	68
A.4.1 Dirac	68
A.4.2 Kronecker	68
B Background Quantum Theory	69
B.1 Energy of the System	69
B.2 The Density Matrix	70
B.3 Liouville Space	70
B.4 The Liouville-von Neumann Equation	72
B.5 Harmonic Potentials	73
B.6 Hierarchical Equations of Motion	74
B.6.1 Bath Correlation Function	74
C Code	77
C.1 General Use	77
C.2 Reproducing Figures	77

List of Figures

1.1	The light harvesting architecture in the green sulfur bacteria <i>Chlorobium tepidum</i> . The FMO trimer sits between the reaction centre, which is embedded in the cell's cytoplasmic membrane, and the baseplate protein of the first chlorosome. Reproduced from Figure 1 of Wen <i>et al.</i> ¹	2
1.2	a) The structure of BChl-a, redrawn from Figure 2 of Fenna and Matthews; ² b) each BChl-a molecule in the FMO complex can be modelled as an effective two-level system.	3
1.3	Energy level schematic showing the relative energies of the chlorosomal base- plate protein, the BChl sites in the FMO complex, and the reaction centre. Excitation energy transferred from baseplate protein to BChl sites 1 and 6. Dominant couplings between sites given by double-headed purple arrows. En- ergy trapped at the reaction centre <i>via</i> sites 3 and 4. Reproduced from Figure 1 of Kreisbeck <i>et al.</i> ³ and Figure 5 of Ishizaki and Fleming. ⁴	5
1.4	a) The ground and first excited electronic states of a BChl site as harmonic potentials, showing the difference in minimum energies between the two poten- tials, ω_{eg} , and reorganisation energy, λ , recreated from Figure 1 of Ishizaki and Fleming; ⁴ b) the temporal correlation function of the dimensionless oscillator coordinates that decays with time.	13
2.1	a) The model 2-site system and harmonic bath used in Lindblad-HEOM bench- marking; b) an energy level schematic of the two sites where site 1 has been arbitrarily defined as having a higher energy than site 2. Site energies are equally distributed around zero, separated by ϵ , in accordance with the spin- boson system Hamiltonian. Tunneling between sites, of strength Δ , is indicated with the double-headed arrow.	28

2.2	Unitary evolution of the density matrix elements of a 2-site closed quantum system governed by the spin-boson system Hamiltonian, with $\epsilon = 20 \text{ rad ps}^{-1}$, $\Delta = 35 \text{ rad ps}^{-1}$, and initial excitation on site 1. Real site populations and imaginary parts of site coherences are plotted.	30
2.3	The 1.5 ps evolution of the purity of a 2-site open quantum system described by each of the Lindblad models and HEOM. Bath interactions induce mixedness in the state of the system over time. Parameters: $T = 300 \text{ K}$, $\epsilon = 40 \text{ rad ps}^{-1}$, $\Delta = 20 \text{ rad ps}^{-1}$, $\gamma = 20 \text{ rad ps}^{-1}$, $\lambda = 2 \text{ rad ps}^{-1}$, $\Gamma_{\text{deph}} = 11 \text{ rad ps}^{-1}$. . .	30
2.4	The 1.5 ps evolution of the inverse participation ratio (IPR) of quantum states for each Lindblad model and HEOM. Parameters used as in Figure 2.3. . . .	31
2.5	Left: the 2.5 ps evolution of the density matrix elements of the model 2-site system, described by the local dephasing Lindblad model. Right: the evolution of the site 1 population ρ_{11} and site coherence ρ_{21} compared to HEOM. . . .	32
2.6	Left: the 2.5 ps evolution of the density matrix elements of the model 2-site system, described by the global thermalising Lindblad model. Right: the evolution of the site 1 population ρ_{11} and site coherence ρ_{21} compared to HEOM. . . .	33
2.7	Left: the 2.5 ps evolution of the density matrix elements of the model 2-site system, described by the local thermalising Lindblad model. Right: the evolution of the site 1 population ρ_{11} and site coherence ρ_{21} compared to HEOM. . . .	35
2.8	The time-evolution of the trace distance between states $\rho^{(1)}(t)$ and $\rho^{(2)}(t)$, where each has a different initial excitation, $\langle 1 \rho^{(1)}(0) 1 \rangle = 1$ and $\langle 2 \rho^{(2)}(0) 2 \rangle = 1$, plotted for each Lindblad model and HEOM. Monotonically decreasing curves (Lindblad) suggests purely Markovian behaviour, whereas regions of positive derivative indicates non-Markovian behaviour.	36
2.9	Left: the 1 ps evolution of the site 1 population, described by the local thermalising Lindblad model and HEOM. Right: the Lindblad-HEOM trace distance over the course of the 1 ps evolution, for every Lindblad model (top) and just the local thermalising model (bottom). Top row: all models defined with a fixed parameter set. Bottom row: HEOM parameters kept the same as in the top row, but local thermalising Lindblad parameters changed to fit site 1 population to HEOM. $T = 300 \text{ K}$, $\gamma = 20 \text{ rad ps}^{-1}$, $\Gamma_{\text{deph}} = 11 \text{ rad ps}^{-1}$. . .	38

2.10 The temperature dependence of the trace distance with respect to the canonical thermal state for the local thermalising Lindblad (left) and HEOM (right). The Lindblad model equilibrates to the canonical state at all temperatures, whereas the HEOM model equilibrates to a non-canonical steady state that coincides with the canonical state only at higher temperatures.	41
2.11 A comparison of the HEOM (left-most column, reproduced from Figure 7 of Zhu <i>et al.</i> ⁵) and Lindblad dynamics of the FMO complex at T = 300 K. Each row corresponds to a different initial site excitation; a) site 1; b) site 6; c) a superposition of sites 1 and 6. $\gamma = 166 \text{ fs rad}^{-1}$, $\lambda = 35 \text{ cm}^{-1}$, $\Gamma_{\text{deph}} = 11.0 \text{ rad ps}^{-1}$	44
2.12 a) the 2.5 ps evolution of the inverse participation ratios states of the FMO complex described by each of the Lindblad models. Excitons remain relatively localised throughout; b) the site populations of the canonical thermal state of the FMO complex at cryogenic and physiological temperature. While sites 3 and 4 are still dominant at 300 K, it is clear that there is a tendency towards the maximally mixed state upon increasing temperature.	45
2.13 The 1 ps evolution of the FMO complex site populations for different initial states at cryogenic temperature (77 K). The outer columns show the unitary dynamics of the system alone, whereas the middle columns show the effect of the bath. The left two columns are plotted with HEOM, taken from Figure 3 of Zhu <i>et al.</i> , ⁵ while the right two columns are plotted with the local thermalising Lindblad. Rows correspond to different initial excitations; a) site 1; b) site 6; c) a superposition of 1 and 6. $\gamma = 50 \text{ fs rad}^{-1}$, $\lambda = 35 \text{ cm}^{-1}$, and $\Gamma_{\text{deph}} = 11.0 \text{ rad ps}^{-1}$	49
2.14 The 1 ps evolution of the FMO complex site populations at physiological temperature (300 K) for different bath relaxation timescales, γ^{-1} , with an initial excitation on a superposition of sites 1 and 6. Reproduced from Figure 6 of Zhu <i>et al.</i> ⁵	51

3.1 Top left: A comparison of the forms of the Debye (blue), Ohmic (orange), and Renger and Marcus' parameterised spectral densities (green). Top right: A comparison of the FMO complex site 1 population for each of the spectral densities, starting from initial excitation on site 1. Bottom: the 2.5 ps evolution of the FMO complex site populations with different spectral densities plotted in each column. Each row corresponds to a different initial excitation; a) site 1; b) site 6; c) a superposition of sites 1 and 6. Parameters used; T = 300 K, $\gamma^{-1} = 166 \text{ fs rad}^{-1}$, $\lambda = 35 \text{ cm}^{-1}$, and $\Gamma_{\text{deph}} = 11 \text{ rad ps}^{-1}$	59
C.1 Reproducing the fitted site 1 population from Figure 2.9 using the open-source Python package written by the author.	78

List of Tables

1.1	The exciton system Hamiltonian for the FMO monomer in the site basis, showing site energies and inter-site coupling strengths, in units of cm^{-1} . Dominant inter-site couplings are given in bold font.	4
1.2	The exciton energies, site-localisation probabilities, and inverse participation ratios (IPRs) for each exciton in the FMO monomer. The significant localisation probabilities (> 0.3) are given in bold, and the excitons ordered by increasing energy.	6
1.3	The Lindblad operators, rate constants, indices over which summation occurs, and conditions on the indices for the local dephasing, global thermalising, and local thermalising Lindblad models.	22
2.1	Equilibration times of each initial state for each Lindblad models at cryogenic and physiological temperatures. Equilibration times for different bath relaxation rates given at physiological temperature. HEOM data reported by Zhu <i>et al.</i> ⁵ included where applicable.	47

List of Abbreviations

BChl	Bacteriochlorophyll
EET	Excitonic Energy Transfer
FMO	Fenna-Matthews-Olson
PPC	Pigment-Protein Complex
ADM	Auxiliary Density Matrix
CPTP	Completely-Positive and Trace-Preserving
EOM	Equation Of Motion
HEOM	Hierarchical Equations Of Motion
IPR	Inverse Participation Ratio
MD	Molecular Dynamics
QME	Quantum Master Equation
RDM	Reduced Density Matrix
TDSE	Time Dependent Schrödinger Equation

Physical Constants

Speed of Light in a vacuum $c = 299\,792\,458 \text{ m s}^{-1}$

Euler's Number $e = 2.71828 \dots$

Reduced Planck's Constant $\hbar = 1.504\,571\,817 \times 10^{-34} \text{ J s}$

Boltzmann's Constant $k_B = 1.380\,650\,3 \times 10^{-23} \text{ J K}^{-1}$

List of Symbols

A_α	Lindblad operator	
c_k	Matsubara coefficient	
$C(t)$	temporal correlation function	
$D(t)$	trace distance	
H	Hamiltonian	
$J(\omega)$	spectral density	rad ps ⁻¹
$k(\omega)$	Redfield rate constant	rad ps ⁻¹
K	bath correlation terms	
$n_{\text{BE}}(\omega)$	Bose-Einstein distribution	
Q	integrated trace distance	
t	time	fs
T	temperature	K
γ	bath relaxation rate	rad ps ⁻¹
Γ_{deph}	dephasing rate	rad ps ⁻¹
Δ	tunneling strength	rad ps ⁻¹
ϵ_i	site energy	rad ps ⁻¹
λ	reorganisation energy	rad ps ⁻¹
ν_k	Matsubara frequency	rad ps ⁻¹
ω	angular frequency	rad ps ⁻¹
$ \psi(t)\rangle$	wavefunction	
$\rho(t)$	reduced density matrix	
$\sigma_{\mathbf{n}}(t)$	auxiliary density matrix	
\mathbb{I}	identity matrix	
\mathcal{L}	Liouvillian superoperator	
\mathcal{N}_c	hierarchy truncation level	

Chapter 1

Introduction

1.1 Light Harvesting

The design and synthesis of molecular machinery capable of efficiently converting energy from sunlight into useful chemical energy is one of the great challenges that underpins modern interdisciplinary clean energy research. In photosynthetic organisms, the process of light harvesting involves collection, transfer, and trapping of the energy from sunlight and occurs with almost 100% efficiency.⁶ Light harvesting comprises the first step of photosynthesis; a complex cascade of chemical reactions responsible for sustaining and providing energy to all life on Earth.^{7,8} How it works and why it is so efficient has been the focus of many experimental and theoretical studies over the past few decades.^{2,3,7,9–18} Developments in the field may lead to improvements in ‘light-to-charge’ conversions in artificial systems such as organic photo-voltaics (OPVs),¹⁹ while there have been suggestions that understanding the role quantum coherence plays may provide a link between fields of quantum biology and quantum computing.^{20–23}

The photon flux in which photosynthetic organisms operate is weak, meaning the probability of absorbing a photon is small.⁹ It is therefore of critical importance that the subsequent light harvesting process is very efficient. For the low-light adapted green sulfur bacteria *Prosthecochloris aestuarii* and *Chlorobium tepidum*, this is especially true. The energy from any sunlight they absorb is transferred between three chlorophyll ‘bodies’. The first, as the ones predominantly photo-excited by sunlight, are known as *chlorosomes* (or photosynthetic antennae) and contain roughly 95% of all the chlorophyll in such organisms.¹⁰ These reside below the cell’s cytoplasmic membrane, as seen in Figure 1.1.

The excitation energy is transferred *via* the second chlorophyll body, a bacteriochlorophyll-a (or *BChl*) pigment-protein complex (PPC), to the third, a pair of chlorophyll molecules known as the *special pair* that form part of the *reaction centre* PPC. This is where a charge separation occurs and the photo-excitation energy is converted into chemical energy in the form of a trans-membrane electrochemical gradient.^{11–13}

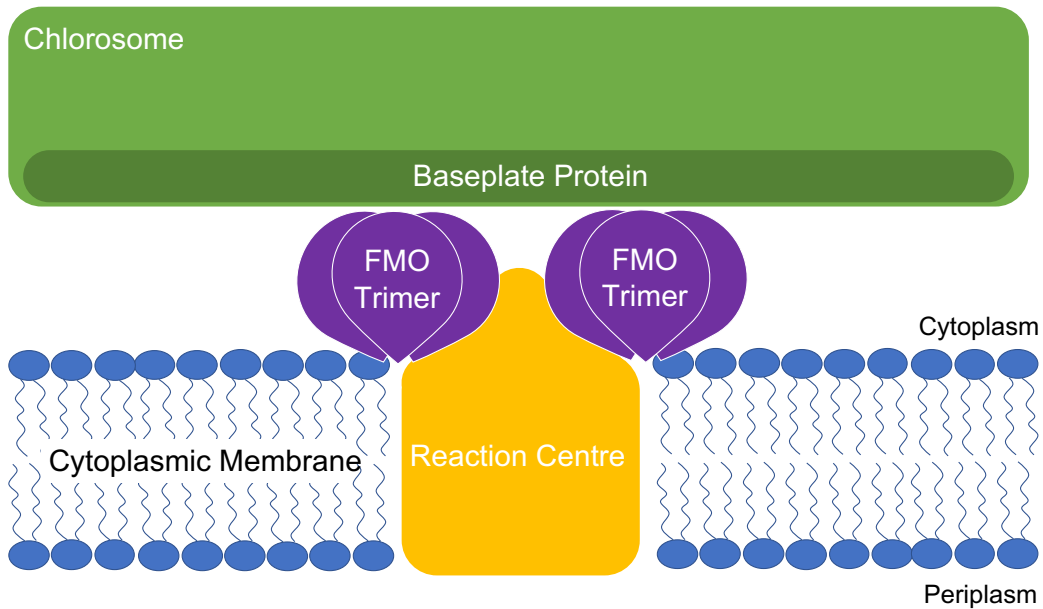


FIGURE 1.1: The light harvesting architecture in the green sulfur bacteria *Chlorobium tepidum*. The FMO trimer sits between the reaction centre, which is embedded in the cell's cytoplasmic membrane, and the baseplate protein of the first chlorosome. Reproduced from Figure 1 of Wen *et al.*.¹

In green sulfur bacteria, the *BChl-a* protein known as the *Fenna-Matthews-Olson* or FMO complex is a water soluble pigment-protein complex (PPC) that mediates the transfer of photo-excitation energy between the first chlorophyll body and the reaction centre, being described as a molecular ‘energy wire’.^{1,24} The FMO complex was first isolated and crystallised from *P. aestuarii* by Olson,²⁵ its structure determined to near-atomic resolution by Fenna and Matthews,^{2,26,27} and later refined by Tronrud *et al.*,¹⁰ before being crystallised from *C. tepidum* in 1997.²⁸ It has a trimeric structure with C_3 symmetry, consisting of three identical protein monomer units each of which binds seven *BChl-a* pigment molecules.⁸ X-ray crystal structures of the FMO monomer show that there exists an eighth *BChl-a* molecule residing in a cleft of the binding protein’s surface, but has been suggested that it doesn’t play an important role in transfer of excitation energy through the FMO monomer.²⁹

1.2 The FMO Complex

1.2.1 Excitons

Under physiologically relevant conditions, each BChl molecule within the FMO complex can be treated as an effective two-level system (Figure 1.2). This is because the population of the electronic energy levels is dominated by the ground and first excited states $|G\rangle$ and $|E\rangle$ respectively.¹⁶ The interaction of excitation energies within FMO, and therefore how the

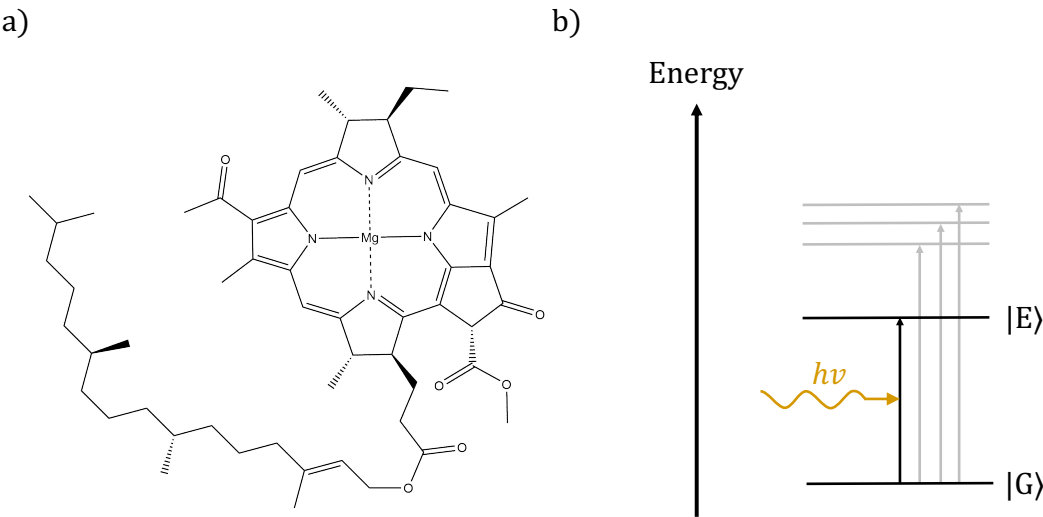


FIGURE 1.2: a) The structure of BChl-a, redrawn from Figure 2 of Fenna and Matthews;² b) each BChl-a molecule in the FMO complex can be modelled as an effective two-level system.

energy is transferred to the reaction centre, is described using the molecular Frenkel exciton model. Extended from its original applications in solid-state physics, this describes the first excited state of each BChl molecule as an exciton *quasi*-particle; an electron-electron hole pair attracted by a Coulombic interaction.⁷ It has been shown that within bacterial PPCs the excitons are localised to a few BChl molecules.³⁰ A quantification of the localisation of excitons within the FMO complex is introduced in the following subsection.

It is also assumed that excitations enter the system one at a time.³ Transfer of this photo-excitation energy occurs non-radiatively between excitons within the FMO complex, a process henceforth referred to as excitonic energy transfer (EET). This quantum-dynamical process, mediating the antennae to reaction centre energy transfer, is responsible in part for the high efficiency of the light harvesting process in photosynthetic bacteria such as *C. tepidum*. The rest of this introduction will be concerned with how a PPC such as the FMO complex and the EET dynamics within it can be described, using a quantum mechanical approach.

1.2.2 The FMO Hamiltonian

As part of the molecular Frenkel exciton model, the network of BChl molecules (or *sites*) can be described by a molecular exciton system Hamiltonian. This is a matrix (the mathematical form of *operators* in quantum mechanics, see Appendix A.2) that is Hermitian (see Appendix A.3), and takes the form:^{8,16,31}

$$H_{\text{sys}} = \sum_{i=1}^N |i\rangle \langle i| E_i + \sum_{i \neq j=1}^N V_{ij} |i\rangle \langle j| , \quad (1.1)$$

with diagonal elements E_i that correspond to the site (or excitation) energies and off-diagonal elements V_{ij} that correspond to inter-site interaction strengths. Physically, the latter represents the overlap of site electronic transition dipoles under the assumption that they are sufficiently spaced so that no exchange occurs.³¹ Site energies and couplings for the FMO complexes of both *P. aestuarii* and *C. tepidum* were experimentally calculated by Adolphs and Renger in 2006.⁸ While very similar in structure, there are subtle differences in the system Hamiltonians formed for each. The one for the FMO monomer in *C. tepidum* has been the focus of relevant theoretical studies into EET within the FMO complex,^{3–5} constructed using parameters for the site energies of the *trimer* from Table 4, and couplings from Table 1 in Adolphs and Renger. Its form in the site basis is given in Table 1.1, with numbering of BChl molecules consistent with the original paper by Fenna and Matthews,² and will be the system Hamiltonian that is used henceforth.

	BChl ₁	BChl ₂	BChl ₃	BChl ₄	BChl ₅	BChl ₆	BChl ₇
BChl ₁	12410	-87.7	5.5	-5.9	6.7	-13.7	-9.9
BChl ₂	-87.7	12530	30.8	8.2	0.7	11.8	4.3
BChl ₃	5.5	30.8	12210	-53.5	-2.2	-9.6	6.0
BChl ₄	-5.9	8.2	-53.5	12320	-70.7	-17.0	-63.3
BChl ₅	6.7	0.7	-2.2	-70.7	12480	81.1	-1.3
BChl ₆	-13.7	11.8	-9.6	-17.0	81.1	12630	39.7
BChl ₇	-9.9	4.3	6.0	-63.3	-1.3	39.7	12440

TABLE 1.1: The exciton system Hamiltonian for the FMO monomer in the site basis, showing site energies and inter-site coupling strengths, in units of cm^{-1} . Dominant inter-site couplings are given in bold font.

The site energies, relative to each other and to the reaction centre, as well as the dominant couplings between sites (given in Table 1.1 in **bold** font) are represented schematically on an energy level diagram in Figure 1.3. Every BChl molecule is assumed to have the same ground state energy. The baseplate protein of the chlorosome transfers the photo-excitation energy

predominantly to the spatially proximate sites 1 and 6.^{1,5} The dominant EET pathways are $1 \rightarrow 2 \rightarrow 3$ and $6 \rightarrow (5, 7) \rightarrow 4 \rightarrow 3$, with the former exhibiting stronger coherences than the latter.³² The EET pathways terminate irreversibly with trapping of the energy on the localised charge separation sites in the reaction centre, predominantly *via* the lowest energy site 3.

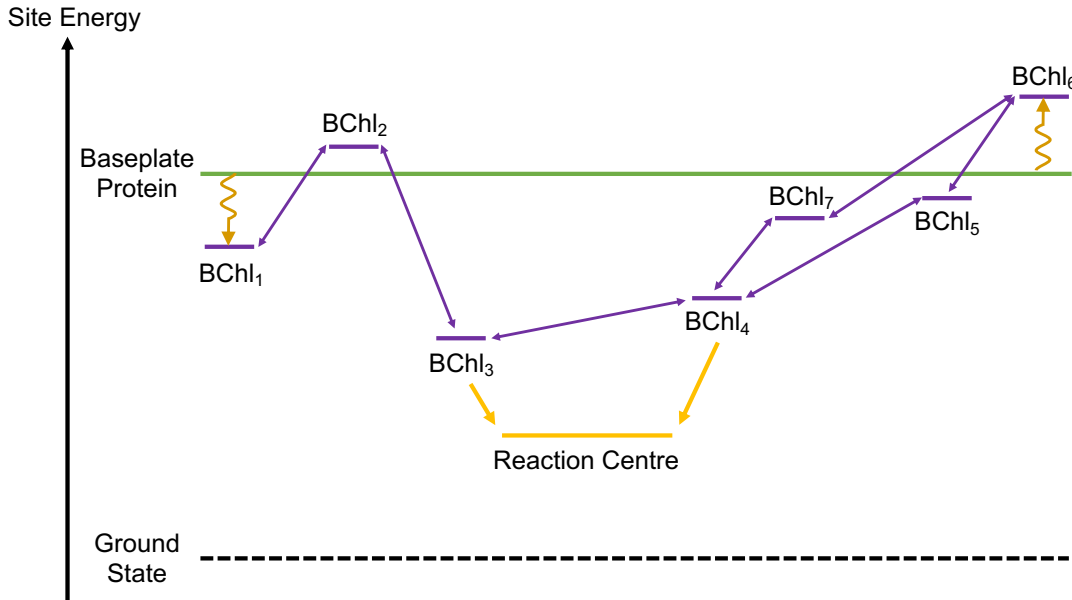


FIGURE 1.3: Energy level schematic showing the relative energies of the chlorosomal baseplate protein, the BChl sites in the FMO complex, and the reaction centre. Excitation energy transferred from baseplate protein to BChl sites 1 and 6. Dominant couplings between sites given by double-headed purple arrows. Energy trapped at the reaction centre *via* sites 3 and 4. Reproduced from Figure 1 of Kreisbeck *et al.*³ and Figure 5 of Ishizaki and Fleming.⁴

The FMO Hamiltonian in the site basis can be transformed into its eigenbasis by diagonalisation to find its eigenvalues and eigenstates. For a molecular Frenkel exciton Hamiltonian, the eigenvalues correspond to exciton energies, while the eigenstates describe the excitons themselves. These eigenstates (or *eigenvectors*) form an orthonormal set, so that $\langle a|b\rangle = \delta_{ab}$, where δ_{ab} is the Kronecker delta (see Appendix A.4). A general exciton, a , can be expressed as:

$$|a\rangle = \sum_i^N c_i(a) |i\rangle , \quad (1.2)$$

where N is the number of sites in the system ($N = 7$ for FMO), and the norm-squared of each c_i coefficient, $|c_i(a)|^2$, represents the probability that the a th exciton is localised on the i th site. For occupation of a single excitation in the PPC, the sum of the site-localisation

probabilities for any given exciton must equal one:

$$\sum_i^N |c_i|^2 = 1 . \quad (1.3)$$

Further to this, an *inverse participation ratio* (IPR) for each exciton can be calculated. This is defined as, for the a th exciton:

$$\text{IPR}(a) = \left(\sum_i^N (c_i(a))^4 \right)^{-1} \quad (1.4)$$

and represents the number of BChl molecules the exciton is delocalised across, where $c_i(a)$ is the i th site coefficient of the a th exciton.³³ The energies, localisation probabilities, and IPR values for each exciton in the FMO system are given in Table 1.2. With most of the excitons being approximately localised to a single BChl molecule ($1 \leq \text{IPR}(a) \leq 2$), only two excitons (B and C) have delocalisation lengths that extend over more than two sites.

Exciton	Energy (cm ⁻¹)	BChl ₁	BChl ₂	BChl ₃	BChl ₄	BChl ₅	BChl ₆	BChl ₇	IPR
A	12180	0.002	0.005	0.208	0.012	0.769	0.002	0.001	1.6
B	12292	0.189	0.022	0.004	0.559	0.002	0.029	0.195	2.6
C	12365	0.012	0.161	0.019	0.098	0.014	0.235	0.461	3.3
D	12455	0.000	0.764	0.006	0.008	0.004	0.000	0.217	1.6
E	12470	0.007	0.035	0.000	0.136	0.000	0.722	0.100	1.8
F	12578	0.779	0.000	0.004	0.183	0.017	0.002	0.015	1.6
G	12681	0.010	0.012	0.759	0.004	0.193	0.010	0.011	1.6

TABLE 1.2: The exciton energies, site-localisation probabilities, and inverse participation ratios (IPRs) for each exciton in the FMO monomer. The significant localisation probabilities (> 0.3) are given in bold, and the excitons ordered by increasing energy.

1.3 The Protein Environment

The protein environment that surrounds the system of BChl molecules in a PPC such as the FMO complex has a great influence on the EET dynamics within it, the efficiency of which is determined by a balance between the unitary dynamics of the system and the relaxation dynamics induced by the environment.³⁴ This section will introduce the quantum dynamical processes occurring in the FMO complex upon photo-excitation and how EET dynamics are monitored.

1.3.1 The System-Bath Model

The FMO complex consists of a network of BChl sites, henceforth referred to as the **system**, which is coupled to, and in thermal equilibrium with, the surrounding protein environment (the **bath**). The system must be considered an **open** quantum system, as the dynamical process of EET within it will be affected by interaction with the bath.

The Hamiltonian for the total, combined system (comprised of system and bath components) H_{tot} is given by the sum of individual Hamiltonians that characterise the system (i.e. the molecular exciton system Hamiltonian in Section 1.2.1), the bath, and the interaction between them. These are H_{sys} , H_{bath} , and H_{int} respectively, and form the basis of the system-bath model for open quantum systems:³⁵

$$H_{\text{tot}} = H_{\text{sys}} + H_{\text{bath}} + H_{\text{int}} . \quad (1.5)$$

Often in the problem of describing the dynamics open quantum systems, such as EET in light harvesting complexes, the thermal bath is modelled with an infinite number of degrees of freedom usually in the form of an infinite number of harmonic oscillators, based on work by Caldiera and Leggett in 1983.³⁶ The Hamiltonian for the collective bath modes H_{bath} is given by the sum of kinetic energy and potential energy terms (respectively) for each individual harmonic oscillator ξ :^{35,37}

$$H_{\text{bath}} = \sum_{\xi}^{\infty} \frac{p_{\xi}^2}{2m_{\xi}} + \frac{m_{\xi}\omega_{\xi}^2 q_{\xi}^2}{2} , \quad (1.6)$$

where p_{ξ} is the linear momentum of the oscillator, m_{ξ} its mass, ω_{ξ} its frequency of oscillation and q_{ξ} its dimensionless displacement from its minimum energy position. For a typical harmonic oscillator the force constant k_{ξ} of the oscillator is related to the mass and frequency by the relation $k_{\xi} = m_{\xi}\omega_{\xi}^2$. The excitonic system can couple to the vibrational modes of the harmonic bath, the interaction of which is characterised by H_{int} , the interaction Hamiltonian:^{8,37}

$$H_{\text{int}} = \sum_{\xi}^{\infty} \sum_{i}^N \hbar\omega_{\xi} q_{\xi} g_{\xi}^{(i)} |i\rangle \langle i| , \quad (1.7)$$

where the coupling constant $g_{\xi}^{(i)}$ defines the strength of interaction between the i th site in the system and ξ th bath mode.⁸ The system-bath coupling operator is $|i\rangle \langle i|$. The coupling between system and bath is assumed to be linear in oscillator displacement q_{ξ} .

1.3.2 Quantum States for Open Systems

A system in a **pure** quantum state can be completely described at any given time t by its state ket wavefunction, $|\psi(t)\rangle$. However, it is known that for an open quantum system such as the FMO complex that interaction of the system with the bath induces disorder in the system that affects its dynamics and results in **mixedness** in its quantum state.⁷ A mixed quantum state, defined as a statistical ensemble of pure states, cannot be fully described by a state ket wavefunction. Instead, a more general notation must be used in order to fully describe **any** quantum state; both pure and mixed. This is known as the *density matrix* denoted by $\rho(t)$ (see Appendix B.2), and for an N -site system takes the form:

$$\rho(t) = \begin{bmatrix} \rho_{11} & \rho_{12} & \dots & \rho_{1N} \\ \rho_{21} & \rho_{22} & \dots & \rho_{2N} \\ \vdots & \vdots & \ddots & \vdots \\ \rho_{N1} & \rho_{N2} & \dots & \rho_{NN} \end{bmatrix}, \quad (1.8)$$

where in the site basis the diagonal elements represent the site populations (the probability that a given site is in its excited state) and the off-diagonal elements represent coherences between sites.

Both the *system* and the *bath* are separate quantum systems in their own right, each constituting a component of the total combined system (the **universe**). The quantum states of the *system*, *bath*, and *universe* are given by density matrices $\rho(t)$, $\rho_B(t)$ and $\rho_{\text{tot}}(t)$ respectively. The system's density matrix, or the *reduced density matrix* (RDM), is the quantum state whose evolution in time is of interest, so is denoted by $\rho(t)$ for brevity.

At some initial time $t = 0$ it is often assumed that the *system* and *bath* components are initially uncorrelated or *decoupled*, so the state of the universe is therefore given by their product:^{31,38,39}

$$\rho_{\text{tot}}(0) = \rho(0) \otimes \rho_B(0), \quad (1.9)$$

where \otimes denotes the Kronecker product (see section A.2.4). While physically speaking it is not generally valid to assume that the system and bath are decoupled initially,⁴⁰ it is an assumption that is commonplace in the literature and allows for a convenient starting point from which the time evolution of the system after a single excitation event can be monitored.³⁹ The state of the system, given by the reduced density matrix $\rho(t)$, can be recovered by *tracing*

out the bath degrees of freedom from the density matrix of the universe:^{14,35}

$$\rho(t) = \text{tr}_B \{ \rho_{\text{tot}}(t) \} . \quad (1.10)$$

However, storing all the information of the system *and* the large and complex bath in the density matrix of the universe ρ_{tot} , evolving it in time, and then tracing out the bath degrees of freedom to retrieve the state of the system is a lengthy and computationally expensive procedure.³⁸ In addition to this, the form of the bath when modelled as an infinite set of oscillators cannot not be exactly known. It is more constructive to *capture* the influence of the bath on the system, as discussed in Section 1.4, rather than explicitly describing its degrees of freedom. Doing so means that only the state of the system at any time, $\rho(t)$, needs to be known.

1.3.3 Dynamical Processes

The processes that occur in the FMO complex as part of EET can be described by action of a superoperator (see Appendix B.3 and Appendix A.2.5) on the reduced system's density matrix. This yields a general equation of motion (EOM) known as the *Liouville equation* that can be used as a generalised starting point for describing EET dynamics in the FMO complex, taking the form:³⁵

$$\frac{d}{dt} \rho(t) = \mathcal{L} \rho(t) , \quad (1.11)$$

where \mathcal{L} is the general Liouvillian superoperator, which can be expressed as the sum of individual Liouvillian superoperators:

$$\mathcal{L} = \mathcal{L}_{\text{sys}} + \mathcal{L}_{\text{bath}} + \mathcal{L}_{\text{trap}} + \mathcal{L}_{\text{decay}} + \mathcal{L}_{\text{rad}} , \quad (1.12)$$

each of which captures a different dynamical process that occurs during EET.^{16,32} \mathcal{L}_{sys} represents the Hamiltonian commutation superoperator that accounts for unitary evolution governed by the system Hamiltonian H_{sys} :²³

$$\mathcal{L}_{\text{sys}} = -\frac{i}{\hbar} \left(H_{\text{sys}} \otimes \mathbb{I} - \mathbb{I} \otimes H_{\text{sys}}^\dagger \right) , \quad (1.13)$$

where \mathbb{I} is the identity matrix and \dagger denotes the complex conjugate transpose of the Hamiltonian. For a closed quantum system where the system-bath interaction isn't considered, the

only dynamical process that exists is the unitary evolution of the elements of the system's density matrix, i.e. $\mathcal{L} = \mathcal{L}_{\text{sys}}$. The equation of motion for such a process (that can be recovered by action of \mathcal{L}_{sys} on $\rho(t)$) yields the *Liouville-von Neumann equation*:³⁷

$$\frac{d}{dt}\rho(t) = \mathcal{L}_{\text{sys}}\rho(t) = -\frac{i}{\hbar}[H_{\text{sys}}, \rho(t)] , \quad (1.14)$$

which is the more general analogue of the time-dependent Schrödinger equation (TDSE):

$$\frac{d}{dt}|\psi(t)\rangle = -\frac{i}{\hbar}H_{\text{sys}}|\psi(t)\rangle , \quad (1.15)$$

from which it can be derived (see Appendix B.4).³⁵ $\mathcal{L}_{\text{trap}}$ captures the dynamics of the irreversible transfer of excitonic energy to the reaction centre, where it is trapped and localised on charge separation sites. $\mathcal{L}_{\text{decay}}$ accounts for the excitonic decay; the recombination of electron and electron hole resulting in the irreversible loss of energy to the environment as heat. $\mathcal{L}_{\text{rad}} = \mathcal{L}_{\text{rad}}^{\text{abs}} + \mathcal{L}_{\text{rad}}^{\text{emit}}$ respectively captures the absorption and emission (spontaneous or stimulated) processes.^{16,32} The efficiency of the light harvesting process can be rationalised in terms of how many quanta, as a proportion of those entering the FMO complex, are successfully trapped at the reaction centre. This is discussed further in Section 3.2.1.

$\mathcal{L}_{\text{bath}}$ describes the relaxation process of the system after photo-excitation, capturing the influence the bath has on it without explicitly defining the form of the bath. In order to account for the bath influence purely in terms of the system's degrees of freedom, the bath relaxation superoperator $\mathcal{L}_{\text{bath}}$ will take a functional form that is derived by making assumptions about how the system and bath interact.

This dynamical process, along with the unitary dynamics described by \mathcal{L}_{sys} , will be the focus of this thesis. How the bath influence is captured is introduced in Section 1.4, while the Lindblad quantum master equation (QME) used to model $\mathcal{L}_{\text{bath}}$ is introduced in Section 1.5. An alternative method to describing bath dynamics, based on a path-integral approach and known as the hierarchical equations of motion (HEOM) approach, is introduced in Section 1.6.

1.3.4 Time Evolution

Observing the dynamics of the system involves monitoring the evolution of the reduced density matrix elements over time. In order to do so, the equation of motion that describes their evolution needs to be integrated. The Liouvillian for open quantum systems in Equation 1.11, with $\mathcal{L} = \mathcal{L}_{\text{sys}} + \mathcal{L}_{\text{bath}}$, can be formally integrated to:

$$\rho(t_1) = \exp(\mathcal{L}dt)\rho(t_0), \quad (1.16)$$

for a time interval $dt = t_1 - t_0$. This provides an expression for the density matrix $\rho(t_1)$, formed by propagation of some initial state $\rho(t_0)$ forward in time by dt . By using a fixed interval dt the propagator is constant, allowing the full time-evolution of the density matrix ρ from some initial state $\rho(0)$ to be calculated by repeatedly applying the propagator at each timestep, rather than re-calculating the propagator at each step.¹⁷ Propagation occurs with the operators and states represented in *Liouville space*, allowing the evolution of each individual site population to be dependent on all elements of the density matrix. This is in contrast to working in *Hilbert space*, where there is only dependence on site coherences. Because site population transfers as part of non-unitary bath relaxation dynamics can occur other than just *via* coherences (i.e. through interactions with the bath), working in Liouville space as opposed to Hilbert space is appropriate. See Appendix B.3 for a demonstration of this.

1.3.5 Coherent Theories

Within the three chlorophyll bodies that make up the light harvesting architecture shown in Figure 1.1, the strengths with which the BChl sites interact with each other and with the surrounding protein environment is varied. The *coupling regime* the open quantum system occupies, defined as the relative strength of electronic (inter-site) couplings to system-bath coupling, determines the mechanism of energy transfer. Site interactions within the strong coupling regime result in excitonic transfer in a strongly coherent manner, whilst those in the weak coupling regime do so incoherently *via* a random walk or semi-classical ‘hopping’ mechanism.¹¹ The BChl sites in the FMO complex, however, occupy the intermediate coupling regime, where the energy scales of inter-site couplings and system-bath couplings are comparable.^{41,42} The FMO complex, as with other photosynthetic PPCs, exhibits some coherent

‘wave-like’ transfer of excitation energy.

In an experimental two-dimensional Fourier transform electronic spectroscopy study, Engel *et al.*²⁴ showed that at cryogenic temperature (77 K) there existed long-lasting coherences in the FMO complex, allowing it to “*sample relaxation rates from all component exciton states*”, and direct the energy transfer efficiently to the energy sink (i.e. site 3). Likened to a ‘quantum search algorithm’ (such as Grover’s algorithm used in quantum computation theory) this coherence transfer of site populations has been attributed to high efficiency of EET,^{11,21,34,43} but this is met with some disagreement^{39,44} and is very much still an open problem.

Important or not, experimental observation of coherence effects in the FMO complex warrants the use of a theory that can capture such phenomena when modelling EET *in silico*. Incoherent theories such as Förster theory, valid when system-bath coupling dominates over inter-system coupling, cannot do this.⁴⁵ Instead, a large body of literature within the field of quantum biology employs coherent theories such as the Lindblad QME or HEOM (introduced in Sections 1.5 and 1.6 respectively) to describe EET dynamics in systems such as the FMO complex.

1.4 Influence of the Bath

The complexity of the non-unitary bath relaxation dynamics of an open quantum system such as the FMO complex stems from its coupling to the bath, i.e. the surrounding protein environment. This is modelled as an infinite number of bosonic harmonic oscillators³⁶ that can couple to the electronic transitions (excitons) in the system. In order to describe the evolution of the reduced system’s density matrix without explicitly defining the bath’s degrees of freedom, the *influence* of the bath needs to be accounted for in a different way. This section discusses how this influence is described.

1.4.1 Harmonic Potentials

The ground and first excited states of each BChl molecule in the system can be modelled as harmonic potentials, V_g and V_e respectively, as seen in Figure 1.4a. The Franck-Condon principle of vertical electronic transitions is assumed, so that excitation of a BChl site in the system is instantaneous, and occurs with no change in configuration of the bath.⁷ It is only after some time that the bath changes configuration (or *reorganises*), resulting in

the vibronically excited BChl molecule relaxing to its vibrational ground state. The energy change associated with this relaxation is known as the *reorganisation energy*, λ , and is shown in Figure 1.4a.⁴⁶ For a more detailed, mathematical description of how the reorganisation energy and system-bath coupling strength, g , can be derived, see Appendix B.5.

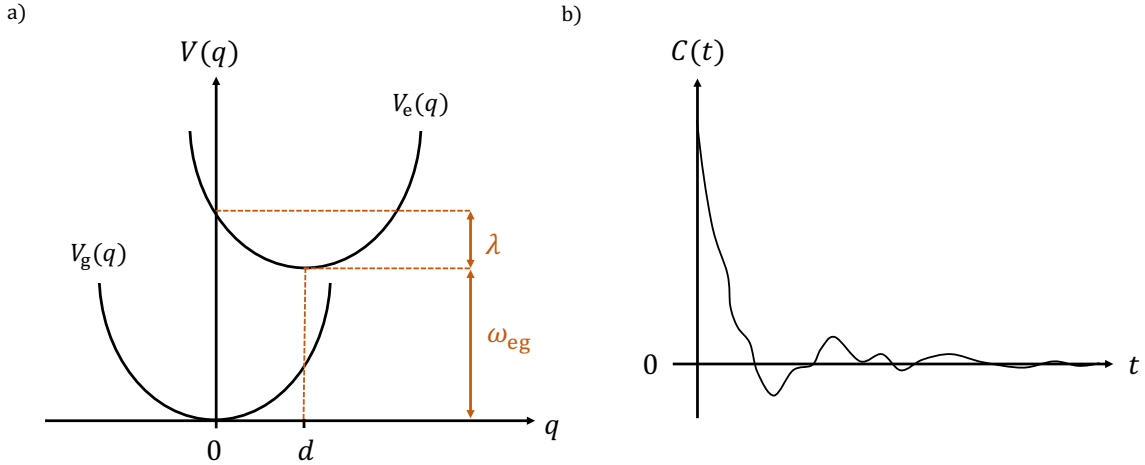


FIGURE 1.4: a) The ground and first excited electronic states of a BChl site as harmonic potentials, showing the difference in minimum energies between the two potentials, ω_{eg} , and reorganisation energy, λ , recreated from Figure 1 of Ishizaki and Fleming;⁴ b) the temporal correlation function of the dimensionless oscillator coordinates that decays with time.

1.4.2 Correlation Functions

Through system-bath coupling, any excitation in the system will have an effect on the bath (with an associated reorganisation energy) and will result in the bath having an influence back on the system that decays with time. This bath influence can be completely characterised by a temporal correlation function $C(t)$, as shown in Figure 1.4b. Due to its complicated functional form, and therefore usually not easy to work with, the temporal correlation function is more conveniently expressed in the frequency domain by taking the Fourier-Laplace transform:

$$C(\omega) = \int_0^\infty C(t) e^{-i\omega t} dt , \quad (1.17)$$

sometimes seen in the literature expressed as the imaginary part only,⁴ obtained by using Euler's formula, $\text{Im}(e^{-i\omega t}) = \sin(\omega t)$. For a bath of harmonic oscillators with dimensionless oscillator coordinates q , the correlation function in the frequency domain $C_{qq}(\omega)$ can be written as the sum of even and odd parts, $C'_{qq}(\omega)$ and $C''_{qq}(\omega)$ respectively. The odd part

takes the form:

$$C''_{qq}(\omega) = \frac{\pi}{2} (\delta(\omega - \tilde{\omega}) - \delta(\omega + \tilde{\omega})) , \quad (1.18)$$

and is related to the even part by:^{35,41}

$$C'_{qq}(\omega) = \coth\left(\frac{\beta\hbar\omega}{2}\right) C''_{qq}(\omega) . \quad (1.19)$$

The total correlation function can therefore be written purely in terms of the temperature independent odd part as:

$$C_{qq}(\omega) = \left[\coth\left(\frac{\beta\hbar\omega}{2}\right) + 1 \right] C''_{qq}(\omega) . \quad (1.20)$$

1.4.3 The Spectral Density

Being independent of temperature and related to the total correlation function by a constant, the odd part of the correlation function, $C''_{qq}(\omega)$, allows all information about the bath to be recovered. It is therefore used to define the *spectral density*, $J(\omega)$, which captures the influence of the harmonic bath on the system. Evaluated at a given electronic transition frequency between excitons in the system, ω , the spectral density is formed from the sum of all bath modes, ξ , with frequency of oscillation, ω_ξ , that are resonant to ω . The coupling strength between the system and bath is given by g_ξ , and the Dirac delta function (see Appendix A.4) ensures that, for a given exciton frequency ω , only resonant bath modes ($\omega_\xi = \omega$) contribute to the spectral density:^{8,39}

$$J(\omega) = \sum_{\xi} g_{\xi}^2 \delta(\omega - \omega_{\xi}) . \quad (1.21)$$

For a given exciton frequency ω , the greater number of resonant bath modes there are and the stronger they couple to the system, the larger the intensity of the spectral density. The coupling strength g_ξ and by extension the spectral density is usually approximated as being independent of site in the system, i , so that $g_\xi^{(i)} = g_\xi$ and $J_i(\omega) = J(\omega)$.⁸ The odd part of the correlation function can be written generally in terms of the spectral density, where the units defining the observable the correlation exists between is contained within a pre-factor but omitted here:

$$C''(\omega) = \frac{\pi}{2} (J(\omega) - J(-\omega)) . \quad (1.22)$$

The spectral density is usually defined only for positive frequencies,⁸ so that $J(\omega \leq 0) = 0$, with the odd part of the correlation function, by definition, picking up the negative transition frequencies with the $J(-\omega)$ term. The form of the spectral density can be approximated, with the most common form being the Debye¹ spectral density:^{5,17,39,47}

$$J_{\text{Debye}}(\omega) = 2\lambda \frac{\omega\gamma}{\omega^2 + \gamma^2} , \quad (1.23)$$

where γ is the bath relaxation rate.² It is related to the bath correlation time, τ_c , by $\gamma = 1/\tau_c$,^{14,48} and defines the frequency of the spectral density's peak. At frequencies $\omega > \gamma$ the spectral density decays to zero, and at frequencies $\omega < \gamma$ the spectral density is approximately linear in ω . The reorganisation energy, λ , can be recovered by the integration:²³

$$\lambda = \frac{1}{\pi} \int_0^\infty \frac{J(\omega)}{\omega} d\omega . \quad (1.24)$$

It is important to note that this definition only holds if the both the spectral density $J(\omega)$ and frequency ω are in angular frequency units (such as rad ps⁻¹). While the quotient $J(\omega)/\omega$ is dimensionless, integration occurs over the angular frequency ω , so the value for the reorganisation energy comes out in units of angular frequency. Other definitions are seen in the literature due to differences in unit conventions.

Use of approximate forms of the spectral density is controversial, with it being argued by Kell *et al.* that they are susceptible to displaying the incorrect behaviour and have ‘shapes’ (i.e. when plotted as a function of frequency, as seen in Figure 3.1) that are very sensitive to the PPC of interest.⁴⁷ However, due to there being “*no direct and detailed information on its form is available for the FMO complex at present*”⁴ (discussed further in Section 3.2.2), the Debye spectral density will be used in this thesis. It is a convenient way of detailing the influence of the bath on the system, and due to its versatility and intuitive form is widely used in similar theoretical studies into EET in photosynthetic PPCs.^{4,5,14,49} Only the spectral density parameters γ and λ (experimentally derived or otherwise) need to be set, without explicitly defining the bath’s degrees of freedom.

¹Otherwise known as the *Drude-Lorentz* or *overdamped Brownian* spectral density

²Also known as the *Drude decay constant* or the *cutoff frequency* (sometimes denoted by ω_c)

1.4.4 Population Transfer Rates

The Redfield theory expression, $k(\omega_{ab})$, represents the population transfer from exciton $a \rightarrow b$,²³ and is defined by the full Fourier-transform correlation function:⁸

$$k(\omega_{ab}) = C(\omega_{ab}) = 2 [(1 + n_{\text{BE}}(\omega_{ab}))J(\omega_{ab}) + n_{\text{BE}}(\omega_{ba})J(\omega_{ba})] ,^3 \quad (1.25)$$

where $n_{\text{BE}}(\omega)$ is the Bose-Einstein distribution, which for $\omega \neq 0$ is given by:⁸

$$n_{\text{BE}}(\omega) = \frac{1}{\exp(\beta\omega) - 1} ,^4 \quad (1.26)$$

and represents the dimensionless population ratio between two excitons separated in energy by ω , where $\beta = 1/k_B T$. If $\omega = \omega_{ab}$, then $n_{\text{BE}}(\omega_{ab})$ represents the population of b relative to a at a given temperature T . If exciton a is higher in energy than exciton b so that $\omega_{ab} > 0$, as the energy gap ω_{ab} approaches zero, or the temperature approaches infinity, the relative population of exciton b to exciton a approaches zero ($n_{\text{BE}}(\omega_{ab}) \rightarrow 0$); i.e. they are equally likely to be populated. On the other extreme, as the exciton energy separation approaches infinity, or the temperature approaches absolute zero, the Bose-Einstein distribution approaches infinity; exciton b approaches 100% likelihood of being populated relative to a .

The Redfield rate constant $k(\omega_{ab})$ is therefore dependent on temperature and the exciton energy difference between excitons involved in the population transfer, captured by $n_{\text{BE}}(\omega_{ab})$, as well as the strength of coupling between system and bath, captured by $J(\omega_{ab})$.

1.4.5 Thermal Equilibrium

After a sufficient time, a bath relaxation process will result in the system reaching a steady state. For bath relaxation dynamics described by a QME formed under the Born-Markov approximation, such as the Lindblad equation (see Section 1.5), a system in contact with a thermal bath of harmonic oscillators will have a steady state that corresponds to the *canonical thermal* state:^{18,49}

$$\rho_{\text{canon}} = \frac{e^{-\beta H_{\text{sys}}}}{\text{tr}(e^{-\beta H_{\text{sys}}})} , \quad (1.27)$$

where H_{sys} is the system Hamiltonian. In the infinite temperature limit as $T \rightarrow \infty$, the equilibrium state of the system is the *maximally mixed* state, which for an N -site system has

³ $\omega_{ab} = \omega_a - \omega_b$ and $\omega_{ba} = -\omega_{ab}$

⁴ $-n_{\text{BE}}(-\omega) = n_{\text{BE}}(\omega) + 1$

the form:¹⁶

$$\rho_{mm} = \frac{1}{N} \sum_{i=1}^N |i\rangle \langle i| , \quad (1.28)$$

or in matrix form

$$\rho_{mm} = \begin{bmatrix} \frac{1}{N} & 0 & \dots & 0 \\ 0 & \frac{1}{N} & \dots & 0 \\ \vdots & \vdots & \ddots & \vdots \\ 0 & 0 & \dots & \frac{1}{N} \end{bmatrix} . \quad (1.29)$$

This mixed state (a *statistical ensemble* of pure states) is *maximally* mixed because, mathematically speaking, its trace-squared value (a measure of the purity of a quantum state, see Appendix B.2) takes the lowest possible value of:

$$\text{tr} \left((\rho_{mm})^2 \right) = \frac{1}{N} . \quad (1.30)$$

Because this maximally mixed state is a scalar multiple of the identity matrix $\rho_{mm} = \mathbb{I}/N$, which is invariant under basis transformation, it can be concluded that physically the maximally mixed state is completely incoherent in every basis.

1.5 The Lindblad Quantum Master Equation

The Lindblad equation, developed by G. Lindblad in 1976,⁵⁰ and separately by Gorini and Kossakowski⁵¹ the same year, is a coherent theory that allows modelling of non-unitary dynamics of open quantum systems. Known as a completely-positive trace-preserving (CPTP) linear map, the Lindblad equation's properties allow the reduced system's density matrix to be evolved in time without destroying its state, ensuring the laws of quantum mechanics are abided by throughout the course of the evolution. Its utility comes with being able to model the bath-influenced relaxation dynamics of the system purely in terms of the system's degrees of freedom. The bath's degrees of freedom need not be explicitly defined; instead its influence is captured through the use of the spectral density (see Section 1.4). The Lindblad equation's general form, mathematical properties, and the approximations made in its derivation are outlined in this section.

1.5.1 General Form

Denoting the state of the system $\rho(t)$ as just ρ for brevity, the general form of the Lindblad equation for bath relaxation dynamics is given by:

$$\frac{\partial}{\partial t}\rho = (\mathcal{L}_{\text{sys}} + \mathcal{L}_{\text{bath}})\rho , \quad (1.31)$$

using the definition of the Hamiltonian commutation superoperator \mathcal{L}_{sys} given in Equation 1.13. The action of the Lindblad bath operator $\mathcal{L}_{\text{bath}}$ on the density matrix is given by:^{16,23}

$$\mathcal{L}_{\text{bath}}\rho = \sum_{\alpha} k_{\alpha} \left(A_{\alpha}\rho A_{\alpha}^{\dagger} - \frac{1}{2} \left\{ A_{\alpha}^{\dagger}A_{\alpha}, \rho \right\} \right) , \quad (1.32)$$

where $\{.,.\}$ denotes the anti-commutator relation (see section A.2.2). The explicit form of the Lindblad *superoperator* is:⁵²

$$\mathcal{L}_{\text{bath}} = \sum_{\alpha} k_{\alpha} \left(A_{\alpha}^* \otimes A_{\alpha} - \frac{1}{2} \left[(A_{\alpha}^{\dagger}A_{\alpha})^* \otimes \mathbb{I} + \mathbb{I} \otimes A_{\alpha}^{\dagger}A_{\alpha} \right] \right) , \quad (1.33)$$

where A_{α} are the Lindblad *operators*, while k_{α} represents some rate constant of the bath relaxation process, both of which take on different functional forms depending on the Lindblad model used. Three such models are discussed in later subsections, with functional forms of the operators and rate constants provided in Table 1.3.

1.5.2 Properties

In order to ensure the state of the density matrix is preserved after the action upon it by the Lindblad superoperator $\mathcal{L}_{\text{bath}}$, as in Equation 1.32, the mathematical form of the Lindblad superoperator itself must be a completely positive trace-preserving (CPTP) linear map. The details of these properties and the implications for the density matrix are outlined below.

Trace Preserving

The occupation number of the excitations within the system must be conserved. For a system in the single excitation manifold, the trace of the diagonal elements (which in the site basis represent probabilities that an exciton is localised on a given site) must therefore be equal to 1 at all times, i.e. $\text{tr}(\rho(t)) = 1$.

Positive Semi-Definite

When represented in the site basis, all diagonal elements of the density matrix must have non-negative values. Physically it would not sense for there to be a negative probability of a given site being excited. By extension, all of the eigenvalues must be non-negative. Upon action of the positive semi-definite Lindblad superoperator on the density matrix, all population probabilities and eigenvalues remain non-negative.

Linear

Suppose a time interval t_3 is defined such that it is the sum of two other time intervals $t_3 = t_1 + t_2$. Consider propagation of an initial state $\rho(0)$ with the exponentiated Lindblad superoperator (as in Equation 1.16) twice in succession for each of the time intervals t_1 and t_2 . Doing so (in either order) yields the same resultant density matrix as having applied it just once for the time interval t_3 , due to the linearity of the Lindblad superoperator.

$$\exp[\mathcal{L}t_3]\rho(0) = \rho(t_3) \quad (1.34)$$

$$\exp[\mathcal{L}t_2]\exp[\mathcal{L}t_1]\rho(0) = \exp[\mathcal{L}t_2]\rho(t_1) = \rho(t_1 + t_2) = \rho(t_3) \quad (1.35)$$

$$\exp[\mathcal{L}t_1]\exp[\mathcal{L}t_2]\rho(0) = \exp[\mathcal{L}t_1]\rho(t_2) = \rho(t_2 + t_1) = \rho(t_3) \quad (1.36)$$

1.5.3 Approximations

The assumptions and approximations about the dynamics of the system, as outlined below, allow the Lindblad equation to be derived. These are outlined below, and have very important implications for the resulting description of EET dynamics in the FMO complex. These will be discussed in Chapter 2.

Born

The timescale of system-bath correlations, τ_c , can persist for timescales on the same order as the system's evolution time, τ_{sys} . The Born approximation assumes that $\tau_c \ll \tau_{\text{sys}}$. For weak (or intermediate) system-bath coupling regimes, the interaction under this approximation is only valid up to terms that are second order in the coupling strength, g (see Equation 1.21).³⁸ This is therefore referred to as the *second order* Born approximation.³⁵

Markov

Many QMEs are formed under the Markov approximation, which assumes that the relaxation timescale of the bath is faster than any timescale associated with the dynamics of the system.^{38,40} A system undergoes *Markovian* behaviour in periods where there is continual flow of information into the bath (*memoryless* system dynamics), whilst *non-Markovian* behaviour occurs when there are correlations in time between system-bath interactions leading to back flow of information into the system. A Lindblad CPTP map defined over the time range $t_3 - t_1$ as:

$$\Omega_{t_3,t_1} = \exp [\mathcal{L}(t_3 - t_1)] \quad (1.37)$$

can be divided into CPTP maps over smaller time intervals, $t_3 - t_2$ and $t_2 - t_1$, such that it abides by the composition law:

$$\Omega_{t_3,t_1} = \Omega_{t_3,t_2} \Omega_{t_2,t_1} \quad (1.38)$$

and is said to induce Markovian dynamics for all $t_3 \geq t_2 \geq t_1$.^{38,53}

Secular

The secular approximation (also known as the *rotating-wave* approximation) can be applied by neglecting fast oscillating terms in the equation of motion for the reduced density matrix.³⁵ Taking the FMO complex as an example, a typical energy difference between excitons within its system Hamiltonian (with reference to Table 1.2) is on the order of 200 cm^{-1} , which translates to an intrinsic timescale for evolution of the system as 0.16 ps .⁵ This is an order of magnitude faster than the typical timescale of relaxation for such a system (usually on the order of 1 ps),²³ so the fast oscillating terms can be ignored and the secular approximation can be applied. This final approximation, when applied to the Redfield equation (the first Markovian QME derived in 1965 for applications in nuclear magnetic resonance⁵⁴), yields the Lindblad equation. It also ensures the property of complete positivity is fulfilled.³⁸

1.5.4 Construction of the Lindblad Operator

The dynamics of an open quantum system, considering only unitary dynamics governed by the system Hamiltonian H_{sys} and bath relaxation dynamics, is given by the Liouville equation

⁵ $(200 \times c)^{-1} \times 1 \times 10^{12} = 0.16 \text{ ps}$, where c is the speed of light in cm s^{-1}

in Equation 1.31:

$$\frac{\partial}{\partial t} \rho = (\mathcal{L}_{\text{sys}} + \mathcal{L}_{\text{bath}}) \rho ,$$

where the Liouville superoperator $\mathcal{L}_{\text{bath}}$ can be modelled by a Lindblad superoperator of explicit form (Equation 1.33):

$$\mathcal{L}_{\text{bath}} = \sum_{\alpha} k_{\alpha} \left(A_{\alpha}^* \otimes A_{\alpha} - \frac{1}{2} \left[\left(A_{\alpha}^{\dagger} A_{\alpha} \right)^* \otimes \mathbb{I} + \mathbb{I} \otimes A_{\alpha}^{\dagger} A_{\alpha} \right] \right) .$$

The Lindblad operators, A_{α} , and rate constants, k_{α} , take different functional forms depending on the Lindblad model used. In this section three Lindblad models will be discussed; the local dephasing, global thermalising, and local thermalising models, with a summary of their construction are given in Table 1.3.

Local Dephasing

- Superoperator $\mathcal{L}_{\text{bath}} = \mathcal{L}_{\text{deph}}$. Lindblad operator A_{α} evaluated for each **site** i .
- Constant dephasing rate Γ_{deph} independent of site.
- Termed *local* as each site couples directly to its own independent bath.

Global Thermalising

- Superoperator $\mathcal{L}_{\text{bath}} = \mathcal{L}_{\text{global}}$. Each Lindblad operator is constructed for a pair of distinct exciton **eigenstates** (a and b) of the system Hamiltonian H_{sys} .
- The Redfield rate constant term $k(\omega_{ab})$ represents the rate of population transfer between eigenstates $a \rightarrow b$, as given in Equation 1.25.
- $k(\omega_{ab})$ is dependent on the energy difference between eigenstates and the strength of coupling between system and bath as dictated by the spectral density $J(\omega_{ab})$, but is independent of site.
- Termed *global* as considers all sites as interacting with a shared (i.e. global) bath.

Local Thermalising

- Superoperator $\mathcal{L}_{\text{bath}} = \mathcal{L}_{\text{local}}$. Lindblad operators are constructed for every combination of site, i , and unique frequency gap between eigenstates of the system Hamiltonian, ω .

- All population transfers between eigenstates a and b whose energies are separated by the unique frequency gap the Lindblad operator is being constructed for (i.e. $\omega_{ab} = \omega_a - \omega_b = \omega$) are summed.
- Each of the population transfers $|b\rangle\langle a|$ that contributes to the construction of the Lindblad operator is weighted by a site contribution $c_i^*(b)c_i(a)$.
- $c_i(a)$ is the i th site coefficient of exciton (eigenstate) a of the system Hamiltonian, while $c_i^*(b)$ is the complex conjugate of the i th site coefficient of exciton b .
- The rate constant $k(\omega)$ represents the rate of population transfer between eigenstates separated by the unique frequency ω , and like the rate constant in the global thermalising model is independent of site.²³

Model	Index α	Lindblad Operator A_α	Rate k_α	Conditions
Local Deph. ¹⁶	i	$ i\rangle\langle i $	Γ_{deph}	$i \in \text{sites}\{1, \dots, N\}$
Global Therm. ^{16,55}	a, b	$ b\rangle\langle a $	$k(\omega_{ab})$	$a \neq b \in \text{eigs}(H_{\text{sys}})$
Local Therm. ²³	i, ω	$\sum_{\omega_a - \omega_b = \omega} c_i^*(b)c_i(a) b\rangle\langle a $	$k(\omega)$	$i \in \text{sites}\{1, \dots, N\}$ $a, b \in \text{eigs}(H_{\text{sys}})$ $\omega \in \text{uniq}\{\omega_{ab}\}$

TABLE 1.3: The Lindblad operators, rate constants, indices over which summation occurs, and conditions on the indices for the local dephasing, global thermalising, and local thermalising Lindblad models.

1.6 Hierarchical Equations of Motion

The Hierarchical Equations of Motion (HEOM) approach allows the evolution of the reduced system's density matrix in time to be monitored, capturing bath-influenced dynamics without making the perturbative Born-Markov or secular approximations.⁴⁰ This makes it a powerful tool for studying the dynamics of open quantum systems in contact with a harmonic bath.¹⁴ Being a numerically exact description of EET dynamics, it can serve as a benchmark for approximate QMEs such as the Lindblad equation.³⁹ HEOM was first derived by Tanimura and Kubo in 1989⁵⁶ and, like the Lindblad approach, makes the assumption that the system couples linearly to the bath's vibrational modes.

The key difference between the Lindblad equation and HEOM, however, is the ability of HEOM to capture *non-Markovian* dynamics. When the timescale of bath relaxation is not

fast relative to the timescale of the system's dynamics, there will exist correlations in the bath that have a time-dependent effect on the dynamics of the system. The Lindblad equation, formed under the Born-Markov approximation, is unable to capture this behaviour. This may be important in coupling regimes similar to those occupied by photosynthetic PPCs.

Originally derived to treat initially uncorrelated states (see Equation 1.9), Tanimura has recently extended the HEOM method to deal with correlated initial states,⁵⁷ improving the power and applicability of HEOM to different problems in open system dynamics where the former approximation may be invalid.⁵⁸ Despite this, it can be assumed that, in the case of instantaneous electronic excitation corresponding to a vertical Franck-Condon transition (i.e. in the FMO complex), the system and bath start off from an initially decoupled state.^{4,14}

1.6.1 Influence Functional

Based on Feynman's path integral formalism,⁵⁹ HEOM makes use of the Feynman-Vernon influence functional⁶⁰ to account for the effect of the bath on the system's dynamics. Formation of this functional occurs *via* integration over all bath degrees of freedom (i.e. all possible *paths* available for the system and bath to couple). Paired with use of a spectral density, such as the Debye form in Equation 1.23, the influence of the bath on the system can be captured without explicitly defining the bath's degrees of freedom. This, much like the Lindblad equation, allows an equation of motion for the reduced system's density matrix $\rho(t)$ to be formed purely in terms of the system's degrees of freedom.

Using a Debye spectral density, the temporal bath correlation function can be expressed as an infinite sum of weighted exponentials,³⁹ which is assumed to be site independent so that $C_j(t) = C(t)$:

$$C(t > 0) = \sum_{k=0}^{\infty} c_k e^{-\nu_k t}. \quad (1.39)$$

The forms of Matsubara coefficients, c_k , and frequencies, ν_k , are given in Appendix B.6.1. The important relations to note, however, are that as $k \rightarrow \infty$, $\nu_k \rightarrow \infty$ and $c_k \rightarrow 0$. This results in the exponential decay of terms in the correlation function (i.e. $c_k e^{-\nu_k t} \rightarrow 0$ as $k \rightarrow 0$). Due to negligible contributions of terms at high values of k , a bath correlation cutoff, K , can be introduced when computationally evaluating the bath correlation function.¹⁴ In practice, this can be a relatively small finite value ($K < 5$) that still accurately captures the bath influence *via* its correlation function.

1.6.2 Auxiliary Density Matrices

The ability of HEOM to describe non-Markovian behaviour comes from its use of *auxiliary density matrices* (ADMs). In the HEOM formalism, these density matrices are distinguished from one another, and from the system's reduced density matrix (RDM), by their vector index \mathbf{n} , which takes the general form:^{14,41}

$$\mathbf{n} = \{\{n_{10}, \dots, n_{1k}, \dots, n_{1K}\}, \dots, \{n_{i0}, \dots, n_{ik}, \dots, n_{iK}\}, \dots, \{n_{N0}, \dots, n_{Nk}, \dots, n_{NK}\}\} \quad (1.40)$$

where the elements n_{ik} are non-negative integers. The RDM, $\sigma_{\mathbf{n}=0} = \rho(t)$, is the density matrix of interest, describing the state of the system (i.e. the FMO complex) with the site population probabilities and coherences. It is indexed by $\mathbf{n} = 0 = \{\{0, \dots, 0\}, \dots, \{0, \dots, 0\}\}$. The ADMs, on the other hand, are mathematical accessories that have no physical meaning (i.e. they are **not** quantum states⁴⁸) but contribute corrections to the dynamics of the system to account for non-Markovian effects. They correspond to all density matrices that have non-zero values for any of the vector index elements n_{ik} , i.e. $\sigma_{\mathbf{n} \neq 0}$. The index $i \in \{1, \dots, N\}$ can take N possible values (the number of sites in the system), while the index $k \in \{0, \dots, K\}$ takes $(K + 1)$ possible values (where K is the bath cutoff). Therefore, the number of *distinct elements* in the vector index in Equation 1.40 is equal to $N(K + 1)$. For example, for a 2-site system ($N = 2$), with a bath cutoff of $K = 3$, there exists 8 distinct vector index elements, $\mathbf{n} = \{\{n_{10}, n_{11}, n_{12}, n_{13}\}, \{n_{20}, n_{11}, n_{12}, n_{13}\}\}$, each of which has a non-negative integer value. Each density matrix, indexed by \mathbf{n} , belongs to a hierarchy level, L . This is defined as the sum of all the elements that comprise its vector index:^{14,39}

$$L = \sum_{i=1}^N \sum_{k=0}^K n_{ik} . \quad (1.41)$$

The system's RDM, $\sigma_{\mathbf{n}=0} = \rho(t)$, with all elements in its vector index equal to 0, belongs to the $L = 0$ hierarchy level. Because there is only one way of attaining a value of $L = 0$, the RDM is the only matrix that occupies this level. All ADMs, on the other hand, occupy higher levels in the hierarchy. Using the values above with $N = 2$ and $K = 3$, an ADM with index $\mathbf{n} = \{\{0, 1, 0, 0\}, \{1, 0, 0, 1\}\}$, for example, belongs to the $L = 3$ hierarchy level.

1.6.3 Hierarchy Truncation

Evaluation of an infinite number of ADMs is computationally impossible. Fortunately, in practice, numerical convergence of HEOM can be achieved for evaluation of a finite number of ADMs, the number of which is determined by the hierarchy truncation level, \mathcal{N}_c .³⁹ This sets a limit for the highest hierarchy level, L , an ADM can belong to if it is to be evaluated with HEOM. For example, setting $\mathcal{N}_c = 0$ will only evaluate the system's reduced density matrix at each given timestep and will therefore not capture any non-Markovian effects. However, setting $\mathcal{N}_c > 0$ will capture these effects (to some extent) by evaluating some ADMs as well as the system's reduced density matrix.

The greater the non-Markovian effects on the dynamics of an open quantum system, the more ADMs that are required for numerical convergence of HEOM.¹⁴ Convergence is achieved when the evolution of the system's reduced density matrix no longer changes upon increases of the bath cutoff, K , and hierarchy truncation level, \mathcal{N}_c . The value of \mathcal{N}_c required for convergence is sensitive to system size and parameters (which determine the degree of non-Markovianity present), so must be determined on a case-by-case basis. Even with a small bath cutoff and truncation level, the computational expense of HEOM can be very large when compared to QMEs such as the Lindblad equation, which only consider propagation of one density matrix at each timestep (see Equation 1.16). The full hierarchical equations of motion for the auxiliary density matrices $\sigma_{\mathbf{n}}$ are given by:^{5,39}

$$\begin{aligned} \frac{d}{dt}\sigma_{\mathbf{n}} = & \left(\mathcal{L}_{\text{sys}} - \sum_i^N \sum_k^K n_{ik} \nu_k \right) \sigma_{\mathbf{n}} \\ & - i \sum_i^N \left[\mathcal{V}_i, \sum_k^K \sigma_{\mathbf{n}_{ik}^+} \right] \\ & - i \sum_i^N \sum_k^K n_{ik} \left(c_k \mathcal{V}_i \sigma_{\mathbf{n}_{ik}^-} - c_k^* \sigma_{\mathbf{n}_{ik}^-} \mathcal{V}_i \right) . \end{aligned} \quad (1.42)$$

\mathcal{L}_{sys} is the Hamiltonian commutation superoperator (Equation 1.13) describing unitary evolution governed by the molecular exciton system Hamiltonian (Equation 1.1). $\mathcal{V}_i = |i\rangle\langle i|$ ^{4,41} represents the system operator in the interaction Hamiltonian (Equation 1.7), and $[.,.]$ denotes the commutator relation (see Section A.2.2). $\sigma_{\mathbf{n}_{ik}^+}$ and $\sigma_{\mathbf{n}_{ik}^-}$ represent density matrices at hierarchy levels 1 higher and 1 lower (respectively) than the matrix indexed by \mathbf{n} , formed by raising or lowering the element n_{ik} in the vector index by 1. This inter-dependence between

hierarchy levels makes the HEOM highly coupled, owing to its computational expense.¹⁴

Any ADMs that occupy a hierarchy level higher than the truncation level, i.e. $L > \mathcal{N}_c$, can either be evaluated to zero (known as the time-nonlocal truncation), or treated with the Markov approximation (the time-local truncation), with the latter allowing for more accurate results.¹⁴ The number of ADMs that are evaluated at each timestep increases ever more rapidly with increasing hierarchy truncation level, \mathcal{N}_c .¹⁴ The truncation level needed for numerical convergence will depend on the system and parameter set used, and may be very high and therefore computationally expensive. In this case, a lower truncation level may be decided upon that balances the convergence tolerance with computational expense.

Chapter 2

Results and Discussion

Due to HEOM's computational expense when scaled to larger systems, QMEs such as the Lindblad equation are sought after as alternative descriptions of the dynamics of open quantum systems because they are tractable, computationally cheap, easy to implement, and analytically soluble.

Despite these advantages, the approximations made in deriving the general form of Lindblad equation, as well as those imposed in defining the specific forms of each Lindblad model, provide potential for the Lindblad models to fall short in accurately describing the bath relaxation dynamics of the EET process in the FMO complex. Their effectiveness in capturing such a dynamical process needs to be rationalised, and can be done so by benchmarking the Lindblad models against the HEOM approach.

In the first section of this chapter, the approximations used to form the Lindblad operators and their implications for EET will be explored for a 2-site system. In the next, the Lindblad models will be benchmarked against HEOM in their ability to describe EET dynamics in the 7-site FMO complex.

All plots have been generated using *quantum_HEOM* (github.com/jwa7/quantum_HEOM), an open-source Python package written by the author, which can also be used to easily reproduce most of the plots in the following 2 chapters of this thesis. See Appendix C for details and examples.

2.1 Model 2-Site System

In this section, the Lindblad dynamics of an open quantum system will be benchmarked against the HEOM approach. At the time of writing, *QuTiP*'s HEOM Solver⁶¹ only allows the HEOM dynamics to be solved for 2-site systems described by a spin-boson Hamiltonian and Debye spectral density, with the system and bath states initially uncorrelated. Benchmarking calculations will therefore be performed for a model 2-site system, with a Debye spectral density used throughout. In each case of plotting with the HEOM approach, the bath correlation function cutoff, K , and hierarchy truncation, \mathcal{N}_c , were determined on a case-by-case basis to achieve numerical convergence of results.

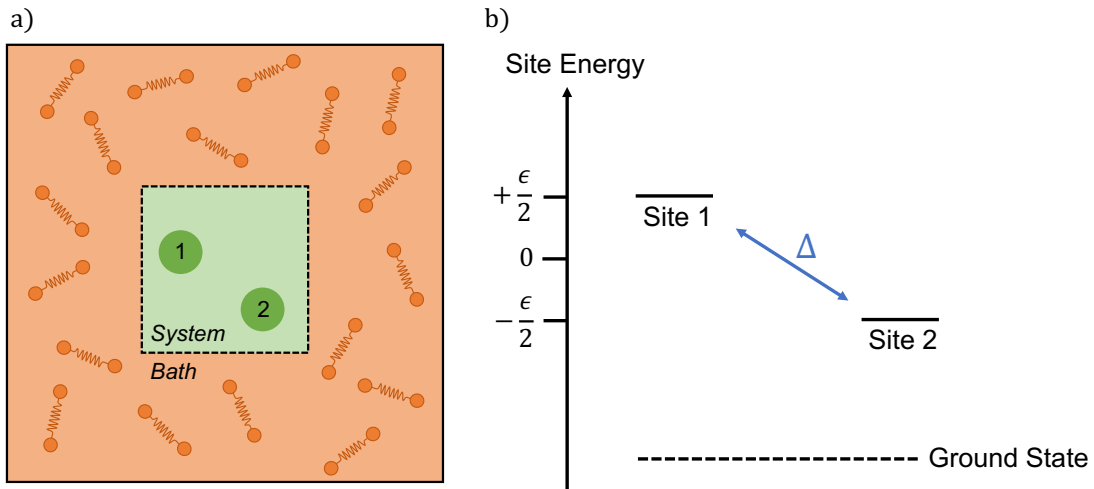


FIGURE 2.1: a) The model 2-site system and harmonic bath used in Lindblad-HEOM benchmarking; b) an energy level schematic of the two sites where site 1 has been arbitrarily defined as having a higher energy than site 2. Site energies are equally distributed around zero, separated by ϵ , in accordance with the spin-boson system Hamiltonian. Tunneling between sites, of strength Δ , is indicated with the double-headed arrow.

2.1.1 The Spin-Boson Hamiltonian

Consider a system consisting of two sites, $|1\rangle$ and $|2\rangle$, surrounded by a thermal bath of harmonic oscillators (Figure 2.1a). $|1\rangle$ can be arbitrarily defined as having a higher exciton (or *site*) energy than $|2\rangle$. The site energies are equally distributed around zero so that $\epsilon_1 = +\epsilon/2$ and $\epsilon_2 = -\epsilon/2$, with the separation given by $\epsilon = \epsilon_1 - \epsilon_2$. This is shown in an energy level diagram in Figure 2.1b (see also Appendix B.1). The system Hamiltonian takes the *spin-boson*

form:^{18,46}

$$H_{\text{sys}} = \frac{\epsilon}{2}\sigma_z + \frac{\Delta}{2}\sigma_x , \quad (2.1)$$

with Δ defining the strength of interaction (or *tunneling*) between sites. The (2×2) σ_z and σ_x Pauli matrices are given by:

$$\sigma_z = \begin{bmatrix} 1 & 0 \\ 0 & -1 \end{bmatrix} , \quad \sigma_x = \begin{bmatrix} 0 & 1 \\ 1 & 0 \end{bmatrix} , \quad (2.2)$$

with the system-bath coupling operator that forms part of the interaction Hamiltonian (see Equation 1.7) also given by σ_z . The dynamics of a closed quantum system, where only interactions between sites exist and the influence of a surrounding thermal bath is not considered, is governed completely by the system Hamiltonian H_{sys} . The state of the system is evolved according to the Liouville-von Neumann equation in Equation 1.14, with $\mathcal{L} = \mathcal{L}_{\text{sys}}$. Starting from a pure state, for example with excitation localised on site 1:

$$\rho(0) = \begin{bmatrix} 1 & 0 \\ 0 & 0 \end{bmatrix} , \quad (2.3)$$

the system will remain in a pure state indefinitely so that $\text{tr}(\rho(t)^2) = 1$ for all t . No mixedness in the quantum state will arise as there exists no interaction with a thermal environment. The result is unitary evolution of the density matrix elements, which oscillate indefinitely in time (Figure 2.2).

For an open quantum system, however, where bath relaxation dynamics are now considered (so that $\mathcal{L} = \mathcal{L}_{\text{sys}} + \mathcal{L}_{\text{bath}}$), mixedness in the quantum state of the system will be induced over time. This can be seen in Figure 2.3 for all Lindblad and HEOM models, where the initially pure state in Equation 2.3 becomes mixed through interaction with the bath. Notice that while the time-dependence of the purity varies for each model, the purity does not drop lower than the minimum value of $1/N = 0.5$ in any case.

While the mixedness of the quantum state can be monitored as a function of time, it does not provide any indication of exciton delocalisation over the course of an evolution. This instead can be monitored by the inverse participation ratio of the state, which is distinct from

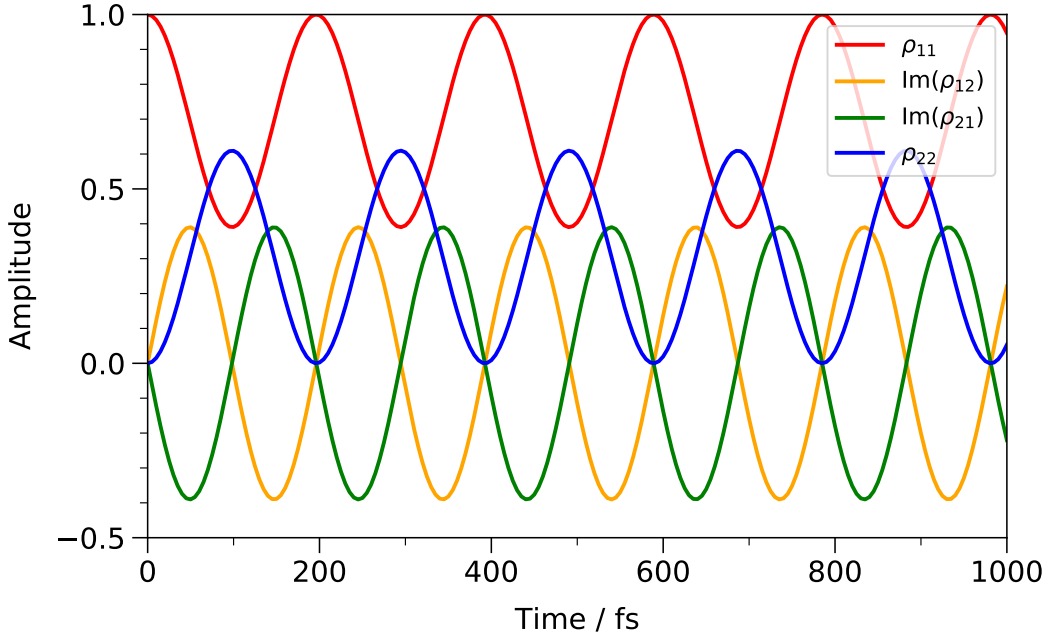


FIGURE 2.2: Unitary evolution of the density matrix elements of a 2-site closed quantum system governed by the spin-boson system Hamiltonian, with $\epsilon = 20 \text{ rad ps}^{-1}$, $\Delta = 35 \text{ rad ps}^{-1}$, and initial excitation on site 1. Real site populations and imaginary parts of site coherences are plotted.

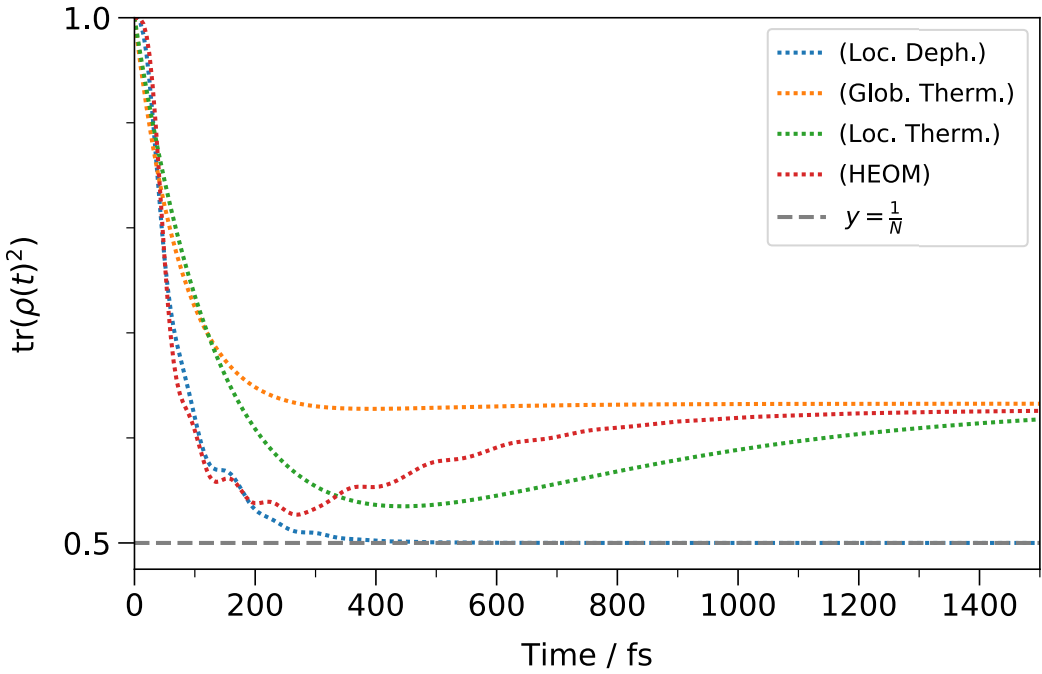


FIGURE 2.3: The 1.5 ps evolution of the purity of a 2-site open quantum system described by each of the Lindblad models and HEOM. Bath interactions induce mixedness in the state of the system over time. Parameters: $T = 300 \text{ K}$, $\epsilon = 40 \text{ rad ps}^{-1}$, $\Delta = 20 \text{ rad ps}^{-1}$, $\gamma = 20 \text{ rad ps}^{-1}$, $\lambda = 2 \text{ rad ps}^{-1}$, $\Gamma_{\text{deph}} = 11 \text{ rad ps}^{-1}$.

the IPR of the system Hamiltonian eigenstates in Section 1.2.2, and is instead defined as.^{31,62}

$$\text{IPR}(\rho) = \frac{(\sum_{i,j} |\rho_{ij}|)^2}{N(\sum_{i,j} |\rho_{ij}|^2)} , \quad (2.4)$$

which takes values $1/N \leq \text{IPR}(\rho) \leq N$, where N is the number of sites in the system and ρ_{ij} is a density matrix element. A value of 1, which is the IPR of the maximally mixed state, ρ_{mm} , corresponds to a completely incoherent (in any basis) and fully localised state. This is in contrast to a completely coherent and fully delocalised state which has an IPR value of N .¹⁶ Values between $1/N$ and 1, however, represent states that are localised but not completely incoherent, having some coherence in some basis. An example is the initial state in Equation 2.3, which has no coherence in the site basis but isn't completely incoherent (i.e. not a scalar multiple of the identity).

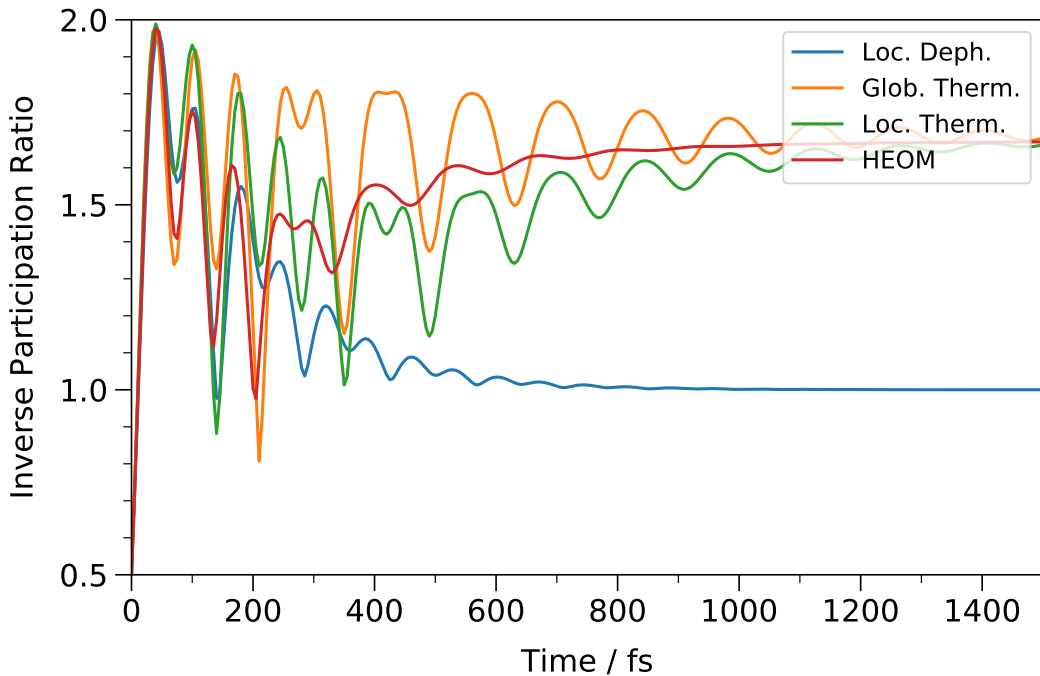


FIGURE 2.4: The 1.5 ps evolution of the inverse participation ratio (IPR) of quantum states for each Lindblad model and HEOM. Parameters used as in Figure 2.3.

Figure 2.4, which plots the IPR of the state as a function of time, shows that EET for all Lindblad models and HEOM begins with an initial (almost) complete delocalisation of the excitonic energy across both of the sites, reaching $\text{IPR}(\rho) \sim 2$ at 75 fs. This is followed by oscillatory localisation-delocalisation behaviour followed by equilibration to a steady state for all models. The forms of these steady states will be discussed in more detail below.

2.1.2 Key Features of the Lindblad Models

The key features of each Lindblad model as a consequence of the specific mathematical forms of their Lindblad operators A_α and rate constants k_α (Table 1.3) will be discussed in this

subsection with reference to the HEOM approach. For illustrative purposes, the system Hamiltonian and (Debye) spectral density parameters have been fixed for all models; $\epsilon = 20$, $\Delta = 40$, $\gamma = 20$, $\lambda = 1$, $\Gamma_{\text{deph}} = 7 \text{ rad ps}^{-1}$, $T = 300 \text{ K}$. Where Lindblad and HEOM have been compared, the density matrix elements for the latter have been underlaid in a dotted line, and only the site 1 population ρ_{11} and site coherence ρ_{21} are plotted for clarity. Note the symmetry relationship of the density matrix elements for a 2-site system, i.e. that $\rho_{22}(t) = 1 - \rho_{11}(t)$ and $\rho_{12}(t) = \rho_{21}^*(t)$ where $*$ denotes the complex conjugate.

Local Dephasing Lindblad

When $\mathcal{L}_{\text{bath}} = \mathcal{L}_{\text{deph}}$, the system is treated as being in the infinite temperature limit ($T \rightarrow \infty$). In such a limit, information about the relative energies of the sites is destroyed and consequently the steady state of the system has all sites equally populated. The steady state therefore corresponds to the *maximally mixed* state:

$$\rho_{\text{mm}} = \begin{bmatrix} \frac{1}{2} & 0 \\ 0 & \frac{1}{2} \end{bmatrix}, \quad (2.5)$$

taking the lowest possible trace-squared value $\text{tr}(\rho_{\text{mm}}^2) = 1/N = 1/2$ (as seen in Figure 2.3). As stated in Section 1.4.5, the maximally mixed state is a scalar multiple of the identity matrix, representing complete loss of coherence in any basis, so has an IPR value of 1. This can be seen as the steady state reached in Figure 2.4.

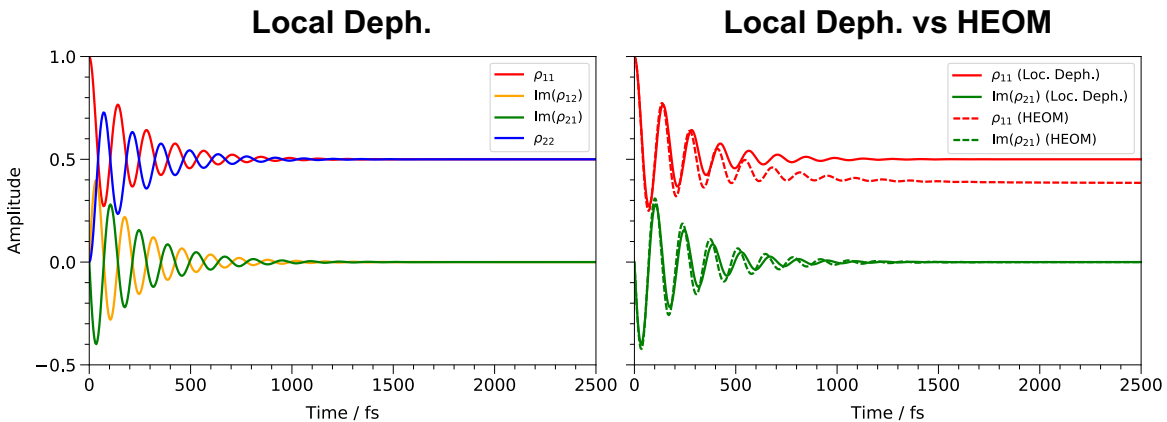


FIGURE 2.5: Left: the 2.5 ps evolution of the density matrix elements of the model 2-site system, described by the local dephasing Lindblad model. Right: the evolution of the site 1 population ρ_{11} and site coherence ρ_{21} compared to HEOM.

The non-unitary bath relaxation dynamics of the model 2-site system are shown in Figure 2.5. The system assumes the steady state after approximately 1 ps, where the loss of coherence (or *decoherence*) can be seen by decay (or *dephasing*) of the imaginary amplitudes of elements ρ_{12} and ρ_{21} to zero, whilst the real site populations ρ_{11} and ρ_{22} decay to an equal population probability of 0.5.

In the case where the sites are degenerate ($\epsilon = 0$), the dephasing model will be able to correctly predict the equilibration of the site populations. It is also clear that the appropriate choice of dephasing rate can give good qualitative agreement in the coherence transfers (shown by the modulation of site population amplitudes) at short timescales (< 300 fs). However, while the dephasing may be able to capture the short-term coherence behaviours in the FMO complex, it is unlikely to ever be successful in capturing the equilibrium behaviour in real systems, particularly large ones. Local protein environments naturally result in different site energies, and as soon as there is a break in degeneracy of site energies, or a deviation away from infinite temperature, the dephasing model at long times becomes invalid.

Global Thermalising Lindblad

The global thermalising model, in contrast to the dephasing model, equilibrates to the ‘correct’ canonical thermal state, defined only by the system Hamiltonian and bath temperature (Equation 1.27). This can be seen by comparison with HEOM in Figure 2.6, which for this parameter set also equilibrates to the canonical thermal state.

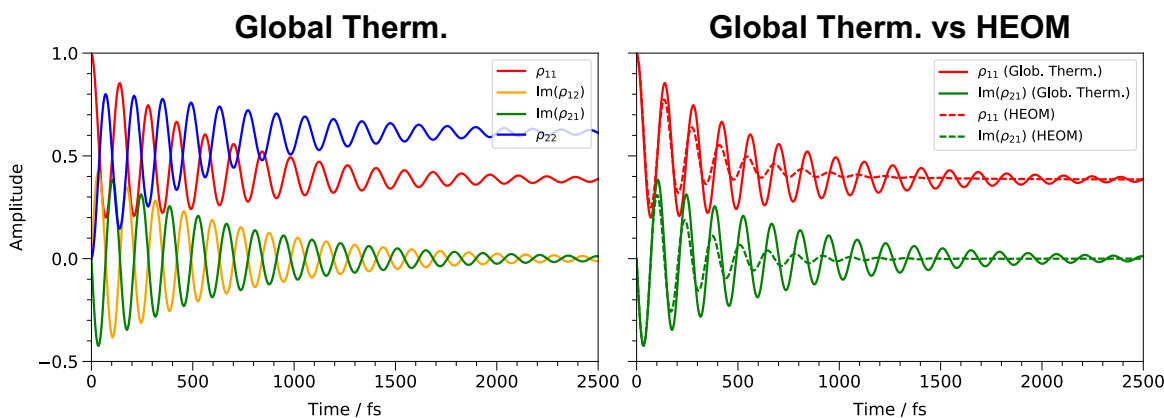


FIGURE 2.6: Left: the 2.5 ps evolution of the density matrix elements of the model 2-site system, described by the global thermalising Lindblad model. Right: the evolution of the site 1 population ρ_{11} and site coherence ρ_{21} compared to HEOM.

The Redfield rate constant, $k(\omega)$, in Equation 1.25, considers population transfer between distinct excitons that depends only their difference in energy (and system-bath coupling captured by the spectral density). With inter-site distances and couplings not considered, the global model equilibrates to the canonical thermal states even in cases where it shouldn't. This behaviour can be easily illustrated with an edge-case example. Consider the 2 sites in the system to be at infinite separation so that the coupling between them is zero (i.e. $\Delta \rightarrow 0$ as $r_{12} \rightarrow \infty$). Zero inter-site coupling means there would be no transfer of population between them. In this case, if starting in the pure state in Equation 2.3, site 1 should remain populated with 100% probability, site 2 with 0%, and the state should remain indefinitely pure. Simulating this situation by setting the tunneling strength to zero in the spin-boson Hamiltonian, the global thermalising model shows transfer of population between sites and equilibration of the system to the thermal state; a direct result of its negligence for inter-site distances and couplings.

While not obvious in the case of the model 2-site system, this may cause problems in the effectiveness of the model in describing EET in larger systems such as the FMO complex where distances and couplings become important.

Local Thermalising Lindblad

Equilibrating to the canonical thermal state like the global model, the local thermalising model better accounts for inter-site couplings through weighting each transfer of population between eigenstates by a site contribution, $c_i^*(b)c_i(a)$, which describes the i th site coefficient in the b th and a th exciton respectively. In the extreme case of sites at infinite separation described above, this site contribution factor will be zero, resulting in no transfer of population between eigenstates and therefore no equilibration of the model. This is the behaviour that one would expect.

The combination of equilibration to the ‘correct’ canonical thermal state, as well as taking into account site distances and couplings makes the local model a promising middle ground between the dephasing and global models.

2.1.3 Trace Distance

In order to assess the performance of the Lindblad approach with respect to HEOM in a more rigorous way than simple qualitative comparison, it would be convenient to define a measure of

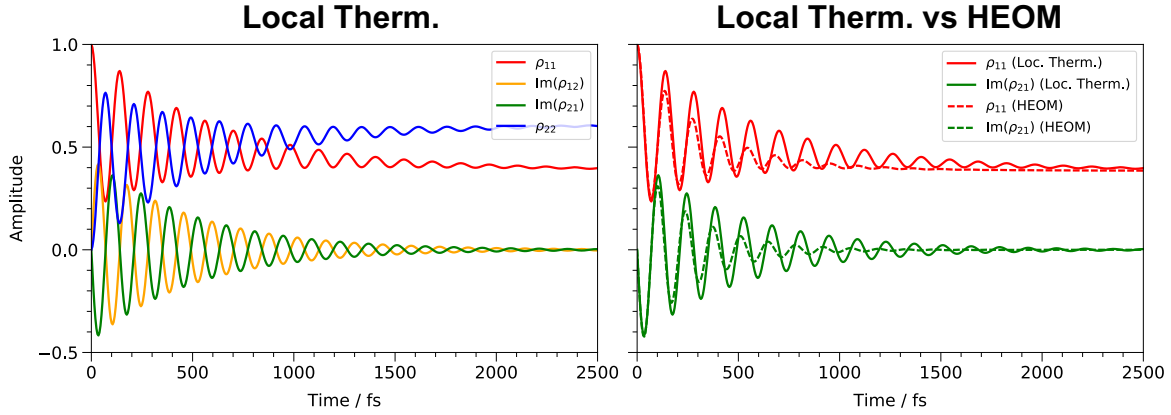


FIGURE 2.7: Left: the 2.5 ps evolution of the density matrix elements of the model 2-site system, described by the local thermalising Lindblad model. Right: the evolution of the site 1 population ρ_{11} and site coherence ρ_{21} compared to HEOM.

similarity between quantum states evolved by each of the approaches. This metric is known as the *trace distance* $D(\rho_1, \rho_2)$, introduced by Breuer *et al.*⁶³ to quantify the similarity between two quantum states ρ_1 and ρ_2 . It is given by:

$$D(\rho_1, \rho_2) = \frac{1}{2}\text{tr}|\rho_1 - \rho_2| , \quad (2.6)$$

where the norm of a matrix A is $|A| = \sqrt{A^\dagger A}$. $D(\rho_1, \rho_2)$ can take values $0 \leq D \leq 1$, equal to zero if and only if $\rho_1 = \rho_2$ (indistinguishable), while a value of 1 indicates the states are orthogonal (maximally distinguishable).⁴⁸ D can be plotted as a function of time to observe the similarity of a quantum state $\rho_1 = \rho(t)$ to a reference state $\rho_2 = \rho^{\text{ref}}(t)$. The trace distance can be integrated with respect to t over some time interval τ and divided through by the time interval to give a mean trace distance metric, Q :

$$Q = \frac{1}{\tau} \int_0^\tau dt \frac{1}{2}\text{tr}|\rho(t) - \rho^{\text{ref}}(t)| , \quad (2.7)$$

that, like D , takes values $0 \leq Q \leq 1$ but quantifies the similarity of a density matrix $\rho(t)$ to a reference state $\rho^{\text{ref}}(t)$ over the course of a whole evolution.^{17,53} The form of the reference state dictates the behaviour that is being observed. In the following two subsections, different forms of the reference state are used to observe non-Markovian and non-canonical equilibrium behaviours.

2.1.4 Non-Markovianity

The trace distance metric can be used as a concrete way of determining whether the EET dynamics of a system exhibits non-Markovian behaviour.¹⁸ Consider a 2-site system $\rho^{(1)}(t)$ that has been initially excited on site 1 (i.e. $\langle 1 | \rho^{(1)}(0) | 1 \rangle = 1$):

$$\rho^{(1)}(0) = \begin{bmatrix} 1 & 0 \\ 0 & 0 \end{bmatrix}, \quad (2.8)$$

and a second system $\rho^{(2)}(t)$ that has been initially excited on site 2 (i.e. $\langle 2 | \rho^{(2)}(0) | 2 \rangle = 1$):

$$\rho^{(2)}(0) = \begin{bmatrix} 0 & 0 \\ 0 & 1 \end{bmatrix}. \quad (2.9)$$

The trace distance between these two quantum states as a function of time, plotted for each of the Lindblad models and HEOM, is shown in Figure 2.8. A monotonically decreasing

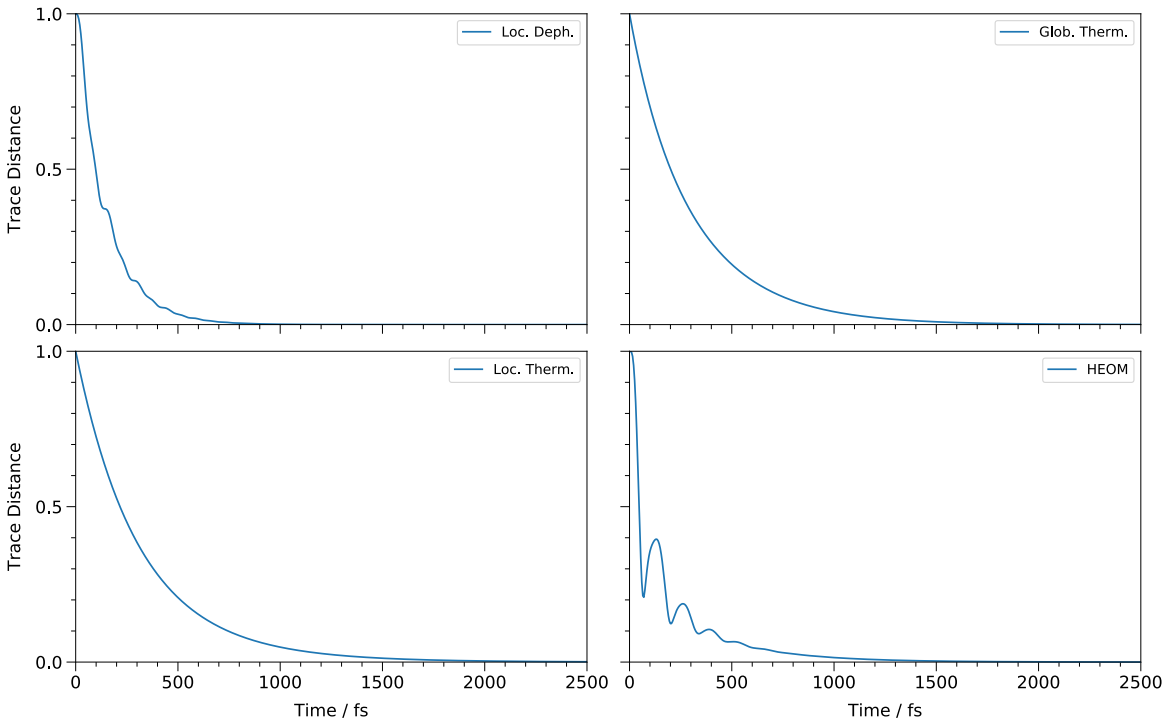


FIGURE 2.8: The time-evolution of the trace distance between states $\rho^{(1)}(t)$ and $\rho^{(2)}(t)$, where each has a different initial excitation, $\langle 1 | \rho^{(1)}(0) | 1 \rangle = 1$ and $\langle 2 | \rho^{(2)}(0) | 2 \rangle = 1$, plotted for each Lindblad model and HEOM. Monotonically decreasing curves (Lindblad) suggests purely Markovian behaviour, whereas regions of positive derivative indicates non-Markovian behaviour.

(i.e. non-positive derivative at all points on the curve) trace distance as a function of time is indicative of purely-Markovian behaviour. This is the behaviour exhibited by all of the

Lindblad models, in alignment with the expectation of the Lindblad equation to do so under the Born-Markov approximation. It is clear, however, that the trace distance curve for HEOM isn't monotonically decreasing throughout the evolution; there are regions of positive derivative that indicate periods of non-Markovian behaviour. While it should be noted that the HEOM approach has the ability to capture non-Markovian behaviour, this does not necessarily mean that it will be exhibited. The fact that the system, for this set of parameters, exhibits non-Markovian behaviour that isn't captured by the Lindblad highlights a potential shortcoming of the Lindblad in its ability to accurately describe the bath relaxation dynamics of EET.

In order to more easily visualise the difference between Lindblad and HEOM models as a result of non-Markovian effects, the trace distance between states for the different models (rather than different states for the same model as in Figure 2.8) can be monitored. For example, the similarity between a quantum state being evolved in time by the Lindblad CPTP map, $\rho_1 = \rho^{\text{Lind}}(t)$, and a reference state being evolved by HEOM dynamics, $\rho_2 = \rho^{\text{HEOM}}(t)$, can be observed with the modified form of Equation 2.6:

$$D(t) = \frac{1}{2} \text{tr} |\rho^{\text{Lind}}(t) - \rho^{\text{HEOM}}(t)| . \quad (2.10)$$

In a similar manner to above, graphical regions of positive derivative are indicative of non-Markovian behaviour that the Lindblad, formed under the Born-Markov approximation, is failing to capture.⁵³ Regions of zero or negative derivative, however, represent periods of Markovian behaviour. If the system's evolution is purely Markovian at all times, the trace distance curve as function of time should remain at zero. A comparison of the evolution of the site 1 population in a 2-site system (with $\epsilon = 0$ and $\Delta = 50$) described by local thermalising Lindblad and HEOM can be found in the top left panel of Figure 2.9, with the Lindblad-HEOM trace distance curves (as in Equation 2.10) plotted for every Lindblad model in the top right panel.

Starting from the same initial state, $\langle 1 | \rho^{(1)}(0) | 1 \rangle = 1$, at time $t = 0$, the Lindblad-HEOM trace distance is zero for all models in the top right plot of Figure 2.9. Over time, the Lindblad states deviate from the HEOM state, indicating periods of non-Markovian behaviour. Towards the end of the 1 ps evolution, it is apparent that the local dephasing model is equilibrating to the incorrect maximally mixed state, indicated by the trace distance assuming

a steady value just below 0.3. The thermalising models, on the other hand, equilibrate to the canonical thermal state. The difference in equilibrium behaviour between the dephasing and thermalising Lindblad models is reflected in the average trace distance metric, Q , in Equation 2.7, which is 0.25 for the dephasing model and 0.12 and 0.07 for the local and global thermalising models respectively.

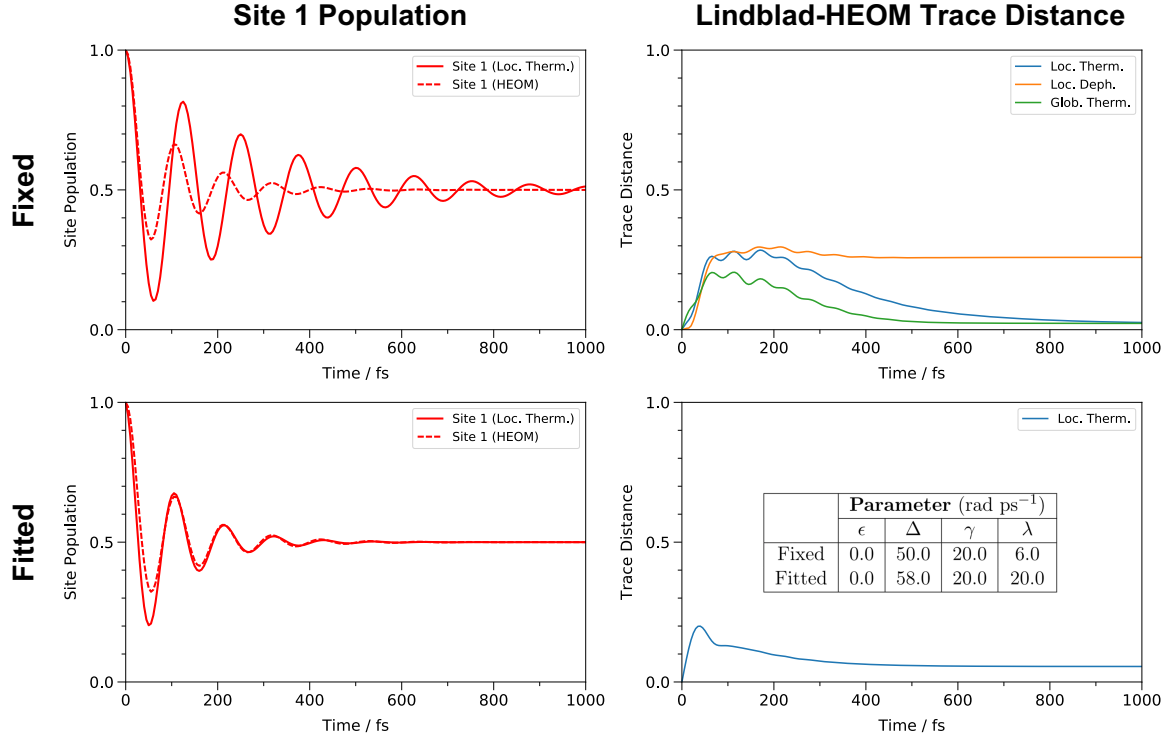


FIGURE 2.9: Left: the 1 ps evolution of the site 1 population, described by the local thermalising Lindblad model and HEOM. Right: the Lindblad-HEOM trace distance over the course of the 1 ps evolution, for every Lindblad model (top) and just the local thermalising model (bottom). Top row: all models defined with a fixed parameter set. Bottom row: HEOM parameters kept the same as in the top row, but local thermalising Lindblad parameters changed to fit site 1 population to HEOM. $T = 300$ K, $\gamma = 20$ rad ps⁻¹, $\Gamma_{\text{deph}} = 11$ rad ps⁻¹.

It is quite apparent from the top left panel of Figure 2.9 that there is a large difference in behaviour of the site 1 population between the local thermalising model and HEOM for a fixed parameter set. The HEOM approach predicts higher frequency oscillations in the site populations, as well as more rapid dephasing to the equilibrium state. The frequency of oscillation predicted by the Lindblad model is determined solely by the system Hamiltonian, or more specifically the tunneling strength Δ , whereas for HEOM the spectral density parameters also contribute. Interaction of the system with the bath, as described by the spectral density, results in an effective increase of tunneling strength between sites, which manifests in the

HEOM approach as a faster frequency of oscillation of site population.

This behaviour was observed by Vaughan *et al.*,⁵³ who studied the non-Markovian effects in a dimer system similar to this one, and proposed that in order to properly probe these effects it is more appropriate to treat the coupling strength as a free parameter. The site population described by the Lindblad model can be fitted to HEOM model, and any differences between their evolution interpreted as being a direct result of non-Markovian behaviour. This is done by increasing the tunneling strength for the Lindblad model in order to match the frequencies of oscillation, and account for the higher effective coupling strength produced by the HEOM approach. Also, the reorganisation energy can be increased to match the rates of population dephasing due to coupling to the bath. The result is shown in the bottom left plot of Figure 2.9, with the changes in parameters summarised in the table shown in the bottom right plot. The effect of the fitting can be seen by the change in the trace-distance evolution for the local thermalising model, with the average trace distance, Q , decreasing in value upon fitting from 0.12 to 0.08.

For short times, $t < 200$ fs, the HEOM approach describes a smaller modulation of population amplitude, which can be attributed purely to non-Markovian effects as opposed to being an artefact of parameters. Also, at longer times ($t > 800$ fs), the decay of the trace distances of the thermalising models in the right hand plots of Figure 2.9 to non-zero values (despite the site 1 populations matching up) can be attributed to emergence of non-canonical equilibrium behaviour. While the Lindblad models equilibrate to the canonical thermal state, HEOM describes a steady state that deviates from this. This is again due to non-Markovian effects, and is discussed further in the next subsection. The average trace distance value of $Q = 0.08$ for the fitted parameter set more accurately represents the extent to which non-Markovian effects result in deviation of dynamics of the system as described by the Lindblad and HEOM approaches, both at short and long times.

2.1.5 Non-Canonical Steady States

If the reference state in Equation 2.6 is the canonical thermal state of the system ρ_{eq} , so that:

$$D(t) = \frac{1}{2} \text{tr}|\rho(t) - \rho_{\text{eq}}| , \quad (2.11)$$

then the equilibration of the system can be observed as decay of the trace distance over time. This can be performed for all Lindblad and HEOM approaches. The Lindblad approach, along with other perturbative quantum master equations formed under the Born-Markov approximations, has a steady state that corresponds to the canonical thermal state, characterised only by the system Hamiltonian H_{sys} and the bath temperature T as described in Section 1.4.5. However, if the bath response time is sufficiently slow relative to the timescale of the system's dynamics, such that the behaviour is non-Markovian, the existence of longer-lasting correlations may mean that the steady state reached by the system is not the canonical thermal state.⁴⁹ Instead, the system may exhibit *non-canonical* equilibrium behaviour. This non-canonical state:

$$\rho_{\text{ncanon}}^{\text{tot}} = \frac{e^{-\beta H_{\text{tot}}}}{\text{tr}(e^{-\beta H_{\text{tot}}})} \quad (2.12)$$

is characterised by considering the *total* Hamiltonian for the universe, $H_{\text{tot}} = H_{\text{sys}} + H_{\text{bath}} + H_{\text{int}}$, but the reduced density matrix for the system, ρ_{ncanon} , *cannot* be retrieved simply by tracing out the bath degrees of freedom:

$$\rho_{\text{ncanon}} \neq \text{tr}_B \left\{ \rho_{\text{ncanon}}^{\text{tot}} \right\}, \quad (2.13)$$

as non-Markovian behaviour results in the existence of system-bath correlations at equilibrium. Instead, use of a numerical, non-perturbative approach such as HEOM can identify the steady state as the state reached after long-time propagation of the reduced system density matrix, so that $\rho_{\text{ncanon}} = \lim_{t \rightarrow \infty} \rho(t)$.⁴⁰ Alternatively, an effective Hamiltonian H_{eff} that includes a reduced description of the bath can be defined. The non-canonical thermal state for the reduced system density matrix is then given by replacement of H_{sys} with H_{eff} in the equation for the canonical thermal state (Equation 1.27). While the numerical form of the non-canonical thermal state will not be discussed here, non-canonical equilibrium behaviour of a system will be signalled simply by equilibration of the system to any state *other than* the canonical one, as monitored by the trace distance.

Iles-Smith *et al.*,^{18,64} as part of their work using a *Reaction Coordinate Master Equation* approach that utilises an effective Hamiltonian, discuss emergence of non-canonical equilibrium behaviour of the system's steady state when described by non-perturbative approaches such as HEOM within certain system-bath coupling regimes and at certain temperatures.

Figure 2.10 shows the temperature dependence of non-canonical equilibrium behaviour exhibited by the model 2-site system. Modelled at cryogenic temperature (77 K), physiological temperature (300 K), and high temperature (600 K), the trace distances plotted monitor the similarity of the state to the canonical thermal state over time. For the Lindblad model

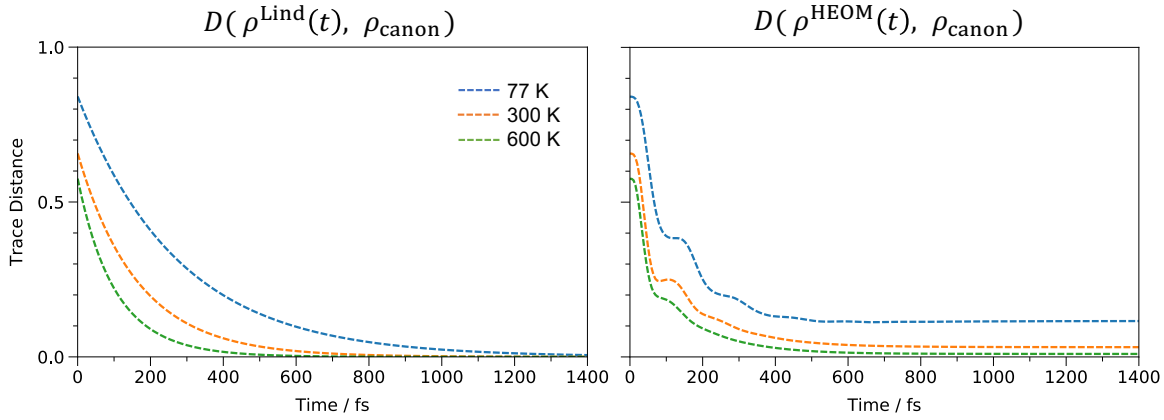


FIGURE 2.10: The temperature dependence of the trace distance with respect to the canonical thermal state for the local thermalising Lindblad (left) and HEOM (right). The Lindblad model equilibrates to the canonical state at all temperatures, whereas the HEOM model equilibrates to a non-canonical steady state that coincides with the canonical state only at higher temperatures.

(left plot), with the local thermalising model used as an example, the trace distances decay smoothly to zero at all temperatures, representing the equilibration of the system to the canonical thermal state.⁷

However, a different behaviour can be seen using the non-perturbative HEOM approach (right). At high temperature the steady state of the system closely matches the canonical thermal state, but at cryogenic temperature there is significant deviation, with the trace distance decaying to a value of ~ 0.12 . There exists an inverse temperature relationship; as the temperature decreases, the deviation of the steady state from the canonical thermal state increases. It can also be seen from Figure 2.10 that at physiological temperature, for this particular parameter set, there is significant deviation of the steady state from the canonical thermal state, indicated by a steady state trace distance of 0.05. Dependent on the parameter set used, such as the coupling regime, the emergence of non-canonical equilibrium behaviour at physiological temperature further highlights potential for the Lindblad method to be inaccurate in describing the bath relaxation dynamics of EET in the FMO complex.

2.1.6 Summary

While the local dephasing model equilibrates to the incorrect state, and the global model neglects inter-site distances and couplings, the local thermalising model exhibits neither of these behaviours so is likely to be the best candidate to describe EET dynamics in the FMO complex. However, the Lindblad models in general are susceptible to inaccuracies when there is existence of non-Markovian behaviour. This can result in the Lindblad approach over-estimating the frequency of oscillation of site populations, as well as not predicting the emergence of non-canonical equilibrium behaviour, the latter of which may occur at physiological temperature. However, these effects are highly sensitive to parameters.

2.2 The FMO Complex

In this section, the Lindblad models will be compared against the HEOM approach for their effectiveness in describing equilibration timescales and coherence transfer of site populations in the FMO complex at different temperatures, and in different regimes of non-Markovianity. Results predominantly from the local thermalising Lindblad model will be compared against results obtained by Zhu *et al.*⁵ using a modified scaled-HEOM approach (developed by Shi *et al.*⁶⁵) to simulate the EET dynamics in the FMO complex.

2.2.1 Parameters

Due to the orientation of BChl sites 1 and 6 towards the baseplate protein of the chlorosome initially excited by sunlight,¹ it is commonplace to observe EET dynamics in FMO starting from initial states that are excited on site 1, site 6, or a superposition of both.^{5,23} As pure states, these can be expressed as wavefunctions whose respective forms are $|\psi^{(1)}(0)\rangle = |1\rangle$, $|\psi^{(6)}(0)\rangle = |6\rangle$, and $|\psi^{(1,6)}(0)\rangle = \frac{1}{\sqrt{2}}(|1\rangle + |6\rangle)$. When the density matrix for the initial superposition state is formed (from the outer product of the wavefunction $|\psi^{(1,6)}(0)\rangle$), coherences in the site basis will be present.

In order to maintain consistency with other theoretical studies,^{3–5} the FMO system Hamiltonian in Table 1.1 and a Debye spectral density as in Equation 1.23 will be used. A value of $\lambda = 35 \text{ cm}^{-1}$ ($= 6.593 \text{ rad ps}^{-1}$) will be used for the reorganisation energy, with a value of $\gamma^{-1} = 50 \text{ fs rad}^{-1}$ ($= 20 \text{ rad ps}^{-1}$) for the bath relaxation rate. These parameters ensure agreement between numerical fitting and experimental data in Read *et al.*'s study into visualisation of

excitonic structure of FMO.^{4,66} Other bath relaxation rates, $\gamma^{-1} = 100 \text{ fs rad}^{-1}$ ($= 10 \text{ rad ps}^{-1}$), and 166 fs rad^{-1} ($= 6.024 \text{ rad ps}^{-1}$), will be used later for simulating different regimes of non-Markovianity, in accordance with work by Zhu *et al.*. While a dephasing rate need not be defined for the HEOM approaches, a value of $\Gamma_{\text{deph}} = 11.0 \text{ rad ps}^{-1}$ has been used as a parameter for the Lindblad models. This dephasing rate is equivalent to the rate constant in the local dephasing Lindblad model, as well as being used to define the rate of population transfer between degenerate eigenstates in the Redfield theory expression in Equation 1.25, i.e. $k(\omega = 0) = \Gamma_{\text{deph}}$. The value of $\Gamma_{\text{deph}} = 11.0 \text{ rad ps}^{-1}$ has been experimentally calculated for the bacterial light harvesting system 2 (LH2)^{67,68} and gave reasonable behaviour when used in the FMO simulations. This is used instead of an analytical expression for the dephasing rate:^{3,32,69}

$$\Gamma_{\text{deph}} = \lim_{\omega \rightarrow 0^+} k(\omega) = \frac{4\lambda k_B T}{\hbar\gamma}, \quad (2.14)$$

derived by taking the limit of the Redfield theory expression at zero frequency. Although this can be evaluated with spectral density parameters (i.e. $\Gamma_{\text{deph}} = 51.8 \text{ rad ps}^{-1}$ for $\lambda = 35 \text{ cm}^{-1}$, $\gamma = 50 \text{ fs rad}^{-1}$, $T = 300 \text{ K}$), there are uncertainties surrounding its validity. Exciton delocalisation may suppress the dephasing rate, and non-Markovian effects may also alter it,¹⁵ so instead the experimental value is used.

2.2.2 Qualitative Model Comparison

Figure 2.11 compares the long-time (2.5 ps) evolution of the FMO site populations for the three initial states at physiological temperature (300 K), described by HEOM (from Zhu *et al.*⁵) and each Lindblad model.

The global thermalising model equilibrates to the canonical thermal state far too quickly, as a direct result of its negligence for inter-site distances and couplings by considering only the energy difference between excitons (the system Hamiltonian's eigenstates). This can also be seen in Figure 2.12a which, through monitoring the inverse participation ratios of each state over time, shows the short-time rapid delocalisation of the exciton energy across more than 2 sites. This is compared to the local models, which remain more localised. Such fast equilibration means that no *quantum beating* is observed. Quantum beating, a signature of quantum coherence transfer, is defined as the periodic modulation of site populations and peak amplitudes³⁴ (as can be seen occurring between sites 1 and 2 up to 800 fs in the HEOM column of Figure 2.11a), and is discussed in more detail later. The local dephasing model,

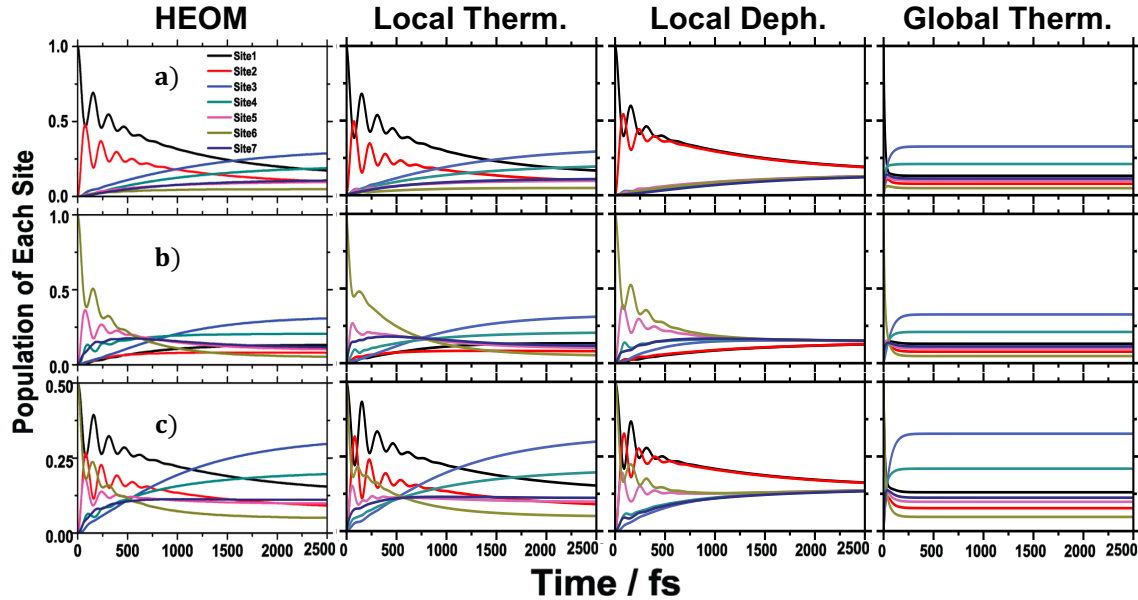


FIGURE 2.11: A comparison of the HEOM (left-most column, reproduced from Figure 7 of Zhu *et al.*⁵) and Lindblad dynamics of the FMO complex at $T = 300$ K. Each row corresponds to a different initial site excitation; a) site 1; b) site 6; c) a superposition of sites 1 and 6. $\gamma = 166$ fs rad $^{-1}$, $\lambda = 35$ cm $^{-1}$, $\Gamma_{\text{deph}} = 11.0$ rad ps $^{-1}$.

on the other hand, equilibrates on a more appropriate timescale. With the experimental dephasing rate of $\Gamma_{\text{deph}} = 11.0$ rad ps $^{-1}$ used, the site populations dephase on a comparable timescale to the HEOM approach so that quantum beating can be observed. Despite this, the incorrect equilibrium behaviour is exhibited. Modelled in the infinite temperature limit, all site populations are equally populated (with a probability of 1/7) in the system's steady state. This model therefore fails to capture the dominant population of sites 3 and 4 at equilibrium as is required for effective transfer of excitonic energy to the reaction centre. The relative site populations in the canonical thermal state at physiological temperature are shown in Figure 2.12b.

It is clear that the local dephasing and global thermalising models have complementary strengths and weaknesses; where the global model equilibrates to the canonical thermal state but does so over timescales that do not properly account for quantum coherence effects, the dephasing model describes such effects on short timescales, but equilibrates to the incorrect steady state. At first glance, the local thermalising Lindblad model seems to capture the strengths of both the dephasing and global model, agreeing qualitatively well with the HEOM approach. It equilibrates on an appropriate timescale and to the canonical state, with a dephasing rate that does not destroy quantum beating too quickly.

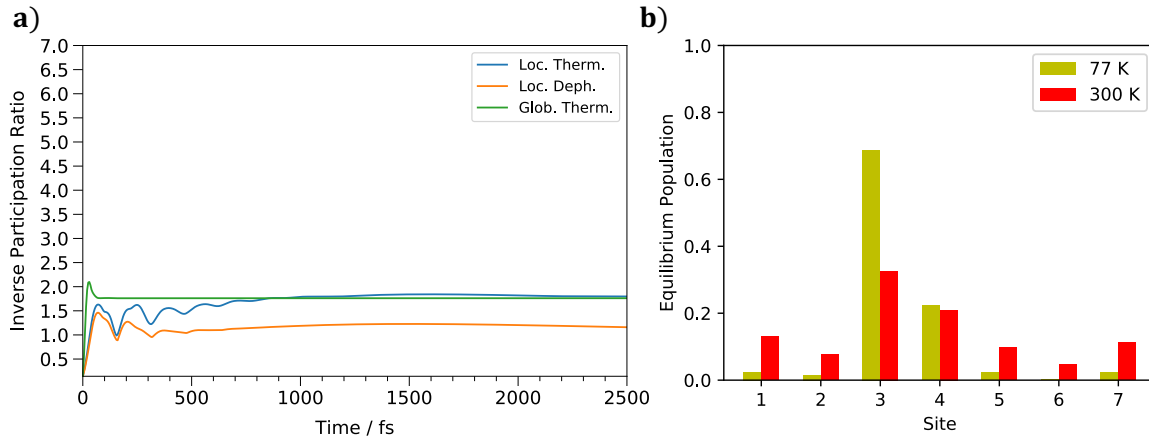


FIGURE 2.12: a) the 2.5 ps evolution of the inverse participation ratios states of the FMO complex described by each of the Lindblad models. Excitons remain relatively localised throughout; b) the site populations of the canonical thermal state of the FMO complex at cryogenic and physiological temperature. While sites 3 and 4 are still dominant at 300 K, it is clear that there is a tendency towards the maximally mixed state upon increasing temperature.

2.2.3 Equilibration Timescales

The FMO system Hamiltonian under the specified parameter set has been shown by Zhu *et al.*⁵ to equilibrate to the canonical thermal state (whose populations at cryogenic and physiological temperature are given in the right hand plot of Figure 2.12) when described by the HEOM approach. This means that despite the potential failure of the Lindblad in capturing non-canonical equilibrium behaviour (as outlined in Section 2.1.5), this will not be an issue in this case.

There are different ways of calculating the equilibration times. An exponential curve, with general equation $D^{(\text{fit})}(t) = ae^{-bt} + c$, where a , b , and c are fitting parameters, can be fitted to the equilibration-trace distance curve (i.e. $D(t) = \frac{1}{2}|\rho(t) - \rho_{\text{canon}}|$ as in Figure 2.10), and the timescale of equilibration, τ_{eq} , taken as the time at which this equation equals zero, i.e. $D^{(\text{fit})}(\tau_{\text{eq}}) = 0$. However, this is very sensitive to fitting parameters and relies on the value of c being negative to be valid. A tolerance, D_{tol} , could be introduced so that the equilibration time is taken as being the time at which $D^{(\text{fit})}(\tau_{\text{eq}}) < D_{\text{tol}}$, but due to the imperfect nature of the fitted curve this tolerance has to be around $D_{\text{tol}} \sim 0.05$, which is too high for valid timescales to be extracted. Alternatively, the actual equilibration-trace distance curve for the system, plotted as a function of time, can be monitored and the equilibration time taken as time at which it has decayed to a value of $D(\tau_{\text{eq}}) < 0.01$. This represents the time at which the distinguishability between the current state and the equilibrium state is lower than 1%.

This is the method that is used for the Lindblad models, and works because the equilibrium-trace distance curve is monotonically decreasing at all points, as a result of the Markovian nature of the Lindblad equation, as shown in Section 2.1.5. However, this method may not be valid for the HEOM approach, where non-Markovian effects may result in the curve having monotonically positive regions. For instance, the distance of the state from equilibrium could temporarily fall within the 1% tolerance before rising again.

Use of a consistent method for the Lindblad models allows a valid comparison between each of their equilibration timescales, with differences arising as a direct result of the way in which their specific Lindblad operators are defined. The method used by Zhu *et al.* to calculate their equilibration times and what tolerance they use (if any), however, is not clear. Therefore, emphasis should not be placed on the absolute values of their timescales compared to those quoted for the Lindblad models, but instead on the general trends and relative values.

The equilibration timescales for each of the Lindblad models at cryogenic (77 K) and physiological (300 K) temperatures, with dependence on different bath relaxation rates for the latter, is shown in Table 2.1, with timescales reported by Zhu *et al.* for their HEOM approach included where reported. Firstly, for a fixed temperature (300 K), increasing the bath relaxation timescale γ^{-1} increases the time it takes the thermalising models to reach equilibrium. Increasing the temperature at a fixed bath relaxation rate decreases the equilibration time. This is because a higher bath temperature reduces the persistence of quantum beating, allowing exciton transfers to occur more quickly.⁵

Secondly, the equilibration timescale of the local dephasing model is insensitive to changes in bath relaxation time and temperature, depending only on the dephasing rate Γ_{deph} . This again calls into question the case for using a rate that can be analytically expressed as a function of temperature and spectral density parameters, such as the form linearly dependent on temperature $\Gamma_{\text{deph}}(T) = 2\pi k_B T \lambda / \hbar^2 \gamma$ suggested by Panitchayangkoon *et al.*,³⁴ but again this is only predicted and may not hold in the aforementioned circumstances in Section 2.2.1.

Thirdly, due to the energy landscapes of each of the dominant pathways, $1 \rightarrow 2 \rightarrow 3$ and $6 \rightarrow (5, 7) \rightarrow 4 \rightarrow 3$, the energetically ‘downhill’ nature of the latter (with reference to Figure 1.3) means that the equilibration timescale of a state initially excited on site 6 should be faster than starting on site 1, with the superposition state taking a value that falls between the two. While this is observed for the local models and HEOM, it is not for the global

T (K)	γ^{-1} (fs rad $^{-1}$)	Model	Equilibration Time, τ_{eq} (ps)		
			Site 1	Site 6	Sites 1 & 6
77	50	HEOM	7	2	6
		Local Therm.	8.87	5.37	8.07
		Local Deph.	5.28	4.02	4.21
		Global Therm.	0.30	0.31	0.30
300	50	Local Therm.	2.48	1.19	2.18
		Local Deph.	5.28	4.02	4.21
		Global Therm.	0.08	0.10	0.09
300	100	Local Therm.	3.05	2.02	2.75
		Local Deph.	5.28	4.02	4.21
		Global Therm.	0.12	0.15	0.13
300	166	Local Therm.	4.29	3.22	3.95
		Local Deph.	5.28	4.02	4.21
		Global Therm.	0.18	0.23	0.20

TABLE 2.1: Equilibration times of each initial state for each Lindblad models at cryogenic and physiological temperatures. Equilibration times for different bath relaxation rates given at physiological temperature. HEOM data reported by Zhu *et al.*⁵ included where applicable.

model at any of the temperatures nor bath relaxation rates. Due to its negligence of inter-site couplings and distances, the global model has no in-built concept of the above dominant EET pathways that are encoded into the system Hamiltonian; instead the rates reflect the energy gap between excitons, regardless of where they are spatially localised. For the FMO complex that occupies the intermediate coupling regime, this also results in the global model having very fast equilibration times.

While the specific numbers cannot be commented on, the fact that the local thermalising model over-predicts the equilibration time compared to all the reported HEOM results is expected, aligning with the results met earlier in Section 2.1.4 whereby, for a fixed Hamiltonian and spectral density parameter set, the HEOM system Hamiltonian had a higher effective tunneling strength due to interaction with the bath. While this results in faster HEOM population transfer and therefore a shorter equilibration time compared to the Lindblad for all initial states, HEOM equilibration for initial excitation on site 6 in particular is significantly faster. The energetically downhill EET pathway for this initial state is enhanced by a higher effective tunneling strength than the dominant pathway starting from site 1 that features an ‘uphill’ transfer from 1 → 2 (see Figure 1.3).

2.2.4 Quantum Beating and EET Pathways

As a coherent theory, along with HEOM (see Section 1.3.5), the local thermalising Lindblad is able to capture coherence energy transfers, which manifests as quantum beating (modulation of amplitudes) between site populations. It, like the HEOM approach, is therefore able to describe the coherent ‘wave-like’ EET in the FMO complex observed experimentally by Engel *et al.*²⁴ Figure 2.13 shows the evolution of the FMO site populations at cryogenic temperature (77 K), for the three different initial states introduced previously. It shows the closed system, as well as the influence of the bath, as described by both the scaled-HEOM approach from Zhu *et al.* (left) and the local thermalising Lindblad (right). When treated as a closed quantum system, the unitary dynamics of the FMO complex governed by the system Hamiltonian is equivalent for both the HEOM and Lindblad models (outer columns). When treated as an open quantum system (middle columns), where the effect of the bath is considered, both approaches exhibit quantum beatings of site populations. This is observed to persist for some 650-800 fs for all three of the initial states, consistent with the experimental observation of 660 fs observed by Engel *et al.*²⁴ at this temperature. A more detailed discussion of these coherence effects for each initial state, considering the EET pathways involved, is given below.

Site 1 initial excitation. Being very strongly coupled ($V_{12} = -87.7 \text{ cm}^{-1}$, the strongest inter-site coupling in FMO), quantum beating between sites 1 and 2 persists for at least 800 fs in both the HEOM and Lindblad approaches. There is greater overlap of site populations at ~ 40 fs in the HEOM approach due to higher effective electronic (i.e. inter-site) coupling due to interaction with the spectral density (see Section 2.1.4). The high energy of site 2 relative to site 1 results in a long lifetime of the site 1 population and thus a slow build-up of population in site 3. In addition to this, the very large difference between energies of sites 2 and 3 ($|\Delta E_{23}| = 320 \text{ cm}^{-1}$) means that any population transfer to site 2 from site 1 results in almost irreversible transfer to site 3 with the back transfer $3 \rightarrow 2$ being suppressed. Consequently, there is no build up of population on site 2, but there is on site 3. All other sites (4-7), for both models, don’t experience much change in population, reflecting the spatial proximity and strength of excitonic coupling between sites involved in the $1 \rightarrow 2 \rightarrow 3$ EET pathway.⁷⁰ The reason there is no population beating between sites 1 and 6, despite being spatially close, is that the energy gap between them is greater than between sites 1 and 2 ($|\Delta E_{16}| = 220$, whereas $|\Delta E_{12}| = 120 \text{ cm}^{-1}$), and the coupling smaller ($V_{16} = -13.7 \text{ cm}^{-1}$).

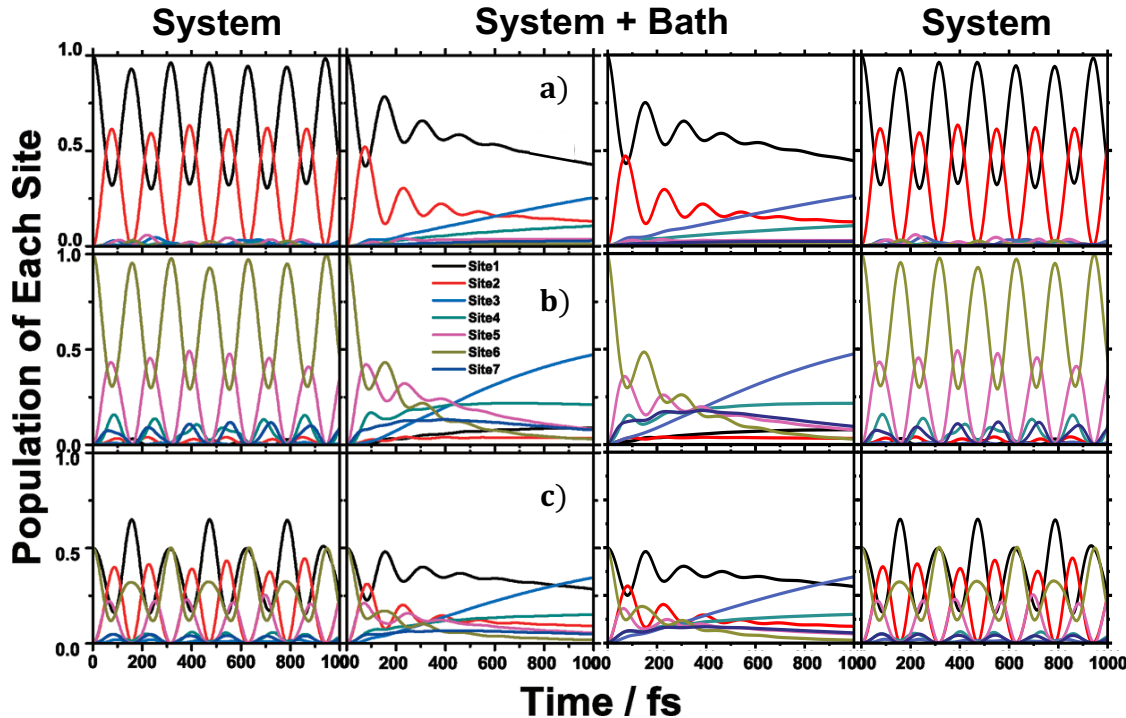


FIGURE 2.13: The 1 ps evolution of the FMO complex site populations for different initial states at cryogenic temperature (77 K). The outer columns show the unitary dynamics of the system alone, whereas the middle columns show the effect of the bath. The left two columns are plotted with HEOM, taken from Figure 3 of Zhu *et al.*,⁵ while the right two columns are plotted with the local thermalising Lindblad. Rows correspond to different initial excitations; a) site 1; b) site 6; c) a superposition of 1 and 6. $\gamma = 50 \text{ fs rad}^{-1}$, $\lambda = 35 \text{ cm}^{-1}$, and $\Gamma_{\text{deph}} = 11.0 \text{ rad ps}^{-1}$

Site 6 initial excitation. Quantum beating of populations between the strongly coupled sites 5 and 6 ($V_{56} = 81.1 \text{ cm}^{-1}$) can be observed, indicating quantum coherence that lasts for at least 650 fs in both models, again in agreement with experiment. However, the beatings described by the HEOM approach results in a greater overlap of site populations. Again, this is due to the greater effective electronic coupling between sites. There is also seen to be a small amount of quantum beating between the strongly coupled and similar energy sites 3 and 4 ($V_{34} = -53.5 \text{ cm}^{-1}$, $|\Delta E_{34}| = 110 \text{ cm}^{-1}$). For both models the population of site 6 decays much faster than it does for site 1 when it is initially excited; after 1 ps the population of site 6 is close to zero (Figure 2.13b), but after the same time the population of site 1 is ~ 0.5 (Figure 2.13a). This reflects the energy landscape of the different EET pathways. Where EET for initial excitation on site 1 occurs *via* the higher energy site 2, for initial excitation on site 6 EET can occur more rapidly *via* the lower energy sites 5 and 7. Fast transfer to lower energy BChl sites also prevents back-transfer of excitation energy to the baseplate protein.

Sites 1 and 6 initial excitation. The major differences in description between the Lindblad and HEOM approaches for each of prior initial states is diminished upon consideration of the initial state as a superposition. This is promising; with both sites 1 and 6 being ‘connected’ to the baseplate protein, the superposition state is likely to be a better descriptor of the instantaneous excitation event in the FMO complex. There is very good agreement between the local thermalising Lindblad model and HEOM for this initial state. Indeed the behaviour observed before is still present here. Beatings between sites 1 and 2 has stronger modulation in amplitude compared to the beatings between sites 6 and 5 due to the stronger coupling between them. The population of site 1 remains higher than that of site 6 due to energetically ‘uphill’ nature of the $1 \rightarrow 2$ population transfer compared to the ‘downhill’ pathway starting on site 6. The persistence of quantum beating indicates coherence effects that last for ~ 650 fs, again in agreement with experiment.

2.2.5 Entering Non-Markovian Regimes

When using a Debye spectral density, the inverse bath relaxation rate models the bath correlation time, $\gamma^{-1} = \tau_c$, so that decreasing γ increases the non-Markovianity.^{48,53} The effectiveness of the local thermalising Lindblad model when the system enters a strongly non-Markovian regime can be evaluated by direct comparison with HEOM at different relaxation times. Zhu *et al.* observed the evolution of a system described by HEOM initially excited in a superposition of sites 1 and 6 at physiological temperature for three bath relaxation timescales; $\gamma^{-1} = 50, 100,$ and 166 fs rad $^{-1}$. The results are shown in the left-hand column of Figure 2.14, with the results from the local thermalising Lindblad model given on the right.

For both models, as the bath relaxation time increases, the equilibration time increases, with the local thermalising Lindblad equilibrating marginally faster than the HEOM approach; this can most easily been seen by noting the time at which the populations of sites 1 and 3 cross over. For timescales $\gamma^{-1} = 50$ and 100 fs rad $^{-1}$, the local thermalising model seems to predict faster equilibration times compared to HEOM, but in the strongest non-Markovian regime the equilibration timescales seem to be well matched, though these cannot be quantitatively verified.

As reported by Zhu *et al.*, the *frequency* of site population oscillations is independent of bath relaxation timescale for the HEOM approach, and this can be seen to be the case with the local thermalising Lindblad as well. This is consistent with the finding by Vaughan *et al.*⁵³

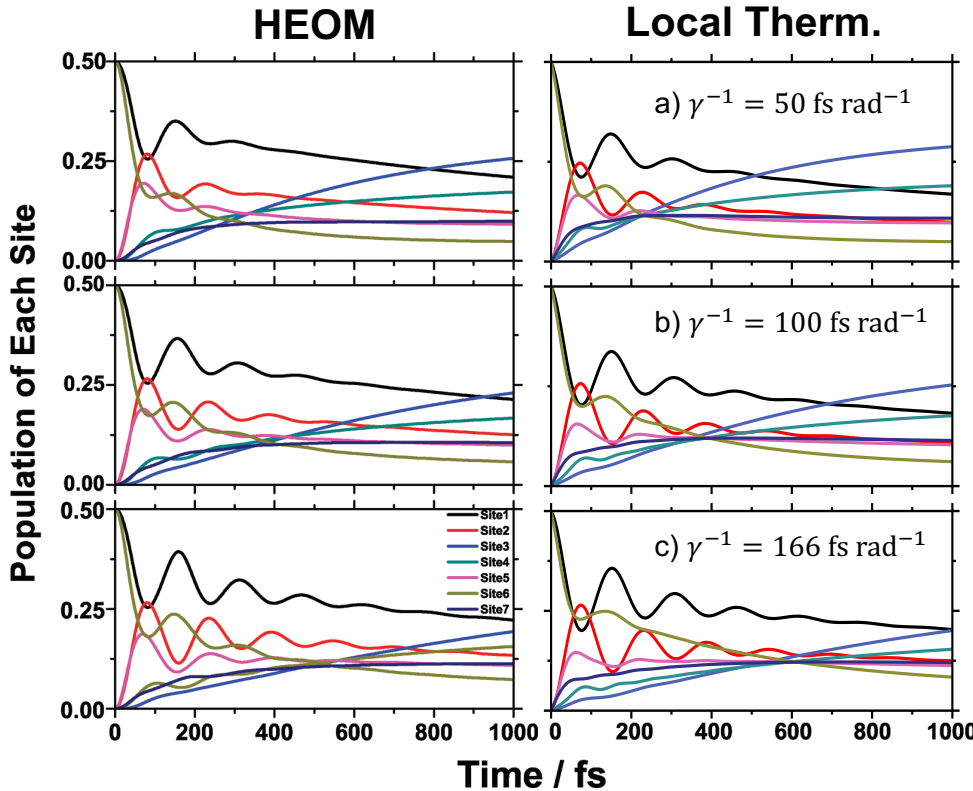


FIGURE 2.14: The 1 ps evolution of the FMO complex site populations at physiological temperature (300 K) for different bath relaxation timescales, γ^{-1} , with an initial excitation on a superposition of sites 1 and 6. Reproduced from Figure 6 of Zhu *et al.*⁵

as shown in Section 2.1.4, where the frequencies of oscillation in site populations between the Lindblad and HEOM approaches (with reference to Figure 2.9) is matched only by adjustment of the electronic coupling strength, with no dependence on the bath relaxation rate.

However, from Figure 2.14, the *strength* of population modulations is clearly dependent on bath relaxation timescale. Entering stronger non-Markovian regimes (by increasing the bath relaxation timescale) results in long-lasting quantum beatings, particularly between the strongly coupled sites 1 and 2,⁵ the first two sites in the dominant $1 \rightarrow 2 \rightarrow 3$ EET pathway mentioned earlier. Both the local thermalising model and HEOM approach show this trend for these sites, exhibiting longer lasting coherences in stronger non-Markovian regimes. However, despite seeming to under-predict equilibration times in the case of $\gamma^{-1} = 50$ and 100 fs rad^{-1} , the persistence of population beatings between sites 1 and 2 is over-predicted.

For sites 6 and 5, the local thermalising model captures the qualitative trend shown between rows in Figure 2.14. As γ^{-1} is increased, the extent to which populations for sites 6 and 5 cross over decreases. The local thermalising model, however, is unable to capture the persistence

of beating between these sites as γ^{-1} is increased, with very fast dephasing in the case of $\gamma^{-1} = 166 \text{ fs rad}^{-1}$. This may be due to the energy landscapes. A lower bath relaxation rate, γ , gives a higher rate of population transfer, given by the Redfield rate expression in Equation 1.25. However, this is met with no resistance in the energy difference between sites 6 and 5 (a ‘downhill’ transfer) so results in rapid population transfer. This is in contrast to the large, ‘uphill’ $1 \rightarrow 2$ transfer, which allows the beatings to persist for longer. The non-Markovian effects captured by the auxiliary density matrices in the HEOM approach allow quantum beatings to persist for longer, and is less affected by the energy landscapes in the strongly non-Markovian regime. Despite the subtle differences, the local thermalising model performs very well in replicating the behaviour exhibited by the HEOM approach, despite not being able to account for non-Markovian effects.

2.2.6 Computational Expense

Using a scaled-HEOM approach, whereby the ADMs from the original HEOM method (outlined in Section 1.6.2) were scaled by:

$$\tilde{\rho}_{\mathbf{n}}(t) = \left(\prod_{k,j} n_{jk}! |c_k|^{n_{jk}} \right)^{-\frac{1}{2}} \rho_{\mathbf{n}}(t), \quad (2.15)$$

in accordance with a method developed by Shi *et al.*⁷¹ Zhu *et al.* were able to achieve numerical convergence at a truncation level of $\mathcal{N}_c = 2$ at 77 K and $\mathcal{N}_c = 4$ at 300 K, where truncation levels of $\mathcal{N}_c = 12$ could be required for the original HEOM approach. With this significant reduction in computational expense, a 2.5 ps simulation was reported to take around 7 minutes and 1.5 hours on a standard desktop computer for each respective temperature.⁵ This is in contrast to the Lindblad approach, which for the same system simulates a 2.5 ps evolution in under 1 second.

For a given number of timesteps, simulation time for the Lindblad approach is only dependent on the size of the system being simulated; a larger system will require working with larger density matrices ($(N \times N)$ for an N -site system) but in theory, due to the Born-Markov approximation and the nature of the fixed-propagator, only the current state of the system needs to be accessed to calculate the future state of the system.

On the other hand, HEOM requires access to and storage of all of the other ADMs at a given

timestep for propagation of the reduced system density matrix. For an N -site system at a hierarchy truncation level of \mathcal{N}_c , the number of matrices that need to be evaluated at each step grows factorially with truncation level as $(N + \mathcal{N}_c)!/(N! \mathcal{N}_c!)$.^{3,4} For the 7-site FMO complex with a truncation level of $\mathcal{N}_c = 4$, for example, 330 matrices need to be evaluated at each timestep, each of size $(N \times N)$.

HEOM also requires consideration of the truncation level \mathcal{N}_c and correlation function cutoff K needed to achieve numerical convergence, and due to their dependence on input parameters, must be determined on a case-by-case basis. With the Lindblad approach, none of these considerations need to be made.

Chapter 3

Conclusion

3.1 Summary

The Lindblad equation provides a computationally cheap, tractable, and easily implemented description for the dynamics of open quantum systems, with one such model accurately replicating EET dynamics in the FMO complex described by the HEOM approach.

For the model 2-site system, the Lindblad equation's inability to describe non-Markovian behaviour has been shown to be important for certain parameter sets. Larger deviations of the steady state away from the canonical thermal state as described by HEOM occur in stronger coupling regimes and at lower temperatures.¹⁸

Parametrised by only a dephasing rate, and with choice of an appropriate, experimentally determined value, the local dephasing model is able to describe the short-time quantum coherence transfers with reasonable agreement to HEOM in both the 2-site model and the 7-site FMO complex. However, equilibration to the maximally mixed state invalidates the long-time behaviour of the quantum state evolved by this model. The global thermalising model, while equilibrating to the canonical thermal state (shown by Zhu *et al.*⁵ to be the equilibrium state for the FMO complex defined under the parameters in Section 2.2.1), neglects inter-site distances and couplings in its consideration of population transfers. This results in very fast equilibration times in the FMO complex, with the model failing to predict any quantum coherence effects.

The local thermalising model, in contrast, recreated many of the coherence behaviours in the FMO complex predicted by the HEOM approach, both at cryogenic and physiological temperatures. Treating the coupling strength as a free parameter in Section 2.1.4 allowed the

site populations to be fitted, and showed that there were only small differences between the local thermalising model and HEOM approach due to non-Markovian effects. This, scaled up to the FMO complex, resulted in this Lindblad model describing the physiological dynamics very well in a strongly non-Markovian regime, in good agreement with HEOM (as shown in Section 2.2.5). In addition to this, a 2.5 ps simulation of the FMO complex at physiological could be performed in under one second, in contrast to the 1.5 hours taken to perform the same simulation with the HEOM approach.

As a numerically exact and non-perturbative treatment, the HEOM approach is able to provide an accurate description of EET dynamics in PPCs such as the FMO complex, while properly accounting for non-Markovian and non-canonical equilibrium effects. However, the ability of the Lindblad equation (or more specifically the local thermalising model) to recreate, with impressive speed, such behaviour in good agreement with HEOM is promising. It could be easily scaled to larger systems, such as light harvesting systems in purple bacteria (i.e the LH1 and LH2 complexes), and can be combined with considerations of other dynamical processes (see Section 3.2.1) to calculate the EET efficiencies.¹⁶ Moreover, the Lindblad approach could be used to quickly and accurately simulate EET dynamics as part of a process of screening potential synthetic light harvesting architectures designed *in silico*.

3.2 Future Work

This section describes some work that leads directly on from this study. Inclusion of dynamical processes other than just the bath relaxation dynamics can allow for trapping efficiencies to be calculated, while calculation of the exact form of the spectral density for the FMO complex will allow a more accurate description of the interaction between excitations in the system and the surrounding protein environment.

3.2.1 Trapping Efficiency

Consideration of the other dynamical processes occurring as part of EET in the FMO complex can allow the efficiency, $\varepsilon[\rho(t)]$, of the energy trapping process to be calculated. This can be defined as the proportion of excitations entering the system that are successfully trapped at the reaction centre. Evolving the state of the system with $\mathcal{L} = \mathcal{L}_{\text{sys}} + \mathcal{L}_{\text{bath}}$, using the three different Lindblad models to model $\mathcal{L}_{\text{bath}}$, the energy trapping process, $\mathcal{L}_{\text{trap}}$ (see Section

[1.3.3](#)), has an efficiency that at any given time can be calculated by:¹⁶

$$\varepsilon[\rho(t)] = \frac{\langle 0 | \mathcal{L}_{\text{trap}} \rho(t) | 0 \rangle}{\langle 0 | (\mathcal{L}_{\text{trap}} + \mathcal{L}_{\text{decay}} + \mathcal{L}_{\text{rad}}^{\text{emit}}) \rho(t) | 0 \rangle}, \quad (3.1)$$

where $|0\rangle$ represents the zero-exciton ground state and $\mathcal{L}_{\text{decay}}$ represents electron-electron hole recombination resulting in loss of heat to the environment. For simplicity, the efficiency is only calculated in the single-excitation manifold. In terms of radiative processes, this excludes absorption, but allows for emission (spontaneous or stimulated) events, $\mathcal{L}_{\text{rad}}^{\text{emit}}$, to be considered. Further to this, a time-averaged efficiency, $\langle \varepsilon[\rho(t)] \rangle_t$, for all states $\rho(t)$ in the evolution by $\mathcal{L} = \mathcal{L}_{\text{sys}} + \mathcal{L}_{\text{bath}}$ can be calculated. This could then be compared with experimental results to further assess the performance of the Lindblad approach.

3.2.2 The Spectral Density

Lack of detailed information about the specific spectral density for the FMO complex⁴ leads to the use of approximate forms in order to capture the system-bath interaction. The Debye spectral density (Equation [1.23](#)) is the form most commonly used in theoretical studies, both in QME approaches and HEOM, being a foundation for expressing the bath correlation function as an infinite sum of exponentials in the latter (see Section [1.6](#)). As an approximate and general form, it is highly versatile and applicable to many different problems in open system dynamics, and in some respects provides a common ground for comparison between studies. However, by virtue of the fact that it is approximate and makes the assumption that the spectral density equal for all sites,^{4,39} tailoring the spectral density to the specific system of interest will allow for a more accurate description of the system-bath interaction.

Parametrisation

In 2002, Renger and Marcus used a density matrix approach to calculate the correlation function of a monomer of the B777 PPC found in the photosynthetic purple bacteria *Rhodoblastus acidophilus* from a simulated fluorescence line narrowing spectrum. From this, a parametrised spectral density was derived:³⁷

$$J_{\text{Renger}}(\omega) = \sum_{i=1}^2 \frac{s_i}{7!2\omega_i^4} \omega^3 \exp\left(-\sqrt{\frac{\omega}{\omega_i}}\right), \quad (3.2)$$

with $s_1 = 0.8$, $s_2 = 0.5$, $w_1 = 0.069$ meV ($= 0.105$ rad ps $^{-1}$), and $w_1 = 0.24$ meV ($= 0.365$ rad ps $^{-1}$). This can be scaled by a factor, f :

$$f = \pi\lambda \frac{s_1\omega_2 + s_2\omega_1}{42\omega_1\omega_2} , \quad (3.3)$$

to ensure integration over all frequency space recovers the reorganisation energy:

$$\lambda = \frac{1}{\pi} \int_0^\infty f \frac{J_{\text{Renger}}(\omega)}{\omega} d\omega , \quad (3.4)$$

in accordance with the Debye spectral density as outlined in Equation 1.24. Another approximate form used is the Ohmic spectral density, given by:⁴⁷

$$J_{\text{Ohmic}}(\omega) = \pi\lambda \frac{\omega}{\gamma} \exp\left(-\frac{\omega}{\gamma}\right) , \quad (3.5)$$

that has again been scaled to ensure integration of the quotient $J(\omega)/\omega$ over all positive frequencies recovers the reorganisation energy. A comparison of the parameterised spectral density with the approximate Debye and Ohmic forms is given in Figure 3.1i. It can be seen that the Ohmic and Renger-Marcus forms describe stronger interactions of excitations in the system with lower frequency modes, with a faster decay of interaction as the frequency is increased. This means that for these spectral densities, compared to the Debye form, a greater degree of non-Markovianity is likely to be exhibited, due to an effective increase in bath correlation time (by decreasing γ).⁵³ The effect of this on the dynamics of the site 1 population of the FMO complex is shown in Figure 3.1ii. The different forms of the spectral density have a noticeable effect. The Renger-Marcus parameterised form results in stronger modulation of amplitudes, as well as slower decay of populations. The Ohmic and Renger-Marcus forms also exhibit longer-lasting coherence effects than the Debye form. The difference in equilibration times can also be seen by observing all the FMO complex site populations for different initial states in Figure 3.1iii.

While parameterised for a PPC in a different species of bacteria, the effect of using the Renger-Marcus (or indeed the Ohmic) spectral density is clear, with noticeable differences arising in the evolution of the site 1 population. A spectral density parametrised specifically for the FMO complex will likely have an effect on the dynamics too, justifying the motivation for use of a more accurate and tailored spectral density for the system of interest.

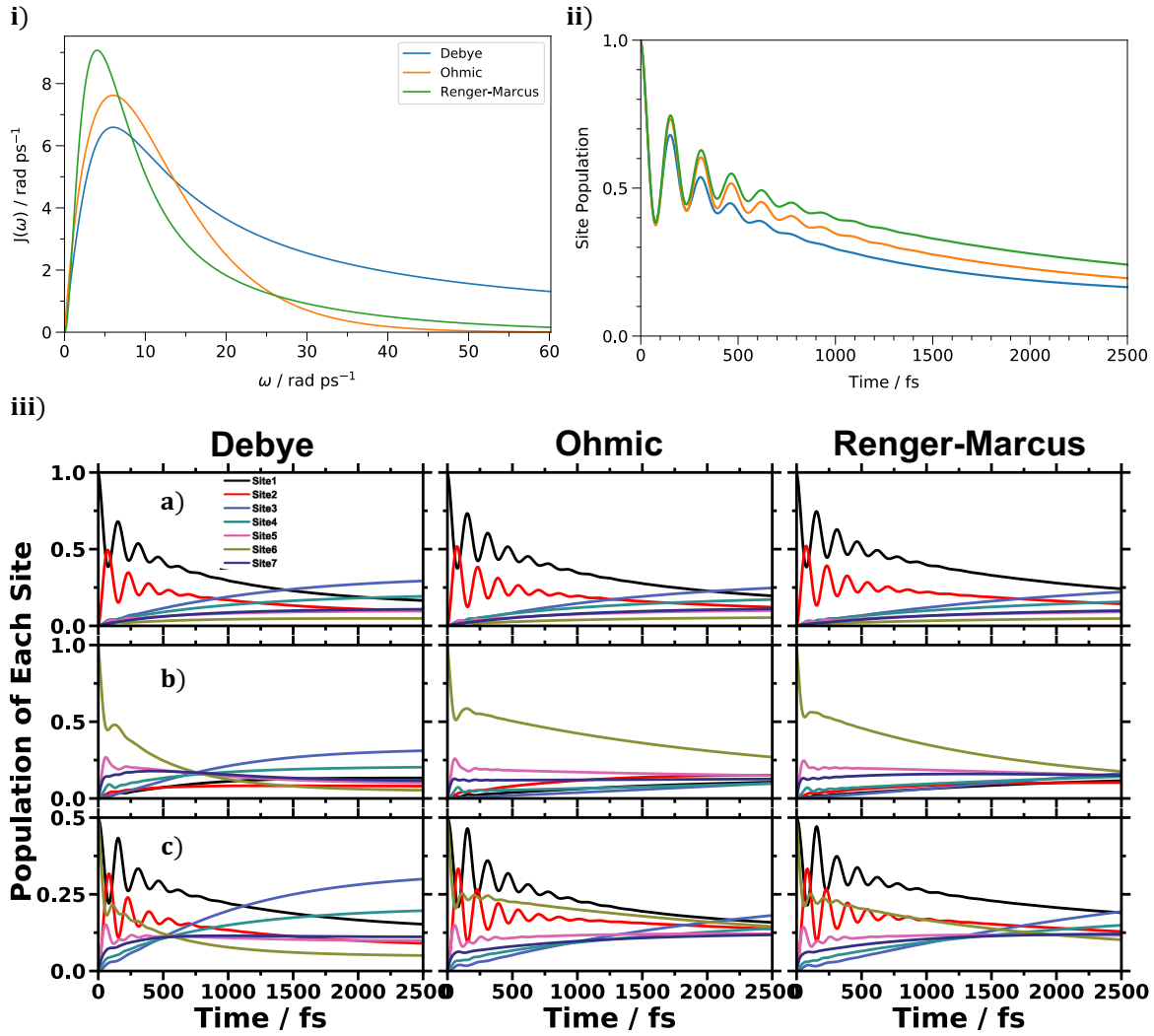


FIGURE 3.1: Top left: A comparison of the forms of the Debye (blue), Ohmic (orange), and Renger and Marcus' parameterised spectral densities (green). Top right: A comparison of the FMO complex site 1 population for each of the spectral densities, starting from initial excitation on site 1. Bottom: the 2.5 ps evolution of the FMO complex site populations with different spectral densities plotted in each column. Each row corresponds to a different initial excitation; a) site 1; b) site 6; c) a superposition of sites 1 and 6. Parameters used; $T = 300$ K, $\gamma^{-1} = 166$ fs rad $^{-1}$, $\lambda = 35$ cm $^{-1}$, and $\Gamma_{\text{deph}} = 11$ rad ps $^{-1}$.

Calculation

Even when using the parametrised Renger-Marcus form of the spectral density, the assumption that it is equivalent for all sites is still made. This is likely to be invalid due to the variation in local protein environments that each of the BChl sites occupies in the FMO complex, and therefore different interactions between BChl excitations and bath modes.

The X-ray crystal structure of the FMO complex, for example from *C. tepidum*, can be obtained from the Protein Data Bank⁷² (code: 3ENI). With this, electronic structure theory

methods can be used to calculate the exact spectral density of the FMO complex. Calculations can be easily run in *entos*,⁷³ a quantum simulation software package that specialises in *ab initio* molecular dynamics for condensed phase systems. Many methods could be used, but a computationally cheap method such as GFN0-xTB could be used to run single point energy calculations⁷⁴ and determine the excitation energies of the BChl molecules within the FMO complex. Another computationally cheap method, known as Δ SCF, performs single point calculations using the self-consistent field (SCF) method of convergence. Calculating the energies of the structures of the ground and first excited states, where the electron occupations are different, allows the excitation energy for each molecule to be approximated as the difference between them. These methods can be used with the molecular dynamics methodology below to calculate the spectral density for the FMO complex. Using cheap methods will allow the process to be tested first, and then a more rigorous *ab-initio* method such as time-dependent density functional theory (TD-DFT) could be used to calculate the excitation energies with a higher accuracy.²⁹

Molecular Dynamics Snapshots

1. Run classical MD using the crystal structure data of FMO complex.
2. Take snapshots of the trajectory at regular time intervals.
3. Perform electronic structure theory calculations on each snapshot to calculate the excitation energy. Doing so over a range of trajectory snapshots would allow the fluctuations in the energy as a result of different vibrational conformations of the system and bath to be captured.
4. Calculate the average energy over all of these snapshots, and calculate the deviation of the energy of each snapshot from this average, $(E(t) - E_{\text{av}})$.

Correlation Functions

1. Choose a lag time τ at which the correlations between energies will be calculated.
2. Calculate the correlation function of the energy fluctuations:⁷⁵

$$C_{\Delta E \Delta E}(t) = \langle (E(t) - E_{\text{av}})(E(t + \tau) - E_{\text{av}}) \rangle , \quad (3.6)$$

by averaging (indicated by the $\langle \dots \rangle$ brackets) over all pairs of snapshots that are separated by τ .

3. Repeat the process of calculating the correlation function using a range of lag times, τ . The constraint that $\tau_{\max} \ll t_{\text{tot}}$, where τ_{\max} is the maximum lag time used, and t_{tot} is the total MD simulation time, is applied. This is to ensure sufficient sampling of pairs of snapshots that are separated by τ_{\max} ; for example if $\tau_{\max} = t_{\text{tot}}$ then only one pair of snapshots would be sampled. It is therefore paramount that the total MD simulation time t_{tot} is sufficiently long. The value of τ_{\max} must also be long enough that convergence of the correlation function (as seen in Figure 1.4b) has been achieved.
4. Sum all of the correlation functions calculated for each τ value to obtain a total correlation function.
5. Fourier-Laplace transform the correlation into frequency space and derive the spectral density.

This should allow for a more accurate, site-dependent description of the system-bath coupling in the FMO complex. This process can be completed using the cheap electronic structure methods described above, as well as with small range of values of the lag time. If use of the resultant spectral contributes to a large change in dynamics for the FMO complex, the level of theory and range of lag times can be increased to improve the accuracy.

3.3 Closing Remarks

3.3.1 Are Coherence Effects Important?

A study into the FMO complex by Wilkins and Dattani³⁹ concluded that coherence effects aren't important for efficient EET in the FMO complex. Comparing the coherent HEOM approach against the incoherent, approximate, and perturbative Förster theory, they were able to show that despite its inability to capture short-time quantum beating of site populations, Förster theory performs well in describing the energy transfers over a longer time period, sometimes over-predicting the efficiency. In addition to this, Duan *et al.*⁴⁴ reported quantum decoherence in the FMO complex occurring within 60 fs, based on a combination of their experimental 2D photon echo spectra and theoretical work. Both of these studies challenge the

conclusions of many experimental and theoretical works that attribute long-lasting quantum coherence to the high EET efficiency observed in photosynthetic PPCs.^{11,34,43}

3.3.2 Light-Matter Interactions

Consideration of the excitation of a biologically relevant system such as the FMO complex as a ‘delta-event’, an infinitely-short instantaneous excitation⁴¹ from which the dynamics of EET are then observed, is an acceptable assumption to make in order to monitor solely the bath relaxation dynamics. This allows comparison of the Lindblad equation and HEOM approaches, such as those by Zhu *et al.*⁵ and Ishizaki and Fleming,⁴⁹ against results from single-photon absorption experiments.^{21,24,76}

However, these systems, in their natural environment, are photo-excited by continuous-wave, incoherent sunlight. In addition to this, the nature of the energy-time uncertainty principle⁷⁷ means that the ‘arrival times’ of such photons cannot be treated as an instantaneous event. These challenge the validity of using coherent laser pulses to study the dynamics of such systems,⁹ and indeed it has been shown that the characteristics of the incident radiation do have an effect on subsequent observed dynamics.⁷⁸ This adds further depth and complexity to the debate surrounding the importance of coherence effects on the efficiency of EET in photosynthetic PPCs. It may also have implications for the ability of the local thermalising Lindblad model to successfully recreate dynamics described by the HEOM approach, for example, in the case of the observed quantum beatings in the initial coherent superposition state, $\rho^{(1,6)}(0)$, described in Section 2.2.4.

It is therefore important to develop theories that are able to treat light-matter interactions explicitly. For example, new work by Janković and Mančal in 2020⁴¹ proposes a hybrid quantum master equation-HEOM approach that can explicitly account for, and perturbatively treat, the excitation event, while treating the coupling between excitations and the bath non-perturbatively. There may be potential for the Lindblad equation to form the QME part of this approach to treat the light-matter interaction. When paired with the HEOM approach, it could provide a powerful tool for modelling the EET dynamics in the FMO complex, and indeed in other photosynthetic PPCs, while accounting for excitation by natural sunlight. In conjunction with further experimental studies, the role quantum coherence effects play in the high efficiency of EET in photosynthetic PPCs (if any) can be understood to a deeper level, with studies into the structure of complexes¹⁶ extended to account for excitation by

incoherent light sources. This work can build off of current understanding of EET laid down by single-photon absorption experiments both experimentally and *in silico*. This will push the field ever closer towards development of synthetic devices able to mimic the behaviour of natural PPCs in natural sunlight.

Appendix A

Mathematical Concepts

A.1 Abbreviations and Notation

- The ' \implies ' symbol represents *implication*.
- The ' \forall ' symbol represents 'for all' (set notation).
- The ' \in ' symbol represents 'is a member of' (set notation).
- For clarity, operators may be expressed without a hat:

$$A \implies \hat{A}$$

this applies most readily to the Hamiltonian, H , and the density matrix, ρ .

A.2 Operators

Operators in quantum mechanics are represented by matrices and have, amongst others, the following properties.

A.2.1 Linearity

An operator \hat{A} that maps E onto F , (i.e. $\hat{A} : E \longrightarrow F$) is linear if it satisfies:

$$\hat{A}(\mathbf{x} + \mathbf{y}) = \hat{A}\mathbf{x} + \hat{A}\mathbf{y} \quad (\text{A.1})$$

$$\hat{A}(c\mathbf{x}) = c\hat{A}\mathbf{x} \quad (\text{A.2})$$

for vector spaces E and F where $x, y \in E$, and constant c .

A.2.2 Commutation

The commutator and anti-commutator (respectively) of two linear operators, \hat{A} and \hat{B} , are given by:

$$[\hat{A}, \hat{B}] = \hat{A}\hat{B} - \hat{B}\hat{A} \quad (\text{A.3})$$

$$\{\hat{A}, \hat{B}\} = \hat{A}\hat{B} + \hat{B}\hat{A} \quad (\text{A.4})$$

and operators are said to *commute* if the order in which they are applied leads to the same result, i.e. if $[\hat{A}, \hat{B}] = 0$.

A.2.3 Trace

The trace of an $N \times N$ square matrix/operator is defined as the sum of the diagonal elements, given by:

$$\text{tr}(\hat{A}) = \sum_i^N a_{ii} |i\rangle \langle i| \quad (\text{A.5})$$

where a_{ii} is the diagonal matrix element. The trace has the following important properties:

- Linearity:

$$\text{tr}(\hat{A} + \hat{B}) = \text{tr}(\hat{A}) + \text{tr}(\hat{B}) \quad (\text{A.6})$$

- Invariant to unitary transformation (where \hat{U} is a unitary operator):

$$\text{tr}(\hat{U}^\dagger \hat{A} \hat{U}) = \text{tr}(\hat{A}) \quad (\text{A.7})$$

as well as basis transformation.

- Invariant to cyclic permutation:

$$\text{tr}(\hat{A}\hat{B}\hat{C}) = \text{tr}(\hat{C}\hat{A}\hat{B}) = \text{tr}(\hat{B}\hat{C}\hat{A}) \quad (\text{A.8})$$

and thus a simpler relation useful for the next property is:

$$\text{tr}(\hat{A}\hat{B}) = \text{tr}(\hat{B}\hat{A}) \quad (\text{A.9})$$

- It therefore follows from equation (A.9), and using equation (A.6), that the trace of a commutator is zero:

$$\text{tr}([\hat{A}, \hat{B}]) = \text{tr}(\hat{A}\hat{B} - \hat{B}\hat{A}) = \text{tr}(\hat{A}\hat{B}) - \text{tr}(\hat{B}\hat{A}) = 0 , \quad (\text{A.10})$$

but not so for the anti-commutator:

$$\text{tr}(\{\hat{A}, \hat{B}\}) = \text{tr}(\hat{A}\hat{B} + \hat{B}\hat{A}) = 2 \text{ tr}(\hat{A}\hat{B}) . \quad (\text{A.11})$$

A.2.4 Kronecker Product

The Kronecker product of 2 matrices \hat{A} and \hat{B} is given by:

$$\hat{A} \otimes \hat{B} = \begin{bmatrix} a_{11}\hat{B} & a_{12}\hat{B} & \cdots & a_{1,n}\hat{B} \\ a_{21}\hat{B} & a_{22}\hat{B} & \cdots & a_{2,n}\hat{B} \\ \vdots & \vdots & \ddots & \vdots \\ a_{m1}\hat{B} & a_{m2}\hat{B} & \cdots & a_{m,n}\hat{B} \end{bmatrix} , \quad (\text{A.12})$$

for example:

$$A = \begin{bmatrix} 1 & 10 \\ 100 & 1000 \end{bmatrix}, \quad B = \begin{bmatrix} 1 & 2 \\ 3 & 4 \end{bmatrix},$$

$$A \otimes B = \begin{bmatrix} 1 & 2 & 10 & 20 \\ 3 & 4 & 30 & 40 \\ 100 & 200 & 1000 & 2000 \\ 300 & 400 & 3000 & 4000 \end{bmatrix}.$$

A.2.5 Superoperators

A superoperator is an operator acting on an operator.⁵²

A.3 Hermitian Operators

Most of the important operators in quantum mechanics are *Hermitian* or *self-adjoint*, and they describe useful observables such as:

- momentum (represented by the momentum operator \hat{p}_q),
- position (represented by the position operator \hat{q}),
- spin (represented by the spin operator \hat{S}).

They satisfy the definition of hermiticity that:

$$A = A^\dagger \quad (\text{A.13})$$

where the dagger \dagger denotes the complex-conjugate transpose of A . The Hamiltonian and the density matrix are also usually Hermitian.

A.4 Delta Functions

A.4.1 Dirac

A Dirac delta function, $\delta(x - a)$, defines a unit pulse at $x = a$, and evaluates to zero for all points on a continuous spectrum of the variable x where $x \neq a$. It has the property that the integral of the function over all space is one.

$$\int_{-\infty}^{\infty} \delta(x - a) = 1 \quad (\text{A.14})$$

A.4.2 Kronecker

The Kronecker delta function, δ_{ab} , is the discrete variable analogue of the Dirac delta function, evaluating to zero when $a \neq b$ and 1 when $a = b$. If a and b are orthonormal quantum states, for example, their inner product evaluates to the Kronecker delta function, i.e. $\langle a | b \rangle = \delta_{ab}$.

Appendix B

Background Quantum Theory

B.1 Energy of the System

Suppose the state of a system consisting of the linear combination of 2 orthonormal sites $|\phi\rangle = \frac{1}{\sqrt{2}}(|1\rangle + |2\rangle)$ is described by the Hermitian *spin-boson* system Hamiltonian:

$$H_{\text{sys}} = \frac{\epsilon}{2}\sigma_z + \frac{\Delta}{2}\sigma_x , \quad (\text{B.1})$$

where the Pauli operators are $\sigma_z = |1\rangle\langle 1| - |2\rangle\langle 2|$ and $\sigma_x = |1\rangle\langle 2| + |2\rangle\langle 1|$. ϵ defines the difference in energies of each site, while Δ defines the tunnelling strength between them. The total energy of the system can be recovered by taking the *expectation value* of H_{sys} with regard to the state of the system $|\phi\rangle$:

$$\begin{aligned} E_{\text{tot}} &= \langle\phi| H_{\text{sys}} |\phi\rangle , \\ &= \frac{1}{\sqrt{2}}(\langle 1| + \langle 2|) \left(\frac{\epsilon}{2}\sigma_z + \frac{\Delta}{2}\sigma_x \right) \frac{1}{\sqrt{2}}(|1\rangle + |2\rangle) , \\ &= \frac{\epsilon}{4}(\langle 1| + \langle 2|)\sigma_z(|1\rangle + |2\rangle) + \frac{\Delta}{4}(\langle 1| + \langle 2|)\sigma_x(|1\rangle + |2\rangle) , \\ &= \frac{\epsilon}{4}(\langle 1| + \langle 2|)(|1\rangle\langle 1| - |2\rangle\langle 2|)(|1\rangle + |2\rangle) + \frac{\Delta}{4}(\langle 1| + \langle 2|)(|1\rangle\langle 2| + |2\rangle\langle 1|)(|1\rangle + |2\rangle) , \end{aligned}$$

simplifying the inner products that evaluate to zero due to the orthonormality of the basis states:

$$\langle n|m \rangle = \delta_{nm} \quad (\text{B.2})$$

where δ_{nm} is the Kronecker delta (see Appendix A.4), it follows that:

$$\begin{aligned} E_{\text{tot}} &= \frac{\epsilon}{4} (\langle 1|1\rangle \langle 1|1\rangle - \langle 2|2\rangle \langle 2|2\rangle) \\ &= \frac{\epsilon}{4} (1 - 1) \\ E_{\text{tot}} &= 0 . \end{aligned}$$

Following similar steps, the energies of each site can be retrieved by finding the expectation values of H_{sys} with respect to each of the sites:

$$\epsilon_1 = \langle 1|H_{\text{sys}}|1\rangle = +\frac{\epsilon}{2} , \quad (\text{B.3})$$

$$\epsilon_2 = \langle 2|H_{\text{sys}}|2\rangle = -\frac{\epsilon}{2} . \quad (\text{B.4})$$

The site energies are therefore equally distributed around zero.

B.2 The Density Matrix

The density matrix (or density *operator*) $\rho(t)$ is a Hermitian matrix that describes the state of a quantum system at time t . It is given by the weighted sum (by probabilities p_α) of outer products of state wavefunctions that describe it:³⁵

$$\rho(t) = \sum_{\alpha} p_{\alpha} |\psi_{\alpha}(t)\rangle \langle \psi_{\alpha}(t)| , \quad (\text{B.5})$$

and can describe any quantum state; both **pure** and **mixed** states, where a mixed state is a statistical ensemble of pure states, and the mathematical definitions are as follows,

- $\text{tr}(\rho^2(t)) = 1$ for a pure state,
- $\text{tr}(\rho^2(t)) < 1$ for a mixed state.

B.3 Liouville Space

Usually, quantum mechanical calculations occur in *Hilbert space*, where the observable (i.e. the system Hamiltonian) and the quantum state (the density matrix) are both treated as $(N \times N)$ operators, where N is the number of sites. The quantum Liouville-von Neumann equation for a closed 2-site system as in Equation (1.14), with the abbreviations $H_{\text{sys}} = H$

and $\rho(t) = \rho$ introduced for clarity and the commutation relation $[H, \rho] = H\rho - \rho H$ expanded, can be visualised in Hilbert space as:

$$\begin{bmatrix} \frac{d}{dt}\rho_{11} & \frac{d}{dt}\rho_{12} \\ \frac{d}{dt}\rho_{21} & \frac{d}{dt}\rho_{22} \end{bmatrix} = -\frac{i}{\hbar} \begin{bmatrix} H_{11} & H_{12} \\ H_{21} & H_{22} \end{bmatrix} \begin{bmatrix} \rho_{11} & \rho_{12} \\ \rho_{21} & \rho_{22} \end{bmatrix} + \frac{i}{\hbar} \begin{bmatrix} \rho_{11} & \rho_{12} \\ \rho_{21} & \rho_{22} \end{bmatrix} \begin{bmatrix} H_{11} & H_{12} \\ H_{21} & H_{22} \end{bmatrix}. \quad (\text{B.6})$$

The equation of motion for only the site 1 population, ρ_{11} , by performing the relevant matrix multiplications, is:

$$\frac{d}{dt}\rho_{11} = -\frac{i}{\hbar} (H_{11}\rho_{11} + H_{12}\rho_{21} - \rho_{11}H_{11} - \rho_{12}H_{21}), \quad (\text{B.7})$$

$$\frac{d}{dt}\rho_{11} = -\frac{i}{\hbar} (H_{12}\rho_{21} - \rho_{12}H_{21}). \quad (\text{B.8})$$

It can be seen that the evolution of the site 1 population probability in time is only dependent on the coherences ρ_{12} and ρ_{21} , noticing that because the matrix elements are scalar quantities they commute (i.e. $H_{11}\rho_{11} = \rho_{11}H_{11}$). However, within the non-unitary relaxation dynamics of an excitonic system such as the FMO complex, population transfer pathways between sites can occur by means other than just *via* coherences, such as through interactions with the bath. It is therefore incomplete to have equations of motion for individual site populations that depend only on the coherences; they must contain dependence on all elements of the reduced density matrix.

This can be achieved by converting to a *Liouville space* representation, where observables (such as Liouville operators representing each dynamical process) are given as $(N^2 \times N^2)$ *superoperators*, and the quantum state (the density matrix) is vectorised to have dimensions $(N^2 \times 1)$. Using a general form for the the Liouvillian superoperator \mathcal{L} , and visualising Equation (1.11) in matrix representation:

$$\begin{bmatrix} \frac{d}{dt}\rho_{11} \\ \frac{d}{dt}\rho_{12} \\ \frac{d}{dt}\rho_{21} \\ \frac{d}{dt}\rho_{22} \end{bmatrix} = \begin{bmatrix} \mathcal{L}_{11} & \mathcal{L}_{12} & \mathcal{L}_{13} & \mathcal{L}_{14} \\ \mathcal{L}_{21} & \mathcal{L}_{22} & \mathcal{L}_{23} & \mathcal{L}_{24} \\ \mathcal{L}_{31} & \mathcal{L}_{32} & \mathcal{L}_{33} & \mathcal{L}_{34} \\ \mathcal{L}_{41} & \mathcal{L}_{42} & \mathcal{L}_{43} & \mathcal{L}_{44} \end{bmatrix} \begin{bmatrix} \rho_{11} \\ \rho_{12} \\ \rho_{21} \\ \rho_{22} \end{bmatrix}, \quad (\text{B.9})$$

it is clear to see that switching to Liouville space representation allows the equation of motion for site 1 (and indeed all other site populations in any N -dimensional system) to be dependent

on all elements of the reduced density matrix:

$$\frac{d}{dt} \rho_{11} = \mathcal{L}_{11}\rho_{11} + \mathcal{L}_{12}\rho_{12} + \mathcal{L}_{13}\rho_{21} + \mathcal{L}_{14}\rho_{22} , \quad (\text{B.10})$$

allowing the capture of population transfer processes that occur *via* coherences, as well as those that don't.

B.4 The Liouville-von Neumann Equation

The time-dependent Schrödinger equation:

$$i\hbar \frac{d}{dt} |\psi(t)\rangle = H |\psi(t)\rangle , \quad (\text{B.11})$$

can be used as a starting point to derive its more general analogue for the density matrix; the *Liouville-von Neumann equation*. This section follows a derivation in *The Theory of Open Quantum Systems*.³⁵

Firstly, a time-evolution operator $U(t, t_0)$, with $U(t_0, t_0) = \mathbb{I}$, can be defined that propagates a state in time over some time interval $t - t_0$. Its action on some initial state $|\psi(t_0)\rangle$ is given by:

$$|\psi(t)\rangle = U(t, t_0) |\psi(t_0)\rangle , \quad (\text{B.12})$$

which can be substituted into equation (B.11) to give:

$$i\hbar \frac{\partial}{\partial t} U(t, t_0) = H(t)U(t, t_0) . \quad (\text{B.13})$$

This differential equation can be integrated for the solution:

$$U(t, t_0) = \exp \left[-\frac{i}{\hbar} H(t - t_0) \right] . \quad (\text{B.14})$$

Using the definition of the time-evolved state ket in equation (B.12), the density matrix in equation (B.5) becomes:

$$\rho(t) = \sum_{\alpha} \omega_{\alpha} |\psi_{\alpha}(t)\rangle \langle \psi_{\alpha}(t)| \quad (\text{B.15})$$

$$\rho(t) = \sum_{\alpha} \omega_{\alpha} U(t, t_0) |\psi_{\alpha}(t_0)\rangle \langle \psi_{\alpha}(t_0)| U^{\dagger}(t, t_0) , \quad (\text{B.16})$$

and simplified to:

$$\rho(t) = U(t, t_0)\rho(t_0)U^\dagger(t, t_0) . \quad (\text{B.17})$$

Taking the derivative with respect to time, now $\frac{d}{dt}$ as opposed to the partial differential $\frac{\partial}{\partial t}$ because total time-dependence is now being referred to, and inserting the equation of motion for the time-evolution operator in equation (B.13) the Liouville-von Neumann equation of motion for the density matrix is obtained:

$$\frac{d}{dt}\rho(t) = -\frac{i}{\hbar}[H(t), \rho(t)] . \quad (\text{B.18})$$

B.5 Harmonic Potentials

The protein environment, modelled as an infinite number of bosonic harmonic oscillators,³⁶ can couple to the electronic transitions (i.e. excitons) in the system. Consider the ground and first excited states of a site in the system as harmonic potentials, V_g and V_e respectively. The potential energy curve of the ground electronic state, with an energy minimum of zero at dimensionless coordinate $q = 0$, has the form:

$$V_g(q) = \frac{1}{2}\hbar\omega_0^{(g)}q^2 , \quad (\text{B.19})$$

where $\omega_0^{(g)}$ is the frequency of oscillation for the vibrational ground state. The electronic first excited state is given by a displaced harmonic oscillator:

$$V_e(q) = \omega_{eg} + \frac{1}{2}\hbar\omega_0^{(g)}(q - d)^2 , \quad (\text{B.20})$$

where the potential minimum is at $q = d$, and the difference in energy minima between the potentials is ω_{eg} . Both of these potentials are represented schematically in Figure 1.4a.⁴⁶ The vertical transition energy at any given coordinate, $\Delta V_{eg}(q) = V_e(q) - V_g(q)$, is given by:

$$\Delta V_{eg}(q) = \omega_{eg} + \frac{1}{2}\hbar\left(\omega_0^{(e)} - \omega_0^{(g)}\right)q^2 - \hbar\omega_0^{(e)}dq + \frac{1}{2}\hbar\omega_0^{(e)}d^2 . \quad (\text{B.21})$$

The Franck-Condon principle of vertical transitions is assumed to be obeyed; that electronic excitation is instantaneous, with no change in configuration of the bath.⁷ A vertical electronic transition from the ground vibrational state of the ground electronic state occurs at $q = 0$, so

that:

$$\Delta V_{\text{eg}}(0) = \omega_{\text{eg}} + \frac{1}{2} \hbar \omega_0^{(\text{e})} d^2 . \quad (\text{B.22})$$

For this transition, and after some time, there will be a conformational change in the bath resulting in the vibrational electronically excited state. The energy change associated with this process, known as the reorganisation energy, is given by:

$$\lambda = \Delta V_{\text{eg}}(0) - \omega_{\text{eg}} = \frac{1}{2} \hbar \omega_0^{(\text{e})} d^2 , \quad (\text{B.23})$$

and corresponds to the difference between the vertical electronic transition energy and the energy gap between the minima of the two potentials. The vertical electronic transition energy, $\Delta V_{\text{eg}}(q)$, can be differentiated with respect to oscillator coordinate to quantify the strength of coupling between system and the bath mode ξ that is resonant with the transition, g_ξ . This expression:

$$g_\xi = \frac{d}{dq} (V_{\text{e}}(q) - V_{\text{g}}(q)) = -\hbar \omega_0 d , \quad (\text{B.24})$$

is independent of q if one assumes that the frequencies of oscillation for the vibrational ground states of each potential are equal, i.e. that $\omega_0^{(\text{g})} = \omega_0^{(\text{e})} = \omega_0$.

B.6 Hierarchical Equations of Motion

B.6.1 Bath Correlation Function

Using a Debye spectral density, the temporal bath correlation function can be expressed as an infinite sum of weighted exponentials, which is assumed to be site independent so that $C_j(t) = C(t)$:

$$C(t > 0) = \sum_{k=0}^{\infty} c_k e^{-\nu_k t} . \quad (\text{B.25})$$

The terms ν_k are decay rates known as the *Matsubara frequencies* and are given by:^{5,14,35,49}

$$\nu_k = \frac{2\pi k}{\beta \hbar} , \quad k > 0 \quad (\text{B.26})$$

with $\nu_0 = \gamma$, the bath relaxation rate, while the Matsubara *coefficients* c_k for $k > 0$ are:

$$c_k = \frac{4\lambda\gamma}{\beta\hbar} \left(\frac{\nu_k}{\nu_k^2 + \gamma^2} \right) , \quad (\text{B.27})$$

and for $k = 0$:

$$c_0 = \lambda\gamma \left(\cot\left(\frac{\beta\hbar\gamma}{2}\right) - i \right) . \quad (\text{B.28})$$

Appendix C

Code

C.1 General Use

quantum_HEOM (github.com/jwa7/quantum_HEOM), an open-source Python package written by the author, can be used by any user with a working understanding of Python to define an open quantum system with a high level of control over its parameters, and plot its dynamics. HEOM has been implemented by interfacing with QuTiP’s HEOM solver class,⁶¹ but all other infrastructure, as well as the Lindblad models (using equations from sources cited in the main text) has been built by the author. After following the ‘*Getting Started*’ instructions in the **README**, users can follow the **tutorials** (github.com/jwa7/quantum_HEOM/tree/master/doc/tutorials) that cover:

- The **unit system** used.
- The **possible parameters** that can be controlled when defining a system, and their options.
- Some **examples** of defining systems and plotting features.

C.2 Reproducing Figures

In addition to the general use cases for defining a system from scratch and plotting its dynamics, most of the figures in Chapters 2 and 3 can be reproduced from pre-existing specification files. For every reproducible figure in this thesis, there exists a ‘.txt’ specification file in the *quantum_HEOM/doc/figures/thesis_figures/* package directory that contains the parameters and function calls used to produce it. How to do this is outlined in another short **tutorial**, but boils down (after following the installation instructions in the **README**) to simply copying

the ‘Python-copyable code’ from the specification file into a *jupyter notebook* and running the cell. For example, to plot the fitted site 1 population shown in Figure 2.9, the ‘Python-copyable code’ from [2.9_local_therm_heom_fitted.txt](#) can be run in a *jupyter notebook*. This example is shown in Figure C.1. This makes it easy to see all the parameters that were used to define the *QuantumSystem* object and plot its dynamics. Without much coding experience required due to the ‘black-boxed’ nature of the package, only understanding of the interplay between the parameters is needed to plot the figures.

```

import os
import sys
ROOT_DIR = os.getcwd()[:os.getcwd().rfind('quantum_HEOM')] + 'quantum_HEOM'
if ROOT_DIR not in sys.path:
    sys.path.append(ROOT_DIR)

import numpy as np
from quantum_heom.quantum_system import QuantumSystem
from quantum_heom import figures as figs

# Args for initialising QuantumSystem 1
args1 = {'sites': 2, 'init_site_pop': [1], 'interaction_model': 'spin-boson', 'epsi_delta': (0, 54.1),
         'dynamics_model': 'local thermalising lindblad', 'time_interval': 5.0, 'timesteps': 300,
         'deph_rate': 11, 'temperature': 300.0, 'cutoff_freq': 40.0, 'reorg_energy': 4.0, 'spectral_density': 'debye'}

# Args for initialising QuantumSystem 2
args2 = {'sites': 2, 'init_site_pop': [1], 'interaction_model': 'spin-boson', 'epsi_delta': (0, 50),
         'dynamics_model': 'HEOM', 'time_interval': 5.0, 'timesteps': 300, 'temperature': 300.0, 'cutoff_freq': 20.0,
         'reorg_energy': 2.0, 'spectral_density': 'debye', 'matsubara_terms': 12,
         'matsubara_coeffs': np.array([153.69482151-40.j, 25.63315357+0.j, 12.75333694+0.j, 8.49446285+0.j,
                                       6.36881219+0.j, 5.09429659+0.j, 4.24490629+0.j, 3.63831497+0.j,
                                       3.18342557+0.j, 2.82965066+0.j, 2.54664636+0.j, 2.31510666+0.j]),
         'matsubara_freqs': np.array([-20., 246.77894367, 493.55788733, 740.336831, 987.11577466, 1233.89471833,
                                      1480.67366199, 1727.45260566, 1974.23154932, 2221.01049299, 2467.78943665,
                                      2714.56838032]), 'bath_cutoff': 3}

# Arguments for plotting dynamics.
plot_args = {'elements': ['11'], 'coherences': ['imag'], 'trace_measure': [None], 'asymptote': False,
             'view_3d': False, 'save': True}

# Use the arguments in the following way:
q1 = QuantumSystem(**args1)
q2 = QuantumSystem(**args2)

figs.plot_dynamics([q1, q2], **plot_args)

```

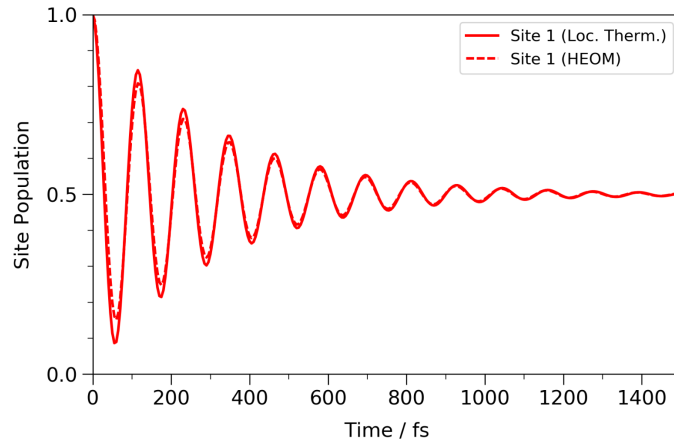


FIGURE C.1: Reproducing the fitted site 1 population from Figure 2.9 using the open-source Python package written by the author.

Bibliography

- [1] J. Wen, H. Zhang, M. L. Gross and R. E. Blankenship, *Proceedings of the National Academy of Sciences of the United States of America*, 2009, **106**, 6134–6139.
- [2] R. E. Fenna and B. W. Matthews, *Nature*, 1975, **258**, 573–577.
- [3] C. Kreisbeck, T. Kramer, M. Rodríguez and B. Hein, *Journal of Chemical Theory and Computation*, 2011, **7**, 2166–2174.
- [4] A. Ishizaki and G. R. Fleming, *Proceedings of the National Academy of Sciences*, 2009, **106**, 17255–17260.
- [5] J. Zhu, S. Kais, P. Rebentrost and A. Aspuru-Guzik, *Journal of Physical Chemistry B*, 2011, **115**, 1531–1537.
- [6] R. E. Blankenship, *Molecular Mechanisms of Photosynthesis*, Blackwell Science Ltd, Oxford, UK, 2002, pp. 1–321.
- [7] F. Fassioli, R. Dinshaw, P. C. Arpin and G. D. Scholes, *Journal of the Royal Society Interface*, 2014, **11**, DOI: 10.1098/rsif.2013.0901.
- [8] J. Adolphs and T. Renger, *Biophysical Journal*, 2006, **91**, 2778–2797.
- [9] P. Brumer and M. Shapiro, *Proceedings of the National Academy of Sciences of the United States of America*, 2012, **109**, 19575–19578.
- [10] D. E. Tronrud, M. F. Schmid and B. W. Matthews, *Journal of Molecular Biology*, 1986, **188**, 443–454.
- [11] J. Strümpfer, M. Şener and K. Schulten, *The Journal of Physical Chemistry Letters*, 2012, **3**, 536–542.
- [12] G. McDermott, S. M. Prince, A. A. Freer, A. M. Hawthornthwaite-Lawless, M. Z. Papiz, R. J. Cogdell and N. W. Isaacs, *Nature*, 1995, **374**, 517–521.

- [13] M. K. Şener, J. D. Olsen, C. N. Hunter and K. Schulten, *Proceedings of the National Academy of Sciences of the United States of America*, 2007, **104**, 15723–15728.
- [14] J. Strümpfer and K. Schulten, *Journal of Chemical Theory and Computation*, 2012, **8**, 2808–2816.
- [15] A. W. Chin, S. F. Huelga and M. B. Plenio, *Philosophical Transactions of the Royal Society A: Mathematical, Physical and Engineering Sciences*, 2012, **370**, 3638–3657.
- [16] S. B. Worster, C. Stross, F. M. W. C. Vaughan, N. Linden and F. R. Manby, *Journal of Physical Chemistry Letters*, 2019, **10**, 7383–7390.
- [17] F. Vaughan, *Ph.D. thesis*, University of Bristol, 2017.
- [18] J. Iles-Smith, A. G. Dijkstra, N. Lambert and A. Nazir, *The Journal of Chemical Physics*, 2016, **144**, 044110.
- [19] J.-L. Brédas, E. H. Sargent and G. D. Scholes, *Nature Materials*, 2017, **16**, 35–44.
- [20] D. Drakova and G. Doyen, 2017, arXiv:1605.06149.
- [21] H. Lee, Y.-C. Cheng and G. R. Fleming, *Science*, 2007, **316**, 1462–1465.
- [22] R. Hildner, D. Brinks and N. F. Van Hulst, *Nature Physics*, 2011, **7**, 172–177.
- [23] M. Mohseni, P. Rebentrost, S. Lloyd and A. Aspuru-Guzik, *The Journal of Chemical Physics*, 2008, **129**, 174106.
- [24] G. S. Engel, T. R. Calhoun, E. L. Read, T. K. Ahn, T. Mančal, Y. C. Cheng, R. E. Blankenship and G. R. Fleming, *Nature*, 2007, **446**, 782–786.
- [25] J. M. Olson, in *The Photosynthetic Bacteria*, Plenum Press, 1978, pp. 161–178.
- [26] B. W. Matthews, R. E. Fenna, M. C. Bolognesi, M. F. Schmid and J. M. Olson, *Journal of Molecular Biology*, 1979, **131**, 259–285.
- [27] B. W. Matthews and R. E. Fenna, *Accounts of Chemical Research*, 1980, **13**, 309–317.
- [28] Y. F. Li, W. Zhou, R. E. Blankenship and J. P. Allen, *Journal of Molecular Biology*, 1997, **271**, 456–471.
- [29] X. Jia, Y. Mei, J. Z. Zhang and Y. Mo, *Scientific Reports*, 2015, **5**, 1–10.

- [30] T. Pullerits, M. Chachisvilis and V. Sundström, *Journal of Physical Chemistry*, 1996, **100**, 10787–10792.
- [31] C. Stross, M. W. Van der Kamp, T. A. A. Oliver, J. N. Harvey, N. Linden and F. R. Manby, *The Journal of Physical Chemistry B*, 2016, **120**, 11449–11463.
- [32] J. Wu, F. Liu, Y. Shen, J. Cao and R. J. Silbey, *New Journal of Physics*, 2010, **12**, 105012.
- [33] M. Cho, H. M. Vaswani, T. Brixner, J. Stenger and G. R. Fleming, *Journal of Physical Chemistry B*, 2005, **109**, 10542–10556.
- [34] G. Panitchayangkoon, D. Hayes, K. A. Fransted, J. R. Caram, E. Harel, J. Wen, R. E. Blankenship and G. S. Engel, *Proceedings of the National Academy of Sciences*, 2010, **107**, 12766–12770.
- [35] H.-P. Breuer and F. Petruccione, in *The Theory of Open Quantum Systems*, Oxford University Press, 2007, ch. 3, pp. 105–172.
- [36] A. O. Caldeira and A. J. Leggett, *Annals of Physics*, 1983, **149**, 374–456.
- [37] T. Renger and R. A. Marcus, *The Journal of Chemical Physics*, 2002, **116**, 9997–10019.
- [38] I. De Vega and D. Alonso, *Reviews of Modern Physics*, 2017, **89**, 1–58.
- [39] D. M. Wilkins and N. S. Dattani, *Journal of Chemical Theory and Computation*, 2015, **11**, 3411–3419.
- [40] A. G. Dijkstra and Y. Tanimura, *Journal of the Physical Society of Japan*, 2012, **81**, 1–4.
- [41] V. Janković and T. Mančal, 2020, arXiv:2001.07180.
- [42] G. D. Scholes, G. R. Fleming, A. Olaya-Castro and R. Van Grondelle, *Nature Chemistry*, 2011, **3**, 763–774.
- [43] I. Kassal, J. Yuen-Zhou and S. Rahimi-Keshari, *Journal of Physical Chemistry Letters*, 2013, **4**, 362–367.
- [44] H. G. Duan, V. I. Prokhorenko, R. J. Cogdell, K. Ashraf, A. L. Stevens, M. Thorwart and R. J. Miller, *Proceedings of the National Academy of Sciences of the United States of America*, 2017, **114**, 8493–8498.

- [45] M. J. Tao, N. N. Zhang, P. Y. Wen, F. G. Deng, Q. Ai and G. L. Long, *Science Bulletin*, 2019, **65**, 318–328.
- [46] A. Ishizaki and G. R. Fleming, *The Journal of Chemical Physics*, 2009, **130**, 234111.
- [47] A. Kell, X. Feng, M. Reppert and R. Jankowiak, *Journal of Physical Chemistry B*, 2013, **117**, 7317–7323.
- [48] P. Rebentrost and A. Aspuru-Guzik, *Journal of Chemical Physics*, 2010, **134**, 101103.
- [49] A. Ishizaki and Y. Tanimura, *Journal of the Physical Society of Japan*, 2005, **74**, 3131–3134.
- [50] G. Lindblad, *Communications in Mathematical Physics*, 1976, **48**, 119–130.
- [51] V. Gorini, *Journal of Mathematical Physics*, 1976, **17**, 821.
- [52] MIT 22.51 Quantum Theory of Radiation Interactions Chapter 8, 2020, https://ocw.mit.edu/courses/nuclear-engineering/22-51-quantum-theory-of-radiation-interactions-fall-2012/lecture-notes/MIT22_51F12_Ch8.pdf.
- [53] F. Vaughan, N. Linden and F. R. Manby, *The Journal of Chemical Physics*, 2017, **146**, 124113.
- [54] A. Redfield, in *Advances in Magnetic and Optical Resonance*, 1965, pp. 1–32.
- [55] M. Ostilli and C. Presilla, *Physical Review A*, 2017, **95**, 1–9.
- [56] Y. Tanimura and R. Kubo, *Journal of the Physical Society of Japan*, 1989, **58**, 101–114.
- [57] Y. Tanimura, *The Journal of Chemical Physics*, 2014, **141**, 044114.
- [58] A. G. Dijkstra and Y. Tanimura, *Physical Review Letters*, 2010, **104**, 1–4.
- [59] R. P. Feynman, *Reviews of Modern Physics*, 1948, **20**, 367–387.
- [60] R. P. Feynman and F. L. Vernon, *Annals of Physics*, 1963, **24**, 118–173.
- [61] J. Johansson, P. Nation and F. Nori, *Computer Physics Communications*, 2013, **184**, 1234–1240.
- [62] T. Meier, V. Chernyak and S. Mukamel, *Journal of Physical Chemistry B*, 1997, **101**, 7332–7342.

- [63] H.-P. Breuer, E.-M. Laine and J. Piilo, *Physical Review Letters*, 2009, **103**, 210401.
- [64] J. Iles-Smith, N. Lambert and A. Nazir, *Physical Review A - Atomic, Molecular, and Optical Physics*, 2014, **90**, 1–9.
- [65] Q. Shi and E. Geva, *The Journal of Chemical Physics*, 2003, **119**, 12063–12076.
- [66] E. L. Read, G. S. Schlau-Cohen, G. S. Engel, J. Wen, R. E. Blankenship and G. R. Fleming, *Biophysical Journal*, 2008, **95**, 847–856.
- [67] A. F. Fidler, V. P. Singh, P. D. Long, P. D. Dahlberg and G. S. Engel, *The Journal of Physical Chemistry Letters*, 2013, **4**, 1404–1409.
- [68] E. Harel and G. S. Engel, *Proceedings of the National Academy of Sciences*, 2012, **109**, 706–711.
- [69] C. Kreisbeck and T. Kramer, *Journal of Physical Chemistry Letters*, 2012, **3**, 2828–2833.
- [70] T. Brixner, J. Stenger, H. M. Vaswani, M. Cho, R. E. Blankenship and G. R. Fleming, *Nature*, 2005, **434**, 625–628.
- [71] Q. Shi, L. Chen, G. Nan, R. X. Xu and Y. Yan, *Journal of Chemical Physics*, 2009, **130**, year.
- [72] H. M. Berman, *Nucleic Acids Research*, 2000, **28**, 235–242.
- [73] F. R. Manby, F. M. Iii, P. J. Bygrave, F. Ding, T. Dresselhaus, A. Buccheri, C. Bungey, S. J. R. Lee, R. Meli, C. Steinmann, T. Tsuchiya, M. Welborn and T. Wiles, 2019, 9220.
- [74] P. Pracht, E. Caldeweyher, S. Ehlert and S. Grimme, *ChemRxiv*, 2019, 1–19.
- [75] C. Curutchet and B. Mennucci, *Chemical Reviews*, 2017, **117**, 294–343.
- [76] E. Collini, C. Y. Wong, K. E. Wilk, P. M. Curmi, P. Brumer and G. D. Scholes, *Nature*, 2010, **463**, 644–647.
- [77] V. Kobe, DH; Aguilera-Navarro, *Physical Review A*, 1994, **50**, 933–938.
- [78] K. Hoki and P. Brumer, *Procedia Chemistry*, 2011, **3**, 122–131.